

UC Berkeley

UC Berkeley Electronic Theses and Dissertations

Title

Local Probe Analysis of the Structural, Electronic, and Optical Properties of Nanomaterials

Permalink

<https://escholarship.org/uc/item/5zv8q3ts>

Author

Joshi, Trinity

Publication Date

2019

Peer reviewed|Thesis/dissertation

Local Probe Analysis of the Structural, Electronic, and Optical Properties of Nanomaterials

By
Trinity Joshi

A dissertation submitted in partial satisfaction of the
requirements for the degree of
Doctor of Philosophy
in
Physics
in the
Graduate Division
of the
University of California, Berkeley

Committee in charge:
Professor Michael F. Crommie, Chair
Professor Feng Wang
Professor Andrew Minor

Spring 2019

Local Probe Analysis of the Structural, Electronic, and Optical Properties of Nanomaterials

Copyright 2019
by
Trinity Joshi

Abstract

Local Probe Analysis of the Structural, Electronic, and Optical Properties of Nanomaterials

by

Trinity Joshi

Doctor of Philosophy in Physics

University of California, Berkeley

Professor Michael F. Crommie, Chair

This dissertation is divided into two segments. The first segment focuses on the structural and electronic characterization of one-dimensional (1D) and two-dimensional (2D) nanostructures using scanning tunneling microscopy (STM) and spectroscopy (STS). The second segment focuses on the investigation of unique optical behavior in 1D-2D heterosystems using scattering-scanning near-field optical microscopy (s-SNOM).

Bottom-up synthesis from molecular precursors provides a useful methodology for designing and fabricating interesting nanomaterials. The first part describes application of bottom-up synthesis techniques to fabricate 1D nanostructures (graphene nanoribbons (GNRs)) and 2D networks (covalent organic frameworks (COF)). Following the synthesis, the structural and electronic properties of these nanomaterials were studied using STM and STS. In this dissertation, two specific GNR projects are discussed that provide in-detail investigation of the manipulation of the electronic properties of GNRs through the site-specific introduction of dopant atoms. The first project describes the detailed study of boron-doped $N = 7$ AGNRs, where the AGNRs are substitutionally doped with boron atoms in their backbone. The second project focuses on the study of sulfur-doped $N = 13$ GNRs, where the sulfur atoms substitutionally dope the edges of the GNRs. This dissertation also describes two COF projects that demonstrate the strong dependence of the electronic structure of single-layer COFs on the chemical bond arrangement within the covalent network. Specifically, the synthesis and characterization of two different porphyrin-based single-layer 2D COFs that exhibit symmetric (COF-366-OMe) and asymmetric (COF-420) bonding environments are studied.

The second part of the thesis describes investigation of the coupling between 1D plasmon polaritons in silver nanowires with 2D phonon polaritons of the silicon carbide (SiC) substrate. The silver nanowire-SiC hybrid structure was investigated using near-field infrared spectroscopy. A significant change in the 1D plasmon dispersion by the 2D phonon polaritons in SiC was observed upon approaching the SiC phonon polariton energies.

To my husband Divesh Joshi and my daughters Drishti Joshi and Trisha Joshi

Table of Contents

List of Figures	v
List of Abbreviations	vii
Acknowledgement	ix
Chapter 1- Introduction	1
1.1 Bottom-up Synthesis of Low-dimensional Nanomaterials	1
1.1.2 Graphene Nanoribbons (GNRs).....	2
1.1.3 Covalent Organic Frameworks (COFs)	4
1.2 Coupled Polaritons in Hybrid Structures.....	6
Chapter 2-Scanning Tunneling Microscopy (STM)	7
2.1 Theory of STM	7
2.1.1 The Bardeen Theory of Electron Tunneling	7
2.1.2 Energy dependence of tunneling matrix elements	11
2.1.3 Asymmetry in Tunneling Spectrum.....	12
2.1.4 The Tersoff–Hamann Model.....	14
2.2 Basic Principles of STM.....	18
2.2.1 STM topography	18
2.2.2 dI/dV spectroscopy.....	19
2.2.3 dI/dV maps	19
2.3 Instrumentation	20
Chapter 3-Scattering Scanning Near-field Optical Microscopy (s-SNOM)	21
3.1 Introduction.....	21
3.2 Basic Working Principle.....	22
3.3 Self-homodyne and homodyne measurements of near-field signal	24
Chapter 4-Graphene Nanoribbons	26
4.1 Bottom-Up Synthesis of $N = 7$ Boron-Doped Graphene Nanoribbons.....	26
4.1.1 Introduction.....	26
4.1.2 Molecular Synthesis.....	27
4.1.3 Bottom-up Fabrication of B-7AGNRs on Au(111)	28
4.1.4 DFT Calculation for B-7AGNRs	32
4.1.4 Summary	35

4.2 Bottom-Up Synthesis of $N = 13$ Sulfur-Doped Graphene Nanoribbons	35
4.2.1 Introduction.....	35
4.1.2 Molecular Synthesis.....	36
4.2.3 Bottom-up Fabrication of S-13-AGNRs on Au(111)	36
4.2.4 Local Electronic Structure of S-13-AGNR.....	39
4.2.4 Theoretical Calculation and Comparison to Experimental Result.....	40
4.2.5 Computational Methods.....	41
4.2.5 Summary	41
4.3 Conclusion and Outlook	42
Chapter 5-Two-Dimensional Covalent Organic Frameworks.....	43
5.1 Symmetric imine-coupled square lattice COF (COF366-OMe).....	43
5.1.1 Introduction.....	43
5.1.2 Molecular Synthesis.....	44
5.1.3 Electronic Structure of the Single Core Precursor TAPP molecule	44
5.1.4 Synthesis of COF366-OMe on Au(111) from Precursor Molecules	46
5.1.5 Local Electronic Structure of COF366-OMe.....	47
5.1.6 DFT Calculations and Comparison to Experimental Results	51
5.1.7 Summary	52
5.2 Asymmetric imine-coupled square lattice COF (COF-420).....	52
5.2.1 Introduction.....	53
5.2.2 Molecular Synthesis.....	54
5.2.3 Synthesis of COF-420 on Au(111) from Precursor Molecules	55
5.2.4 Local Electronic Structure of COF-420.....	57
5.2.5 DFT Calculations and Comparison to Experimental Results	59
5.2.6 Hirshfeld Charge Transfer Analysis	63
5.2.7 Estimation of the Dipole-Induced Inter-sublattice Electrostatic Energy Offset	63
5.2.8 Summary	64
5.3 Conclusion and Outlook	64
Chapter 6-Coupled Plasmon and Phonon Polaritons in a Hybrid Structure.....	65
6.1 Introduction.....	65
6.2 Experimental set-up	66

6.3 Experimental Observation	67
6.4 Theoretical Calculations and Comparison to Experimental Results.....	69
6.5 Materials and Methods. FDTD Numerical Calculations.	72
6.6 Conclusion and Outlook	72
Bibliography	74
Appendix: List of All COFs studied	87

List of Figures

Figure 1.1: Bottom-up Synthesis.	2
Figure 1.2 Example of armchair and zigzag GNRs	3
Figure 1.3 Reaction scheme of N=7 AGNRs.....	4
Figure 1.4 Reaction scheme of Schiff-base condensation reaction.	6
Figure 2.1 An energy diagram of the tip-sample junction.	14
Figure 2.2 The Tersoff – Hamann model of STM.	16
Figure 2.3 Diagram of basic STM set-up.....	18
Figure 3.1 Different NSOM techniques.....	22
Figure 3.2 Basic Working Principle.....	23
Figure 4.1. Synthesis of the B-doped molecular precursor 1.....	28
Figure 4.2 Bottom-up synthesis of B-7AGNRs.....	30
Figure 4.3 Statistical analysis of B-7AGNRs STM images.....	32
Figure 4.4. Experimental and theoretical electronic structure of B-7AGNRs.....	34
Figure 4.5 Synthesis of 1	36
Figure 4.6 Bottom-up synthesis of S-13-AGNRs.....	38
Figure 4.7 Statistical analysis of S-13-AGNRs STM images.....	38
Figure 4.8 STM dI/dV spectroscopy of S-13-AGNRs.....	40
Figure 4.9 Theoretical electronic structure of S-13-AGNRs	41
Figure 5.1 Single TAPP molecule electronic structure.....	45
Figure 5.2 Synthesis of COF366-OMe on a Au(111) surface.	47
Figure 5.3 STS measurements of COF366-OMe on Au(111) surface.....	48
Figure 5.4 Spatial distribution of COF366-OMe electronic states.	50
Figure 5.5 Synthesis of meso-tetra(<i>p</i> -formylphenyl)porphyrin.	54

Figure 5.6 Bottom-up fabrication of COF-420.	56
Figure 5.7 Justification of the assignment of the core A (from TAPP) and core B (from TFPP)	57
Figure 5.8 Electronic structure of COF-420.	59
Figure 5.9 Theoretical electronic structure of COF-420 on Au(111).	60
Figure 5.10 Theoretical electronic structure of free-standing COF-420 monolayer.	61
Figure 5.11 Local charge transfer leads to spatial separation of CB and VB.	62
Figure 6.1 Experimental set-up.....	67
Figure 6.2 Experimental observation.....	68
Figure 6.3 Experimentally measured and numerically calculated λ_{sp}	70
Figure 6.4 Theoretical calculations.....	72

List of Abbreviations

- AFM: Atomic Force Microscopy
- AGNR: Armchair Graphene Nanoribbons
- CB: Conduction Band
- COF: Covalent Organic Framework
- DFT: Density Functional Theory
- DMA: 2,5-dimethoxybenzene-1,4-dicarboxaldehyde
- DOS: Density of States
- FET: Field Effect Transistor
- GNR: Graphene Nanoribbons
- LDA: Local Density Approximation
- LDOS: Local Density of States
- MIM: Metal-Insulator-Metal
- NSOM: Near-field Scanning Optical Microscopy
- PDOS: Projected Density of States
- RT: Room Temperature
- SiC: Silicon Carbide
- SPM: Scanning Probe Microscopy
- s-SNOM: Scattering scanning near-field optical microscopy
- STM: Scanning Tunneling Microscopy
- STS: Scanning Tunneling Spectroscopy
- TAPP: (5,10,15,20-tetrakis (4-aminophenyl) porphyrin
- TMDC: Transition Metal Dichalcogenide
- TFPP: (5,10,15,20-tetrakis (4-formylphenyl) porphyrin
- UHV: Ultra-High Vacuum

VB: Valence Band

ZGNR: Zigzag Graphene Nanoribbons

1D: One-dimensional

2D: Two-Dimensional

Acknowledgement

First of all, I would like to thank my advisor Professor Michael F. Crommie for his endless support, guidance and encouragement throughout my Ph. D. His enthusiasm and love for physics is truly contagious. Working with two home-built machines, there have been times when things did not work as we expected. But his technical expertise along with his positive attitude and enthusiasm helped us power through those rough times. He also taught me how to break down a complex problem into smaller, simpler, approachable ones.

These past six years of my Ph.D would not have been possible without the support of amazing co-workers in the Crommie group. Giang D. Nyugen and Ivan Pechenezhskiy trained me on the HM-VT-STM. Daniel J. Rizzo and Christopher Bronner collaborated with me on the GNR projects. Chen Chen trained me on the home-built low temperature STM. He is the person I worked with on a daily basis for the greatest amount of time in the Crommie group. His strong and impressive background in chemistry allowed him to teach me many interesting new concepts. I really appreciate his flexibility and easy-going attitude. He is the kindest co-worker that I have ever worked with. Gaoqiang Wang worked with me on the COF project. Even though I did not get a chance to work with him a lot, I am confident his hard-work and dedication will give great results. I have also worked with exceptional undergraduates, high-school students and visiting scholars, including Won-Woo Choi, Bobby Ge, Eric Yu, Lingjie Zhou, Peinian Liu, Theron Tarigo and Ting Chen.

Both the GNR and COF projects were inter-disciplinary. These projects were conducted in close collaboration with chemists, theoretical physicists and electrical engineers. The success of these projects would not have been possible without the hard work of my collaborators. I would like to thank Professor Felix Fischer and his group for synthesizing the GNR molecular precursors, Professor Steven Louie and his group for calculating the electronic properties of the GNR and Professor Jeffrey Bokor and his group for fabricating electronic devices from GNRs. I would also like to thank Professor William R. Dichtel, Professor Seth Marder, and Professor Omar M. Yaghi and his group for synthesizing the COF molecular precursors, as well as Professor Jean-Luc Bredas and his group members Hong Li and Huifang Li for calculating the electronic properties of COF structures.

I also would like to express my gratitude to Professor Feng Wang for giving me an opportunity to work with him in the s-SNOM project. I appreciate his guidance and support throughout the project. I would also like to thank the Wang group members. Ji-Hun Kang whose incredible theoretical calculations helped me to more deeply understand my experimental results. And Lili Jiang and Zhiwen Shi who trained me on the s-SNOM set-up.

I would also like to thank our exceptional administrative staff. Anne C Takizawa and Joelle Miles who helped me with paperwork related to my classes, salary, and qualifying exams. Our group assistants Lisa Partida and Elaine Quiter helped me with paperwork regarding funding, travel reimbursements and equipment purchases. Eleanor Crump, Anthony Vitan and Carlos Bustamante from the physics facility who not only took care of our lab but also always kept us well informed about all the activities and maintenance occurring on-site.

Last but definitely not the least, I am extremely grateful to my family. My husband, Divesh Joshi who has loved and supported me throughout my ups and downs. He inspired me to always

keep a positive attitude even when things were not going as I anticipated. I am truly amazed by his work-life balance. He is an amazing father and I really appreciate how he is always there for our daughters. My daughters Drishti Joshi and Trisha Joshi for bringing joy and happiness to each and every moment of my life. They are truly my stress busters. This journey would not have been possible without their unconditional love. My in-laws, Indu and Devendra Joshi, who took such good care of my daughters when I was working. My mother Uma Pradhananga for always believing in me. My father Dr. Trinetra Man Pradhananga for introducing me to the fascinating world of science. Family members Umatri Pradhananga, Sunetra Pradhananga, Dikshya Joshi, Rajana Sakha and Manan Joshi for always supporting me. And finally my pet Jasper Joshi for always making me happy.

Chapter 1- Introduction

1.1 Bottom-up Synthesis of Low-dimensional Nanomaterials

As technology nodes continue to shrink in size, the scale of modern electronic devices now approach the scale of a nanometer [1, 2]. At this length scale, the molecular structure of materials plays a significant role in determining their electronic properties. In order to understand the exotic behavior that emerges at this length scale, as well as to utilize these interesting new properties, extreme control over material chemical structure with atomic precision is required. The question then arises of how to obtain this atomic precision. One approach to achieve such atomic scale structural control is through bottom-up synthesis. Bottom-up synthesis is a fabrication technique where synthesis of materials occurs via self-assembly of atomic or molecular precursors via chemical reactions, thus allowing great flexibility through precursor design. This technique can be applied to synthesize both one-dimensional (1D) (Figure 1.1(a)) as well as two-dimensional (2D) nanostructures (Figure 1b). The bottom-up technique provides a roadmap for engineering new low-dimensional molecular nanostructures with specialized desired properties. In this chapter I will give a brief introduction of two such nanostructures. Firstly, I will discuss 1D graphene nanoribbons [3] (Figure 1a) then I will discuss the 2D covalent organic frameworks [4] (Figure 1.1(b)). The structural as well as the electronic properties of these nanostructures were explored using Scanning Tunneling Microscopy (STM) and Scanning Tunneling Spectroscopy (STS).

Chapter 1- Introduction

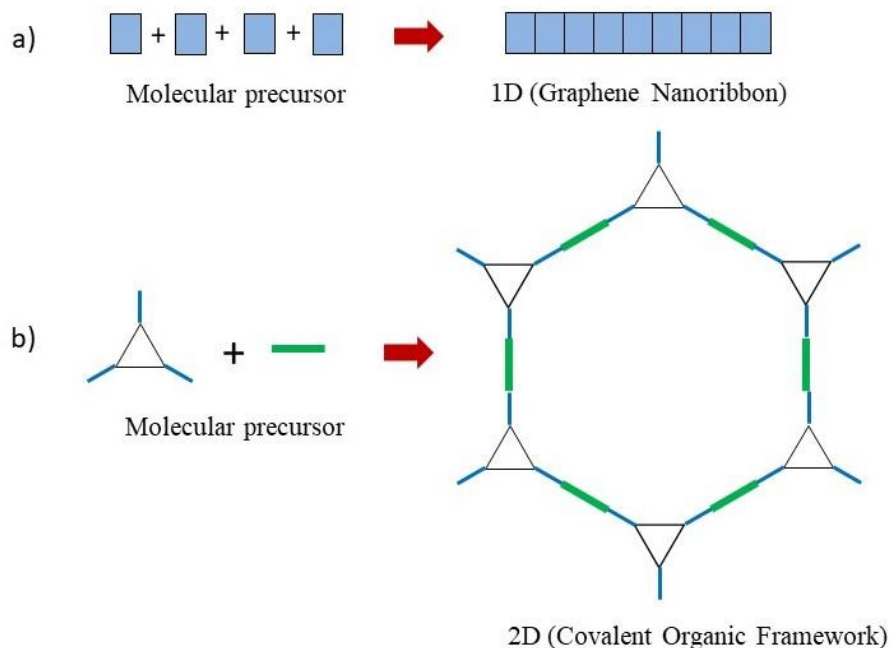


Figure 1.1: Bottom-up Synthesis. (a) Bottom-up Synthesis of 1D nanostructure (graphene nanoribbon) (b) Bottom-up Synthesis of 2D nanostructure (covalent organic framework)

1.1.2 Graphene Nanoribbons (GNRs)

Graphene, a single layer of carbon atoms arranged in a honeycomb lattice, is a two-dimensional semi-metal with zero gap between the valence and conduction band [5]. Graphene exhibits remarkable strength [6] as well as thermal [7] and electrical conductivity [8, 9]. But the absence of a band-gap in graphene prevents it from efficiently performing on-off switching operations [10]. This restricts graphene from being used as transistors in electronic logic circuits. It is possible, however, to open a band-gap in graphene. This can be achieved by cutting it into small ribbons. Such quasi-one-dimensional strips of graphene are called graphene nanoribbons (GNRs). GNRs have a tunable energy gap that depends on their width and edge symmetry [11–14]. The width of a GNR in number of atoms is represented by an integer N (Figure 1.2). The two high symmetry edge structures of a GNR are armchair (Figure 1.2(a)) and zigzag (Figure 1.2(b)).

Chapter 1- Introduction

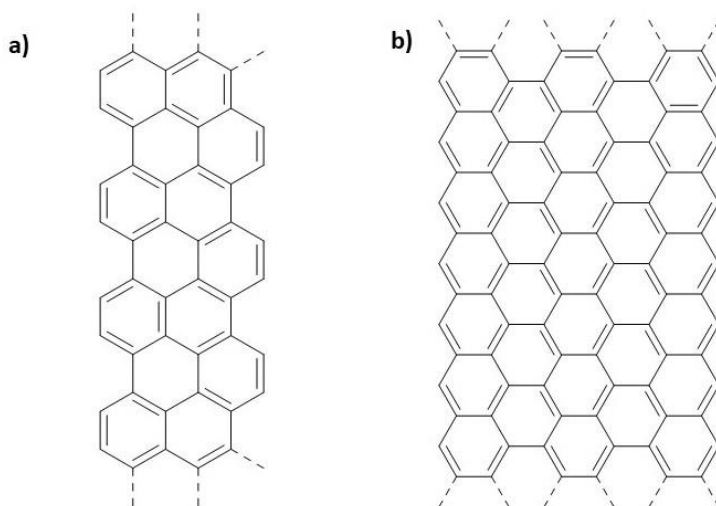


Figure 1.2 Example of armchair and zigzag GNRs (a) 6-Armchair GNR (6-AGNR). Here 6 represents number of carbon rows across the width (b) 6-Zigzag GNR(6-ZGNR). Here 6 represents number of zigzag chains across the width [15].

In-depth theoretical analysis of GNRs can be found in Dr. Yen-Chia Chen's PhD dissertation [16]. One simple approach to understanding the band structure of GNRs is by imposing boundary conditions on graphene wavefunctions. We can qualitatively estimate the band structure of a GNR by sampling the Dirac cones of the graphene bands at different slicing planes in k -space and then projecting them onto a one-dimensional band structure using a zone-folding technique [13]. The edge geometry of the GNR determines the orientation of the slicing planes in k -space whereas the width of the GNR determines the quantization distance between adjacent slicing planes. Hence, the width and the edge geometry of GNRs play an important role in determining their electronic properties. More accurate DFT calculations introduce some changes to the band structure of GNRs due to edge relaxations and spin-polarization effects [12]. Additional GW corrections predict bigger band gaps compared to standard DFT calculations [11, 15, 17, 18].

GNRs have previously been fabricated by the top-down methods of unzipping carbon nanotubes [19], chemical vapor deposition [19], etching of 2D-graphene [20], and scanning probe lithography [20]. However, these techniques all lacked atomic precision and control, critical factors in determining GNR electronic structure. Cai and co-workers reported the first synthesis of atomically-precise GNRs by a bottom-up strategy [3]. In the bottom-up approach materials are self-assembled from smaller molecular precursors via chemical reaction. Figure 1.3 shows the reaction pathway for the bottom-up synthesis of $N = 7$ AGNRs. This particular GNR is made from molecular precursors that are terminated by halogen atoms. These precursors are deposited onto a

Chapter 1- Introduction

metallic substrate and upon annealing to elevated temperature undergo a two-step reaction. The first step is a surface-assisted chemical reaction (Ullmann-type coupling) where the aryl-halogen bond of the molecular precursor cleaves, leaving the molecular precursors with radicals [21–24]. These radicals then diffuse on the surface and bond with each other to form polymers. The second step is cyclodehydrogenation whereupon further annealing to higher temperature causes C-H bonds to be cleaved and C-C bonds to form, yielding flat GNRs.

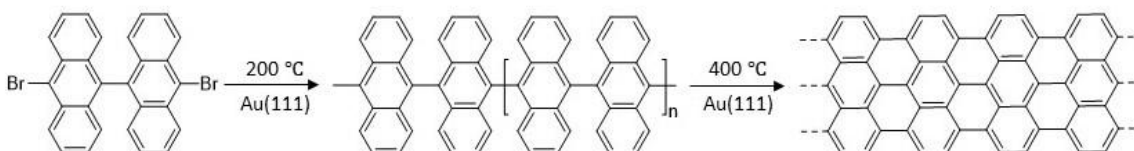


Figure 1.3 Reaction scheme of N=7 AGNRs. Molecular precursor dibromo- bisanthracence (left) is deposited on the Au(111) surface. The sample is then annealed to 200°C whereupon the molecules undergo Ullmann-type coupling reaction to form linear polymers. Upon further annealing to 400° C the polymers undergo cyclodehydrogenation to form N=7 AGNRs.[3]

Ullmann-type coupling followed by cyclodehydrogenation has become one of the most popular technique for the synthesis of bottom-up GNRs with different width and edge geometries [3, 25, 26]. But the incorporation of the GNRs into device configurations requires significant modification of their band structure. This can be achieved by introducing site-specific dopant atoms. This could further lead to the introduction of new states into the GNR band-gap leading to entirely new electronic properties. This dissertation will present two such projects. The first project describes boron-doped $N = 7$ AGNRs, involving AGNRs that are substitutionally doped with boron atoms in their backbone [27]. The second project focuses on the study of sulfur-doped $N = 13$ GNRs, where sulfur atoms are substitutionally positioned into the GNR edges [28].

1.1.3 Covalent Organic Frameworks (COFs)

Covalent organic frameworks (COFs) are crystalline extended organic structures composed of light elements (such as carbon, boron, nitrogen, oxygen, and so on) linked together by strong covalent bonds [4, 29, 30]. The exotic electronic properties observed in single-layer two-dimensional materials such as graphene and the transition metal dichalcogenides have sparked great interest in exploring new, single-layer COF films [31–36]. Bottom-up synthesis from molecular precursors provides a useful methodology for designing and fabricating this new class of 2D materials. The full power of organic chemical synthesis enables us to engineer COFs with a variety of unit cells [37]. This provides us with new opportunities to fabricate 2D crystal lattices with interesting electronic properties [38, 39]. In addition to this, the electronic structure of 2D-

Chapter 1- Introduction

COFs is highly dependent on the chemical bonds within these networks. Hence, COFs have recently been proposed as a potential candidate for molecular electronics because of their tunable electronic structure. Furthermore, bandgap engineering can be employed in COFs to synthesize semiconductor heterostructure devices with novel optical, optoelectronic, and device properties. COFs are thus of great interest to chemists who study the synthesis of new molecular assemblies, to physicists who explore the electronic and magnetic structure of 2D networks, and to engineers who are keen to integrate these materials into future nanodevices.

Ever since the discovery of the COFs in 2005 by the Yaghi group [4] there have been reports of several different types of COFs with numerous chemical linkages [29, 40–42], pore sizes [43], and geometries [37, 44, 45]. The majority of the reported COFs have been synthesized in solution [44, 46, 47], bulk [4], or in the form of thin-films [46]. Only a limited number of single-layer COFs have been synthesized [48–52] and even fewer of them have been examined using scanning tunneling spectroscopy [53, 54]. Hence, the fabrication and the electronic structure characterization of single-layer COFs is still in its infancy. There exists a need to characterize single-layer COFs in order to understand and utilize the novel electronic properties they exhibit. This dissertation presents the on-surface synthesis and electronic structure characterization of two-different COFs with square symmetry, an important symmetry class for molecular materials. We accomplished this by synthesizing molecular precursors designed to self-assemble into a molecular network via the Schiff-base condensation reaction [55]. Figure 1.4 presents a reaction pathway for molecular precursors to self-assemble into COFs via the Schiff-base condensation reaction [56]. This reaction can only take place between two different types of precursors. One of the precursors must be functionalized with an amine ($-\text{NH}_2$) group whereas the other precursor must be functionalized with a carbonyl ($-\text{C}=\text{O}$) group. In the example shown in Figure 1.4 the precursor 5,10,15,20-tetrakis (4-aminophenyl) porphyrin (TAPP) is functionalized with amine groups whereas the precursor 2,5-dimethoxybenzene-1,4-dicarboxaldehyde (DMA) is functionalized with carbonyl groups. During the reaction, the hydrogen and oxygen from the precursors react to form water (as a side-product) such that the precursors can be reticulated into a covalent network held together by the imine ($-\text{C}=\text{N}$) bonds (Figure 1.4). This dissertation will describe two different types of single layer imine-coupled square lattice COFs [56, 57]. The resulting COFs were characterized by STM in ultrahigh vacuum and at cryogenic temperatures to ensure the highest possible experimental resolution in a contamination free measurement.

Chapter 1- Introduction

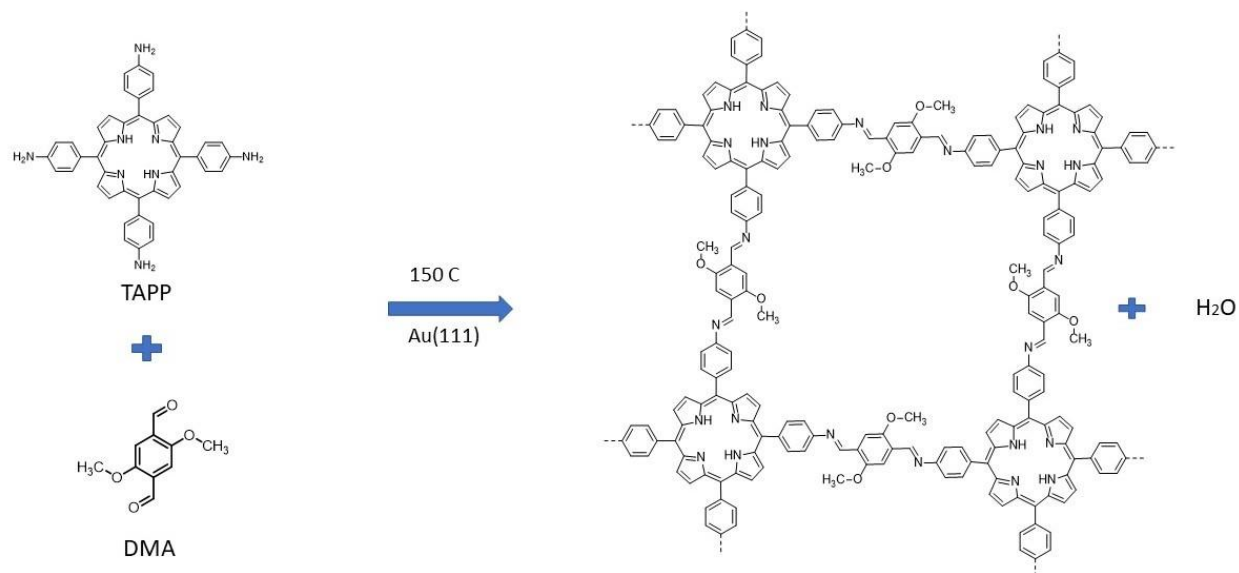


Figure 1.4 Reaction scheme of Schiff-base condensation reaction. The left molecules are TAPP and DMA which are precursor molecules functionalized with amine (-NH₂) and carbonyl (-C=O) groups respectively. After deposition on the Au(111) surface, the sample is annealed to 150° C resulting in the formation of imine-coupled square lattice COFs through the Schiff-base condensation reaction.[56]

1.2 Coupled Polaritons in Hybrid Structures.

Microscopic coupling of photons with electrons and optical phonons gives rise to two unique quasiparticles: surface plasmons (SPs) and phonon polaritons (PhPs). This provides a novel platform for the localization and manipulation of light in the sub-diffraction regime by strongly enhancing the electric fields in the proximity of material surfaces. Excitation of both infrared SPs and PhPs simultaneously in heterostructures facilitates further control of infrared light-matter interactions at the nanoscale. This dissertation will present the first study of coupling behavior arising from interaction between two distinct polaritons in different dimensionality, and will show that the coupling behavior in 1D-2D hetero-systems can exhibit unique behavior. Specifically, I will discuss investigation of the coupling of 1D plasmon polaritons in silver nanowires with 2D phonon polaritons in silicon carbide (SiC) substrates for silver nanowire-SiC hybrid structures using scattering-scanning near-field optical microscopy (s-SNOM) [58–61].

Chapter 2-Scanning Tunneling Microscopy (STM)

2.1 Theory of STM

2.1.1 The Bardeen Theory of Electron Tunneling

Following the discussion in ref. [62], this section presents the basic theory of tunneling. Bardeen's first-order perturbation theory [63] is the most widely applied theory to explain tunneling phenomena in STM. In order to verify the Bardeen–Cooper–Schrieffer (BCS) theory of superconductivity [64], Giaever [65–67] designed and demonstrated an experiment involving tunneling spectroscopy with metal–insulator–metal (MIM) tunneling junctions. His MIM tunneling experiment led to the development of new concepts regarding tunneling phenomena. These concepts, developed through the study of MIM tunneling junctions, play a vital role in the understanding of tunneling phenomena in STM and STS.

Bardeen considered an MIM tunnel junction as two separate subsystems of a metal-insulator interface first, rather than solving the Schrödinger equation of the combined system. By solving the stationary Schrödinger equation of the subsystems the electronic states of the individual subsystems are first obtained. These solutions are much easier to obtain than the combined system. Time-dependent perturbation theory is then used to calculate the transmission rate of electrons from one electrode to another. Several assumptions/approximations of Bardeen's theory are [62]:

1. Tunneling is weak and first-order approximations are enough to describe the system.
2. Eigenstates of the two electrodes are nearly orthogonal.
3. Electron-electron interactions are ignored.
4. Occupation probabilities for sample and tip states are independent of each other. These probabilities do not change during tunneling.
5. Both the sample and the tip are in electrochemical equilibrium.

In the 1-D case (junction along Z-axis), when the two electrodes are far apart, the wavefunctions of electrode A (left) satisfy the Schrödinger equation of the free electrode A

$$\left[\frac{-\hbar^2}{2m} \frac{\partial}{\partial z^2} + U_A \right] \varphi = i\hbar \frac{\partial \varphi}{\partial t} \quad (2.1)$$

Chapter 2-Scanning Tunneling Microscopy (STM)

where U_A is the potential function of electrode A depending on both spatial and time coordinates, and φ is the stationary state of electrode A and is given by:

$$\varphi = \psi_\mu e^{-iE_\mu t/\hbar} \quad (2.2)$$

The spatial wavefunctions and energy eigenvalues satisfy the following equation

$$\left[\frac{-\hbar^2}{2m} \frac{\partial}{\partial z^2} + U_A \right] \psi_\mu = E_\mu \psi_\mu \quad (2.3)$$

Similarly, the wavefunctions of electrode B (right) satisfy the Schrödinger equation of the free electrode B

$$\left[\frac{-\hbar^2}{2m} \frac{\partial}{\partial z^2} + U_B \right] \varphi = i\hbar \frac{\partial \varphi}{\partial t} \quad (2.4)$$

where U_B is the potential function of electrode B depending on both spatial and time coordinates, and φ is the stationary state of electrode B and is given by:

$$\varphi = \chi_\nu e^{-iE_\nu t/\hbar} \quad (2.5)$$

The spatial wavefunctions and energy eigenvalues satisfy the following equation

$$\left[\frac{-\hbar^2}{2m} \frac{\partial}{\partial z^2} + U_B \right] \chi_\nu = E_\nu \chi_\nu \quad (2.6)$$

When the two electrodes are far apart the wavefunctions of electrode A and electrode B decay into the vacuum. But when the two electrodes are brought together, the Schrödinger equation of the combined system is given by

$$i\hbar \frac{\partial \varphi}{\partial t} = \left[\frac{-\hbar^2}{2m} \frac{\partial}{\partial z^2} + U_A + U_B \right] \varphi \quad (2.7)$$

In the presence of the combined potential, the state ψ_μ described by equation (2.3) will no longer evolve according to the equation (2.1). It now has a probability of transferring to the states of electrode B. In other words, we assume the wavefunction of the entire junction system to be

$$\varphi = \psi_\mu e^{-iE_\mu t/\hbar} + \sum_{\nu=1}^{\infty} c_\nu(t) \chi_\nu e^{-iE_\nu t/\hbar} \quad (2.8)$$

where the coefficients $c_\nu(t)$ are to be determined by equation (2.7) and at time $t = 0$, $c_\nu(0) = 0$.

The wavefunctions ψ_μ and χ_ν belong to different Hamiltonians and neither of them are the eigenfunction of the Hamiltonian of the combined system. According to our assumption, eigenstates of the two electrodes are nearly orthogonal.

Chapter 2-Scanning Tunneling Microscopy (STM)

Now, inserting equation (2.8) into equation (2.7) leads to

$$i\hbar \sum_{v=1}^{\infty} \frac{dc_v(t)}{dt} \chi_v e^{-iE_v t/\hbar} = U_B \psi_{\mu} e^{-iE_{\mu} t/\hbar} + U_A \sum_{\lambda=1}^{\infty} c_{\lambda}(t) \chi_{\lambda} e^{-iE_{\lambda} t/\hbar} \quad (2.9)$$

Taking the inner product of both sides of the preceding equation with $\chi_v^* e^{iE_v t/\hbar}$, and using the fact that ψ_{μ} and χ_v are orthogonal, we have

$$i\hbar \frac{dc_v(t)}{dt} = \int \chi_v^* U_B \psi_{\mu} e^{-i(E_{\mu}-E_v)t/\hbar} d^3\mathbf{r} + \int \chi_v^* U_A \chi_{\lambda} c_{\lambda}(t) d^3\mathbf{r}$$

The second term on the right-hand side can be neglected under the approximation that tunneling is weak enough that coefficients $c_{\lambda}(t)$ are sufficiently small when t is close to 0. Hence, we have

$$i\hbar \frac{dc_v(t)}{dt} = \int \psi_{\mu} U_B \chi_v^* e^{-i(E_{\mu}-E_v)t/\hbar} d^3\mathbf{r}. \quad (2.10)$$

Defining a tunneling matrix element as

$$M_{\mu\nu} = \int \chi_{\nu}^* U_B \psi_{\mu} d^3\mathbf{r} \quad (2.11)$$

and integrating equation (2.10) over time, the amplitude of the ν^{th} state of electrode B at time t is given by $c_{\nu}(t)$,

$$c_{\nu}(t) = M_{\mu\nu} \frac{e^{-i(E_{\mu}-E_{\nu})t/\hbar} - 1}{E_{\mu} - E_{\nu}} \quad (2.12)$$

Hence, if we start with the μ^{th} state of electrode A, the probability of having the ν^{th} state of electrode B at time t is given by

$$\rho_{\mu\nu}(t) \equiv |c_{\nu}(t)|^2 = |M_{\mu\nu}|^2 \frac{4\sin^2((E_{\mu}-E_{\nu})t/2\hbar)}{(E_{\mu}-E_{\nu})^2} \quad (2.13)$$

The function $f(t)$, defined as

$$f(t) = \frac{4\sin^2((E_{\mu}-E_{\nu})t/2\hbar)}{(E_{\mu}-E_{\nu})^2} \quad (2.14)$$

reaches its maximum at $E_{\mu} = E_{\nu}$ and approaches zero rapidly for $E_{\mu} \neq E_{\nu}$. Hence, the tunneling current depends on the number of available states of electrode B near the energy value of a state in electrode A can tunnel into. If $\rho_B(E)$ is the density of states of the electrode B at energy E , the total probability of tip states that the original sample state can tunnel into at time t is

Chapter 2-Scanning Tunneling Microscopy (STM)

$$p_{\mu\nu}(t) = \frac{2\pi}{\hbar} |M_{\mu\nu}|^2 \rho_B(E_\mu) t \quad (2.15)$$

where the mathematical identity $\int_{-\infty}^{+\infty} \frac{\sin^2 au}{\pi au^2} du = 1$ is used.

The time of tunneling is much greater than $\frac{\hbar}{\Delta E}$, where ΔE is the energy resolution, and so we assume the condition of elastic tunneling $E_\mu = E_\nu$. Hence, the states in electrode A can only tunnel into states in electrode B of the same energy value.

Now from the side of electrode A, the number of available states is defined by the density of states of electrode A at energy E, $\rho_A(E)$, and the energy interval defined by the bias voltage V . Assuming that the density of states of both electrodes does not vary appreciably near the Fermi level over the range of the applied bias voltage V , the tunneling current is

$$I = \frac{2\pi e^2}{\hbar} |M_{\mu\nu}|^2 \rho_A(E_F) \rho_B(E_F) V \quad (2.16)$$

and the tunneling conductance $G = I/V$ is

$$G = 2\pi^2 G_0 |M_{\mu\nu}|^2 \rho_A(E_F) \rho_B(E_F) \quad (2.17)$$

where $G_0 = \frac{e^2}{\pi\hbar}$ is the conductance quantum.

Upon further analysis, tunneling matrix $M_{\mu\nu}$ is given by

$$M_{\mu\nu} = \frac{\hbar^2}{2m} \int_{z=z_0} \left[\psi_\mu \frac{\partial \chi_\nu^*}{\partial z} - \chi_\nu^* \frac{\partial \psi_\mu}{\partial z} \right] dx dy \quad (2.18)$$

and it is the surface integral of the wavefunctions (and their normal derivatives) of the two electrodes calculated at the separation surface. This formula is symmetric with regards to both electrodes.

The above derivations are based on two electrodes A and B separated by a tunnel barrier. The Bardeen theory provides the basis of the tunneling principle of STM if we assume one electrode as the tip and the other as the sample. Using equation (2.16), and by summing over all the relevant states the tunneling current at a bias voltage V can be evaluated. When the temperature is finite electrons in both electrodes follow the Fermi distribution [68]

$$f(E) = (1 + \exp[(E - E_F)/k_B T])^{-1} \quad (2.19)$$

Thus, with a bias voltage V , the total tunneling current is

Chapter 2-Scanning Tunneling Microscopy (STM)

$$I = \frac{4\pi e}{\hbar} \int_{-\infty}^{+\infty} [f(E_F - eV + \varepsilon) - f(E_F + \varepsilon)] \rho_A(E_F - eV + \varepsilon) \rho_B(E_F + \varepsilon) |M|^2 d\varepsilon \quad (2.20)$$

Where, $\rho_A(E)$ and $\rho_B(E)$ are the density of states of electrode A and electrode B respectively.

When $k_B T$ is smaller than the energy resolution required in the measurement, then $f(E)$ can be approximated by a step function, and the tunneling current is then given by

$$I = \frac{4\pi e}{\hbar} \int_0^{eV} \rho_A(E_F - eV + \varepsilon) \rho_B(E_F + \varepsilon) |M|^2 d\varepsilon \quad (2.21)$$

If we assume the magnitude of tunneling matrix $|M|$ does not change too much in the interested energy interval. The tunneling current is given by the convolution of DOS of two electrodes

$$I \propto \int_0^{eV} \rho_A(E_F - eV + \varepsilon) \rho_B(E_F + \varepsilon) d\varepsilon \quad (2.22)$$

The electronic structure of the two participating electrodes thus make symmetrical contribution to the tunneling current. Hence, ρ_A (DOS of electrode A) and ρ_B (DOS of electrode B) contribute equally to the tunneling current.

2.1.2 Energy dependence of tunneling matrix elements

Bardeen assumed that the tunneling matrix element $|M|$ is constant, but in STS experiments the energy scale could be as large as $\pm 2eV$. Hence, it is important to evaluate the dependence of $|M|$ on energy.

In the gap region, the wavefunction of electrode A is

$$\psi_\mu(z) = \psi_\mu(0) e^{-\kappa_\mu z} \quad (2.23)$$

$\kappa_\mu = \sqrt{2mE_\mu}/\hbar$ is the decay constant corresponding to the energy eigenvalue of φ_μ , and $z = 0$ indicates the interface between electrode A and the tunnel barrier,

Similarly in the gap region, the wavefunction of electrode B is

$$\chi_\nu(z) = \chi_\nu(s) e^{-\kappa_\nu(s-z)} \quad (2.24)$$

where $\kappa_\nu = \sqrt{2mE_\nu}/\hbar$ is the decay constant corresponding to the energy eigenvalue of χ_ν and $z = s$ indicates the interface between electrode B and the tunnel barrier. Due to the condition of elastic tunneling, $\kappa_\nu = \kappa_\mu = \sqrt{2mE_\mu}/\hbar$.

Inserting equation (2.23) and equation (2.24) into equation (2.18), we obtain

Chapter 2-Scanning Tunneling Microscopy (STM)

$$M_{\mu\nu} = \frac{\hbar^2}{2m} \int_{z=z_0} 2\kappa_\mu \psi_\mu(0) \chi_\nu(s) e^{-\kappa_\mu z_0} e^{\kappa_\mu(-s+z_0)} dx dy$$

$$M_{\mu\nu} = \left[\frac{\hbar^2}{2m} \int_{z=z_0} 2\kappa_\mu \psi_\mu(0) \chi_\nu(s) dx dy \right] e^{-\kappa_\mu s} \quad (2.25)$$

Hence, the tunneling matrix does not depend on the position of the separation surface, $z = z_0$. $\chi_\nu(s)$ is the value of the wavefunction of electrode B at the interface between electrode B and the tunnel barrier, thus the expression in the square bracket is constant. The energy dependence of the tunneling matrix element $M_{\mu\nu}$ comes from the decay constant κ_μ .

We will now apply the effect of the energy dependence of the tunneling matrix element to STS to predict the existence of asymmetry due to the effect of tip DOS and the sample DOS.

2.1.3 Asymmetry in Tunneling Spectrum

Figure 2.1 shows an energy diagram of a tip-sample junction. When a positive sample bias voltage V is applied, the Fermi level of the sample is lowered by eV compared to the Fermi level of the tip. The electrons thus tunnel from occupied states of the tip into empty states of the sample. An average work function $\bar{\phi}$, the energy difference of the vacuum level to the middle of the two Fermi levels, is introduced.

Rewriting equation (2.21) into symmetrical form with respect to the tip and the sample results in

$$I = \frac{4\pi e}{\hbar} \int_{-\frac{1}{2}eV}^{\frac{1}{2}eV} \rho_{Tip} \left(E_F - \frac{1}{2}eV + \varepsilon \right) \rho_{Sample} \left(E_F + \frac{1}{2}eV + \varepsilon \right) |M(\varepsilon)|^2 d\varepsilon. \quad (2.26)$$

The decay constant for a tip-occupied state of eigenvalue E is given by

$$\kappa = \frac{\sqrt{2mE}}{\hbar} = \frac{\sqrt{2m(\bar{\phi}-\varepsilon)}}{\hbar}. \quad (2.27)$$

Under experimental conditions, ε (the variable of integration of equation (2.26)) is smaller than $\frac{1}{2}eV$. Thus, ε is much smaller than $\bar{\phi}$, and we can then expand equation (2.27) to

$$\kappa = \frac{\sqrt{2m(\bar{\phi}-\varepsilon)}}{\hbar} = \frac{\sqrt{2m\bar{\phi}}}{\hbar} \left(1 - \frac{\varepsilon}{2\bar{\phi}} \right) = \kappa_0 \left(1 - \frac{\varepsilon}{2\bar{\phi}} \right) \quad (2.28)$$

where $\kappa_0 = \frac{\sqrt{2m\bar{\phi}}}{\hbar}$ is the decay constant corresponding to the average work function $\bar{\phi}$.

Chapter 2-Scanning Tunneling Microscopy (STM)

Following equation (2.25), the tunneling matrix can be written as a function of the energy parameter ε

$$M(\varepsilon) = M(0)\exp\left(\frac{\kappa_0\varepsilon s}{2\phi}\right). \quad (2.29)$$

Inserting equation (2.29) into equation (2.26) gives an expression of tunneling current as follows:

$$I = \frac{4\pi e}{\hbar} \int_{-\frac{1}{2}eV}^{\frac{1}{2}eV} \rho_{Tip}\left(E_F - \frac{1}{2}eV + \varepsilon\right) \rho_{Sample}\left(E_F + \frac{1}{2}eV + \varepsilon\right) |M(0)|^2 \exp\left(\frac{\kappa_0\varepsilon s}{\phi}\right) d\varepsilon \quad . \quad (2.30)$$

If we examine the equation (2.30) carefully, we notice that the positive half of the bias interval is more important than the negative half due to the exponential factor.

In the limiting case, with gap width s being large, the main contribution to the tunneling current (equation (2.30)) comes from a small energy interval near $\varepsilon \approx \frac{1}{2}eV$. In this case, the tunneling conductance is approximately

$$\frac{dI}{dV} \approx \rho_{Sample}(E_F + eV)\rho_{Tip}(E_F) \quad (2.31)$$

In other words, by using a positive bias to probe the unoccupied states of the sample, the tunneling current at bias voltage V is proportional to the sample DOS at energy $E_F + eV$, as if the tip DOS is flat (i.e. the tip DOS is concentrated at the Fermi level).

However, when a negative bias is applied to the sample, electrons from the occupied states of the sample tunnel to the unoccupied states of the tip. In this case, the energy spectrum of the tip plays a significant role. Hence, great care must be taken to ensure that the tip DOS is flat.

Chapter 2-Scanning Tunneling Microscopy (STM)

properties can be taken out of the problem. Tersoff and Hamann proposed a model that represented the tip as a geometrical point such that the STM image is only related to the properties of the surface [62]. Following the discussion in ref. [62], the original derivation by Tersoff and Hamann is given below.

As shown in Figure 2.2, the STM tip is modeled as a locally spherical potential well with radius of curvature R centered at r_0 . The sample surface is represented by the $z = 0$ plane. The center of curvature of the tip is $r_0 = (0, 0, z_0)$. In the vacuum region, both wave functions of the sample and the tip near the Fermi level satisfy the Schrödinger equation

$$-\frac{\hbar^2}{2m} \Delta \psi(\mathbf{r}) = -\phi \psi(\mathbf{r}) \quad (2.32)$$

Where ϕ is the work function. Using the decay constant $\kappa = \sqrt{2m\phi}/\hbar$, equation (2.32) becomes

$$\Delta \psi(\mathbf{r}) = \kappa^2 \psi(\mathbf{r}). \quad (2.33)$$

For the sample wave function in the vacuum, equation (2.33) can be expressed using a two-dimensional Fourier expansion. Using the notation $\mathbf{x} = (x, y)$ and $\mathbf{q} = (k_x, k_y)$, the general form of the sample wavefunction is

$$\psi(\mathbf{r}) = \int d^2 \mathbf{q} f(\mathbf{q}, z) e^{i\mathbf{q} \cdot \mathbf{x}} \quad (2.34)$$

Inserting this into equation (1.33), we obtain the equation for $f(\mathbf{q}, z)$,

$$\frac{d^2}{dz^2} f(\mathbf{q}, z) = (\mathbf{q}^2 + \kappa^2) f(\mathbf{q}, z). \quad (2.35)$$

The solution in the vacuum region is then

$$f(\mathbf{q}, z) = a(\mathbf{q}) e^{-\sqrt{\mathbf{q}^2 + \kappa^2} \cdot z} \quad (2.36)$$

where $a(\mathbf{q})$ are the coefficients of the Fourier components of the surface wavefunction at $z = 0$. They contain all the information of the surface electronic structure. The general form of the sample wavefunction in the vacuum region is then

$$\psi(\mathbf{r}) = \int d^2 \mathbf{q} a(\mathbf{q}) e^{-\sqrt{\mathbf{q}^2 + \kappa^2} \cdot z + i\mathbf{q} \cdot \mathbf{x}} \quad (2.37)$$

Chapter 2-Scanning Tunneling Microscopy (STM)

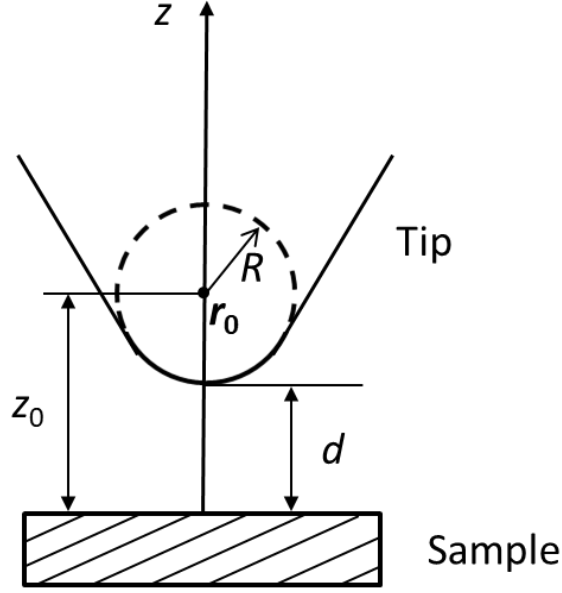


Figure 2.2 The Tersoff–Hamann model of STM. The tip is modeled as a locally spherical potential well with radius of curvature R centered at \mathbf{r}_0 . Adapted from Figure 6.1 of reference [62].

For the tip wave function, $\psi(\mathbf{r})$, Tersoff and Hamann assumed that it is spherically symmetric with respect to the center of curvature \mathbf{r}_0 . Denoting $r^2 = x^2 + y^2 + (z - z_0)^2$, the spherically symmetric tip wave function can be written as $\varphi(\mathbf{r})$, then equation (2.33) becomes

$$\frac{1}{r} \frac{d^2}{dr^2} [r\chi(\mathbf{r})] = \kappa^2 \chi(\mathbf{r}) . \quad (2.38)$$

Up to a constant, the solution is

$$\chi(\mathbf{r}) = \frac{1}{r} e^{-\kappa r} . \quad (2.39)$$

For the region $z < z_0$, the Fourier transform of equation (2.39) is

$$\chi(\mathbf{r}) = \frac{1}{r} e^{-\kappa r} = \frac{1}{2\pi} \int d^2\mathbf{p} \frac{e^{-\sqrt{\kappa^2 + \mathbf{p}^2}(z_0 - z) + i\mathbf{p} \cdot \mathbf{x}}}{\sqrt{\kappa^2 + \mathbf{p}^2}} \quad (2.40)$$

where \mathbf{p} is the two-dimensional wave vector variable for the Fourier transform.

With these wavefunctions, Tersoff and Hamann estimated the tunneling matrix element using equation (2.18):

Chapter 2-Scanning Tunneling Microscopy (STM)

$$M = -\frac{\hbar^2}{2m} \int_{z=0} \left[\chi^* \frac{\partial \psi}{\partial z} - \psi \frac{\partial \chi^*}{\partial z} \right] dx dy . \quad (2.41)$$

Up to a constant, it leads to

$$M \propto \int d^2 \mathbf{q} \int d^2 \mathbf{p} \int d^2 \mathbf{x} \left[1 + \frac{\sqrt{\kappa^2 + \mathbf{q}^2}}{\sqrt{\kappa^2 + \mathbf{p}^2}} \right] a(\mathbf{q}) e^{-\sqrt{\kappa^2 + \mathbf{q}^2} \cdot z_0 + i(\mathbf{p} + \mathbf{q}) \cdot \mathbf{x}} . \quad (2.42)$$

Integration over \mathbf{x} gives a delta function $\delta(\mathbf{p} + \mathbf{q})$. Hence

$$M \propto \int d^2 \mathbf{q} a(\mathbf{q}) e^{-\sqrt{\kappa^2 + \mathbf{q}^2} \cdot z_0} . \quad (2.43)$$

Comparing this with equation (2.37), we found that the tunneling matrix element is the value of the sample wave function at $\mathbf{r}_0 = (0, 0, z_0)$, which is the center of curvature of the tip

$$M \propto \varphi(\mathbf{r}_0) . \quad (2.44)$$

Summing up all sample states near the Fermi level leads to the following expression for the tunneling conductance:

$$G \equiv \frac{I}{V} \propto |\varphi(\mathbf{r}_0)|^2 \rho_S(E_F) = \rho_S(E_F, \mathbf{r}_0) \quad (2.45)$$

where $\rho_S(E_F, \mathbf{r}_0)$ is the local density of states (LDOS) of the sample at the Fermi level at the center of curvature of the tip. This is the main result of the Tersoff-Hamann model.

Following the discussion in the latter part of section 2.1.1, if we apply a finite sample bias V and the tip-sample junction is under finite temperature T , then we can write the tunneling current as

$$I = \frac{4\pi e}{\hbar} \int_0^{eV} \rho_T(E_F - eV + \varepsilon) \rho_S(E_F + \varepsilon) |\psi(\mathbf{r}_0)|^2 d\varepsilon . \quad (2.46)$$

The differential conductance of the tunnel junction is then given by

$$\frac{dI}{dV} \propto \text{LDOS}(E_F + eV, \mathbf{r}_0) . \quad (2.47)$$

Equation (2.47) is the extension of the Tersoff–Hamann model to finite bias voltage. It states that the tunneling conductance at bias voltage V is proportional to the local density of states of the sample at the energy level $E_F + eV$ at the center of curvature of the tip. It is one of the most significant results upon which dI/dV spectroscopy and dI/dV mapping are based on.

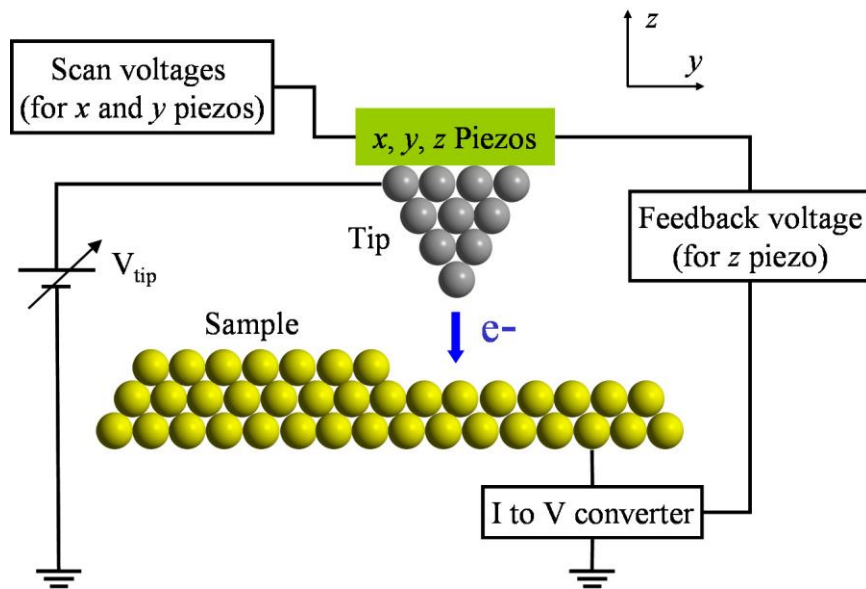
2.2 Basic Principles of STM

STM is a unique instrument that enables the study of atomic-scale structural and electronic properties of nanomaterials. It is capable of making three significant measurements. They are STM topography, dI/dV spectroscopy, and dI/dV maps.

2.2.1 STM topography

An STM consists of an atomically-sharp tip and a conducting surface that are placed very close to each other (on the order of several Ångströms). Figure 2.3 shows the basic setup of an STM. The xy -plane represents the sample surface and the z -direction is the direction perpendicular to the surface. Voltages are applied to the x , y and z piezos to move the tip in the x , y and z direction respectively. In addition to this a constant bias voltage (V_{tip}) is applied between the tip and sample. Upon application of this bias voltage (V_{tip}), electrons tunnel between the tip and sample. This tunneling current exponentially depends on the tip-sample distance. Thus, the tunneling current (after being converted to voltage) enters the feedback loop. While the tip moves in the xy -plane, the feedback provides voltage to the z -piezo to move the tip in the z -direction so as to keep the tunneling current constant. Hence, by plotting the variation of the z -position of the tip as a function of x and y co-ordinates we obtain the constant-current topograph.

One can also record STM topography in constant-height mode. In this mode of operation, the feedback circuit is turned off to keep the z -position constant during scan. Thus, by plotting the amplitude of the tunneling current as a function of x and y co-ordinates we obtain the constant-height topograph.



Chapter 2-Scanning Tunneling Microscopy (STM)

Figure 2.3 Diagram of basic STM set-up. Adapted from reference [71].

2.2.2 dI/dV spectroscopy

dI/dV is a spectroscopic technique that enables the study of electronic properties of materials on a surface. In this technique we keep the tip fixed at a desired position in the xy plane. We then sweep the bias voltage and record dI/dV as a function of the voltage. In order to minimize the noise we do not numerically differentiate $I(V)$, but instead use a lock-in amplifier to measure dI/dV directly. Because of the following relation;

$$\left. \frac{dI}{dV} \right|_V \propto LDOS_{sample}(E_F + eV),$$

dI/dV spectroscopy actually measures a sample's LDOS as a function of energy at a particular location within the sample.

2.2.3 dI/dV maps

dI/dV mapping is a technique that enables us to plot the spatial distribution of LDOS at a particular energy level. It maps the intensity of LDOS at a particular energy as a function of position on a pre-determined surface.

One of the most common ways of taking dI/dV maps is by keeping the sample bias constant at a particular value, say V_a , and scanning the x and y directions with the feedback on while measuring $dI(V_a)/dV$. This method provides both a topographic image as well as a dI/dV map at the voltage V_a simultaneously. This method is ideal for samples with large height variations or for systems having high thermal drift, and can be performed quickly.

The second method of recording dI/dV maps is called the multi-voltage dI/dV map. As its names suggest, in this approach there are two voltages: voltage V_a that determines the surface over which we are measuring the dI/dV signal, and voltage V_b that determines the energy at which we are measuring the dI/dV signal. In this method (with the feedback on) the sample bias is set to V_a and the current to I_a and an equally spaced grid of (x,y) co-ordinates is chosen. For each (x,y) point in the grid the feedback is turned off and the sample bias is then ramped from V_a to V_b . $dI(V_b)/dV$ is then measured after which the sample bias is changed back to V_a . The feedback is then turned back on and the tip is moved to the next coordinate. Thus, we are able to record the dI/dV map at the voltage V_b along the surface displayed by the STM topograph at $V=V_a$ and $I=I_a$. This method is relatively slower than the first method but offers more flexibility to choose the surface and energy over which we measure the LDOS.

Chapter 2-Scanning Tunneling Microscopy (STM)

2.3 Instrumentation

Throughout my graduate career, I principally worked with two STM instruments, as follows:

- 1) Home-built VTSTM: This is a home-built variable-temperature STM that operates in ultra-high vacuum (UHV). The original STM design and construction was carried out by Michael F. Crommie, Katsumi Nagoka, Hadrian Knotz, and David Kwon . Significant modifications to the STM were made by Matt Comstock [72], Niv Levy [73], Luis Berbil-Bautista, Jong Cho [74], Ivan Pechenezhskiy [75] and Giang D. Nyugen [76] . The project describing the bottom-up synthesis and characterization of GNRs was performed in this STM.
- 2) Home-built LTSTM: This is a home-built STM operated in UHV at a base temperature of 7K. This machine was designed and built by Michael F. Crommie, Wei Chen and Vidya Madhavan. Details about this STM can be found in the Ph.D. theses of Wei Chen [106], Vidya Madhavan [107], Tiberiu Jamneala [108], Michael Grobis [109], Ryan Yamachika [110], and Yen-Chia Chen [10]. The project describing the bottom-up synthesis and characterization of COFs was performed in this STM.

Chapter 3-Scattering Scanning Near-field Optical Microscopy (s-SNOM)

3.1 Introduction

Scanning near-field optical microscopy (SNOM) is a powerful technique that combines scanning probe microscopy (SPM) with spectroscopy to provide sub-diffraction-limited spatial resolution information about optical properties of materials. It is a combination of near-field optical microscopy and scanning probe microscopy. In near-field optical microscopy, a small aperture (smaller than the wavelength of light) is placed in close proximity to the sample surface. The aperture then interacts with the near-field of the sample and scatters the light into the far-field where it is detected. In order to obtain precise mechanical control of the sample and the probe, the near-field microscopy technique is coupled with scanning probe techniques such as atomic force microscopy (AFM) [77, 78] thus giving rise to near-field scanning optical microscopy (NSOM) [79].

The idea of using a small aperture to probe the near-field and beat the diffraction limit was originally proposed by Edward Synge in 1928 [80] (Figure 3.1(a)). The initial NSOM technique, known as aperture NSOM, measured the near-field through a tiny aperture. In this method, the probing tip has an aperture running through its center. This aperture acts as a waveguide into which near-field light is coupled (Figure 3.1(b)) The resolution in this technique directly scales as the radius of the aperture. Better resolution thus requires decreasing the radius of the aperture, but this in turn decreases the near-field signal [81]. Hence, in order to overcome this problem a new NSOM technique, known as scattering scanning near-field microscopy (s-SNOM) was developed in the 1990's [82]. In this method, the light scattered from the tip's apex is used in order to convert the near-field into a measurable far-field signal (Figure 3.1(c)). In s-SNOM the spatial resolution depends on the radius of tip apex. Thus, in this technique sharper tips give higher resolution without compromising the intensity of the near-field signal [79]. The theoretical models that describe the s-SNOM interaction are the tip spheroid model [83], the simple dipole model [81] and the extended monopole model [84].

Chapter 3-Scattering Scanning Near-field Optical Microscopy (s-SNOM)

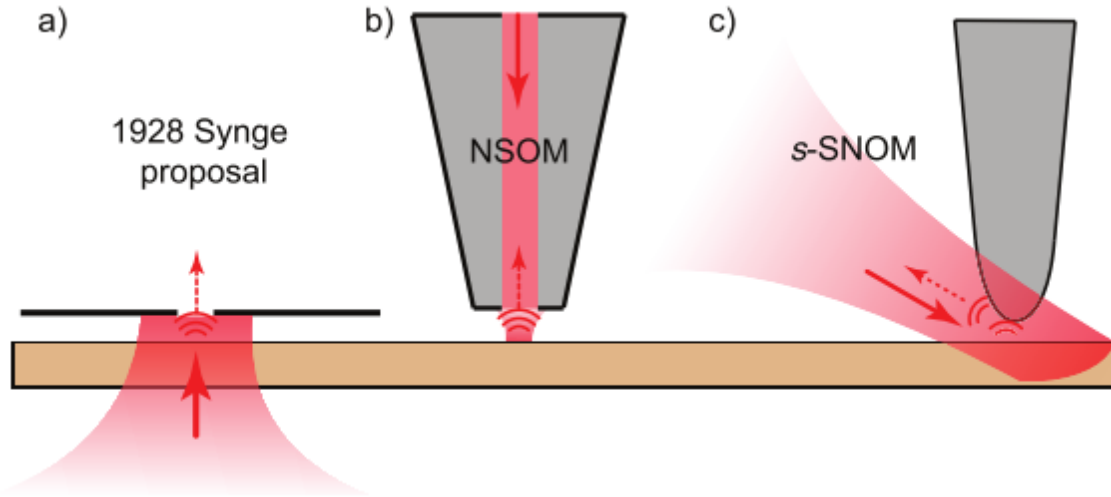


Figure 3.1 Different NSOM techniques (a) The experimental schematic for Syngé's original 1928 proposal for sub-diffraction imaging based on a sub-wavelength size aperture. (b) Schematics of the general experimental implementations for aperture-based NSOM based on a tapered optical fiber. (c) Scattering-based *s*-SNOM near-field microscopy. Figure taken from reference [85].

3.2 Basic Working Principle

In an *s*-SNOM light is focused onto the apex of a sharp metal-coated AFM tip. The AFM is then operated in the tapping mode in which the cantilever holding the tip is oscillated at a resonant frequency Ω . The scattered near-field signal is inversely proportional to the tip-sample distance. It is strongest when the tip is close to the sample and its intensity decreases with increase in the tip-sample distance. Thus, the optical signal at the detector, $|E_{sca}(t)|$, is a combination of the distance dependence of the near-field scattering $I(z)$ (Figure 3.2(a)) and the sinusoidal tip motion $z(t)$ (Figure 3.2(b)). If we take the Fourier transform of the non-linear signal then we obtain signal peaks at frequency $n\Omega$ ($n=\text{int.}$) (Figure 3.2(b)). Because the weak *s*-SNOM signal is embedded in the undesirable background signal, a lock-in detection is used to extract the *s*-SNOM signal at harmonics of the atomic force microscope tip oscillation frequency Ω [79].

Chapter 3-Scattering Scanning Near-field Optical Microscopy (s-SNOM)

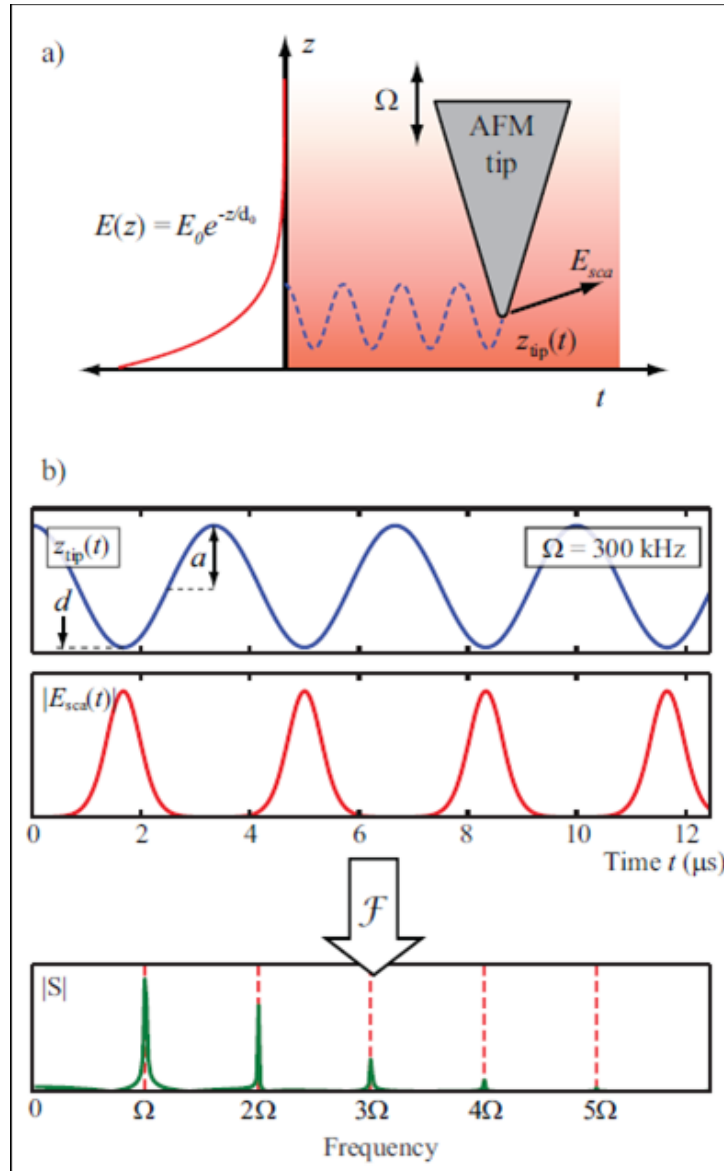


Figure 3.2 Basic Working Principle of s-SNOM (a) dependence of the near-field scattering $I(z)$ on the tip-sample distance combined with (b) the sinusoidal tip motion, $z(t)$ gives the optical signal $|E_{sca}(t)|$. Fourier transform of the non-linear signal gives signal peaks at frequency $n\Omega$ ($n=\text{int.}$). Figure after reference [85].

3.3 Self-homodyne and homodyne measurements of near-field signal

In our near-field measurements, we used self-homodyne and homodyne detection schemes that are extensively used in other near-field measurement studies since they yield high-quality near-field images. The self-homodyne scheme incorporates the near-field light E_n together with background light E_b . The total field, $E_n + E_b$, is scattered by the AFM tip, and is collected by a HgCdTe detector. The collected signal I is proportional to the intensity of the total field, $|E_n + E_b|^2$, of which an explicit form is given by

$$I \propto |E_n + E_b|^2 = |E_n|^2 + |E_b|^2 + 2|E_n||E_b|\cos(\theta_n - \theta_b) \quad (3.1)$$

where θ_n and θ_b are the arguments of E_n and E_b , respectively. The contribution from the first term of the right-hand-side is negligibly small, and the second term also yields a very small contribution at higher order frequencies $n\Omega$ where Ω is the tapping frequency of the AFM tip. Therefore, the measured signal is mainly contributed by the cross term. When the scanning area is in the deep sub-wavelength then $|E_b| \gg |E_n|$ and the detected signal can be strongly enhanced by the background light. However, since θ_b is not a constant over the measuring area, there is a possibility that the measured signal is hampered by interference fringes coming from the spatially-varying phase, $\theta_n - \theta_b$. In order to check the validity of results from the self-homodyne measurements, we also must use homodyne detection. In the homodyne detection, a reference beam E_{ref} is incorporated as the amplification beam. The total signal collected by the HgCdTe detector is now proportional to

$$\begin{aligned} I &\propto |E_n + E_b + E_{ref}|^2 \\ &= |E_n|^2 + |E_b|^2 + |E_{ref}|^2 \\ &\quad + 2|E_b||E_{ref}|\cos(\theta_b - \theta_{ref}) + 2|E_n||E_b|\cos(\theta_n - \theta_b) + 2|E_n||E_{ref}|\cos(\theta_n - \theta_{ref}). \end{aligned}$$

where θ_{ref} is the phase of the reference beam. The first term gives only a negligible contribution. The next three terms do not depend on the near-field signal, so that their contribution will be very small at high order frequencies $n\Omega$. The measured signal can then be approximately given by

$$I \propto 2|E_n||E_b|\cos(\theta_n - \theta_b) + 2|E_n||E_{ref}|\cos(\theta_n - \theta_{ref}) \approx 2|E_n||E_{ref}|\cos(\theta_n - \theta_{ref}). \quad (3.2)$$

The last approximation holds since the reference beam is usually much stronger than the background ($|E_{ref}| \gg |E_b|$).

Chapter 3-Scattering Scanning Near-field Optical Microscopy (s-SNOM)

During our experiment we recorded near-field images from both the self-homodyne and the homodyne schemes. Consistency between the near-field images obtained from the two techniques confirmed the validity of our experimental results.

Chapter 4-Graphene Nanoribbons

This chapter discusses my work on graphene nanoribbons(GNRs). GNRs are quasi-one dimensional strips of graphene with novel electronic and magnetic properties [3, 12, 86–89]. The researchers who contributed to these studies are Trinity Joshi, Dr. Ryan R. Cloke, Dr. Tomas Marangoni, Dr. Giang D. Nguyen, Daniel J. Rizzo, Dr. Christopher Bronner, Dr. Ting Cao, Dr. Francesca M. Toma, Zahra Pedramrazi, Dr. Chen Chen, Dr. Yen-Chia Chen, Dr. Marco Favaro, Dr. Steven G. Louie, Dr. Michael F. Crommie, and Dr. Felix R. Fischer.

Ever since the first report of bottom-up synthesis of graphene nanoribbons by Cai et. al [3], researchers around the world have heavily invested their resources to fabricate graphene nanoribbons with different width [3, 26, 90] and edge symmetry [3, 25, 26]. However, to incorporate these nanoribbons in device configuration we need a method to modulate their band structure and charge carrier concentration by substituting specific carbon atoms in the hexagonal graphene lattice with n- or p-type dopant heteroatoms. In this chapter, I will report two such projects where the graphene nanoribbons were doped with boron and sulphur atoms. The first section describes the detailed study of boron-doped $N = 7$ AGNRs, where the AGNRs are substitutionally doped with boron atoms in their backbone. The second section focuses on the study of sulfur-doped $N = 13$ GNRs, where the sulfur atoms substitutionally dope the edges of the GNRs.

4.1 Bottom-Up Synthesis of $N = 7$ Boron-Doped Graphene Nanoribbons

I will first discuss the bottom-up fabrication and electronic structure characterization of atomically defined hydrogen terminated $n = 7$ armchair GNRs (7 -AGNRs, n corresponds to the number of carbon atoms across the width of the ribbon) featuring a regioregular pattern of B atoms along the central backbone of the ribbon on a Au(111) surface. The work described below was originally published in ref. [27].

4.1.1 Introduction

Recent advances in the bottom-up fabrication of atomically precise GNRs from molecular precursors have yielded new technique for the incorporation of nitrogen atom dopants in the form of pyridine and pyrimidine rings into the edges of chevron-GNRs [91–93]. Since the lone-pair of the N-heteroatom in these structures is not in conjugation with the extended π -system of the GNR, edge-doping only shifts the position of both the conductance and valence band edges of the ribbon without introducing dopant states into the gap [91]. Controlled n-/p-doping, i.e., the controlled introduction of filled/empty donor or acceptor states into the gap of atomically defined GNRs,

Chapter 4-Graphene Nanoribbons

instead requires the incorporation of dopant heteroatoms at precise positions along the backbone of the ribbon where the filled/empty p-orbitals are in conjugation with the extended π -system.

In this chapter, I will report the bottom-up synthesis and characterization of atomically defined hydrogen terminated $n = 7$ armchair GNRs featuring a regioregular pattern of B atoms along the central backbone of the ribbon. This synthesis of B-doped 7-AGNRs (B-7AGNRs) was carried out by the thermally induced radical step-growth polymerization/cyclization of the molecular precursor, 5,10-bis(10-bromoanthracene-9-yl)-5,10-dihydroboranthrene (**1**, Figure 4.2(a)), on Au(111) in ultra-high vacuum (UHV). Low-temperature scanning tunneling microscopy (STM) imaging of fully cyclized B-doped 7-AGNRs (B-7AGNRs) reveals a unique, characteristic stripe pattern along the length of the ribbon with a period corresponding to the distance between the expected position of dopant atoms in the molecular repeat unit (Figure 4.2(d), (e)). This is consistent with the empty p-orbitals of boron conjugating to the extended π -system of the 7-AGNR and acting as substitutional dopants. Density functional theory (DFT) calculations reveal that B-7AGNRs have a deep acceptor band at energies within the gap of undoped 7-AGNRs, which is localized along the backbone of a B-7AGNR and verified experimentally through dI/dV imaging.

4.1.2 Molecular Synthesis

The boron-doped 7-AGNR precursor **1** (Figure 4.2(a)) was obtained through selective monolithiation of 9,10-dibromo-anthracene (**2**), followed by borylation with 5,10-dibromo-5,10-dihydroboranthrene (**3**) in 73% yield (Figure 4.1). Despite the reported instability of this class of substituted boranthrenes, crystals of **1** are stable in air at 24 °C showing no signs of degradation over several months, as indicated by ^1H NMR spectroscopy [94–96]. DSC and TGA analysis reveals a melting point above 350 °C and a gradual mass loss associated with partial dehalogenation above this temperature.

Synthesis of the molecular precursors (**1**) was performed by the F. Fischer group. Orange crystals of **1** suitable for X-ray diffraction were obtained by slow evaporation of a $\text{C}_2\text{H}_2\text{Cl}_4$ solution (Figure 4.1). **1** adopts a C_i symmetry in the crystal lattice. The geometry around the boron atom is trigonal-planar with bond angles and bond distances ranging between 119.7–120.9° and 1.56–1.78 Å, respectively. While the two 9-bromoanthracene units are coplanar, the central boranthrene is twisted out of planarity with a dihedral angle $\text{C}(2)\text{--C}(1)\text{--B}(1)\text{--C}(15) = 97.6^\circ$ (Figure 4.1). This nonplanar conformation is crucial as it sterically shields the Lewis acidic B atoms from nucleophilic attack and imparts a favorable nonplanar geometry to the molecule, prerequisite for an efficient radical step-growth polymerization on the Au(111) substrate [3, 18, 102, 103, 26, 91, 92, 97–101].

Chapter 4-Graphene Nanoribbons

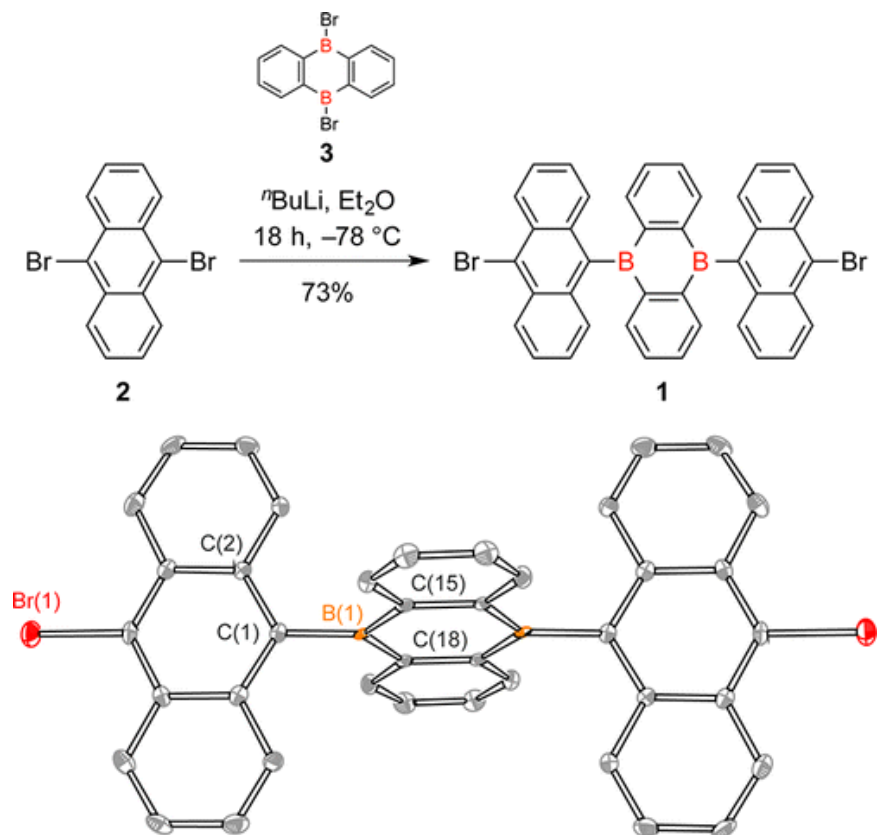


Figure 4.1. Synthesis of the B-doped molecular precursor **1** (top). ORTEP representation of the X-ray crystal structure of **1** (bottom). Thermal ellipsoids are drawn at the 50% probability level. Color coding: C (gray), Br (red), B (orange). Hydrogen atoms and co-crystallized solvent molecules are omitted for clarity. Relevant structural parameters: C(1)–B(1), 1.578(5) Å; C(15)–B(1), 1.561(5) Å; C(18)–B(1), 1.562(5) Å; C(2)–C(1)–B(1)–C(15), 97.6°; $\text{C}_{46}\text{H}_{30}\text{B}_2\text{Br}_2\text{Cl}_{12}$; 1189.54 g mol⁻¹; triclinic; P-1; orange; a = 8.6046(3) Å; b = 9.8632(4) Å; c = 14.5013(6) Å; $\alpha = 82.148(2)^\circ$, $\beta = 82.067(2)^\circ$; $\gamma = 74.011(2)^\circ$; 100 (2) K; Z = 1; R1 = 0.0387; GOF on $F^2 = 1.036$.

4.1.3 Bottom-up Fabrication of B-7AGNRs on Au(111)

Fully cyclized B-7AGNRs were fabricated by sublimation of molecular building block **1** at 250–270 °C in UHV onto pristine Au(111) held at 24 °C. STM imaging at 13 K prior to polymerization reveals that the molecules assemble into irregular islands with an apparent height of 0.4 nm (Figure 4.2(b)), clustered around the Au(111) herringbone reconstruction. Gradual annealing of submonolayer samples of **1** on Au(111) to 220 °C (20 min) induces homolytic cleavage of the labile C–Br bond, followed by step-growth polymerization of the carbon-centered diradical intermediates to form extended linear polymer chains poly-**1** (Figure 4.2(c)). STM

Chapter 4-Graphene Nanoribbons

images of polymer chains display a characteristic pattern of alternating protrusions (average distance between white markers 0.95 ± 0.04 nm, Figure 4.2(d)) along the polymer backbone. The repulsive interaction between peri-hydrogen atoms in adjacent anthracene units prevents a coplanar arrangement of monomer units in the polymer backbone (this observation is consistent with images of polyanthracene, the precursor to undoped 7- AGNRs [3, 97, 98]. Unique to the B-doped GNR precursors is a distinctive secondary structure along the polymer that correlates with the length of a monomer unit (Figure 4.2(a)) in poly-**1** (average distance between black markers 1.40 ± 0.04 nm, Figure 4.2(d)). While the anthracene fragments appear as brighter spots in topographic STM images, the more electron-deficient boranthrenes correlate with a weaker signal that alternates along the edges of the polymer. The observation of this characteristic secondary pattern in images of poly-**1** indicates that the exocyclic B–C bonds are stable under the polymerization conditions and no undesired fragmentation of monomer building blocks is observed during the step-growth process.

Chapter 4-Graphene Nanoribbons

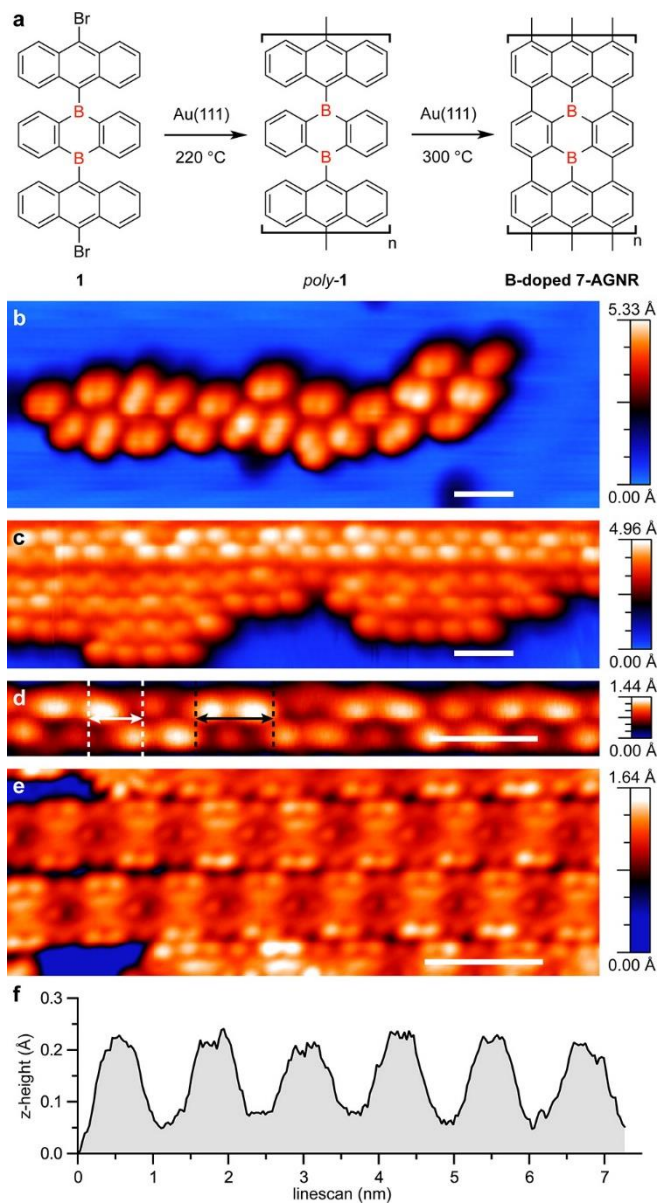


Figure 4.2 Bottom-up synthesis of B-7AGNRs (a) Schematic representation of the bottom-up synthesis of B-7AGNRs. (b) STM topographic image of molecular building block 1 as deposited onto a pristine Au(111) surface held at 24 °C (sample voltage $V_s = 1.5$ V, tunneling current $I_t = 30$ pA, imaging temperature $T = 13$ K). Subsequent annealing steps induce the homolytic cleavage of the labile C–Br bonds, followed by radical step-growth polymerization (220 °C) and thermal cyclization/dehydrogenation (300 °C) to yield B-7AGNRs. (c) STM topographic image of *poly-1* ($V_s = 1.0$ V, $I_t = 20$ pA, $T = 13$ K). (d) STM topographic image of *poly-1* showing a characteristic pattern of alternating protrusions ($V_s = 1.0$ V, $I_t = 20$ pA, $T = 13$ K). (e) STM

Chapter 4-Graphene Nanoribbons

topographic image of fully cyclized B-7AGNRs $V_s = -0.1$ V ($V_s = -0.1$ V, $I_t = 3$ pA, $T = 4.5$ K). (f) Representative z-axis profile showing the characteristic height modulation along the long axis of a B-7AGNR. Scale bar is 2 nm.

Further annealing of the Au(111) substrate at 300 °C (20 min) induces a thermal cyclization/dehydrogenation sequence that converts *poly-1* into fully conjugated B-7AGNRs (Figure 4.2(e)). The apparent width and average height of the resulting GNRs are 1.6 nm and 0.16 ± 0.04 nm, respectively. Statistical analysis of large area STM images of densely packed ribbons shows that the majority of B-7AGNRs ranges in length between 4–12 nm with a few examples exceeding 16 nm (Figure 4.3). STM topography at negative bias reveals a characteristic stripe pattern corresponding to a height modulation (amplitude 0.14 ± 0.02 Å) along the length of the B-7AGNRs (Figure 4.2(f)). The periodicity of this topographic feature, 1.30 ± 0.05 nm, correlates with the expected spacing between boranthenene units along the backbone of a B-7AGNR (Figure 4.2(a))

Chapter 4-Graphene Nanoribbons

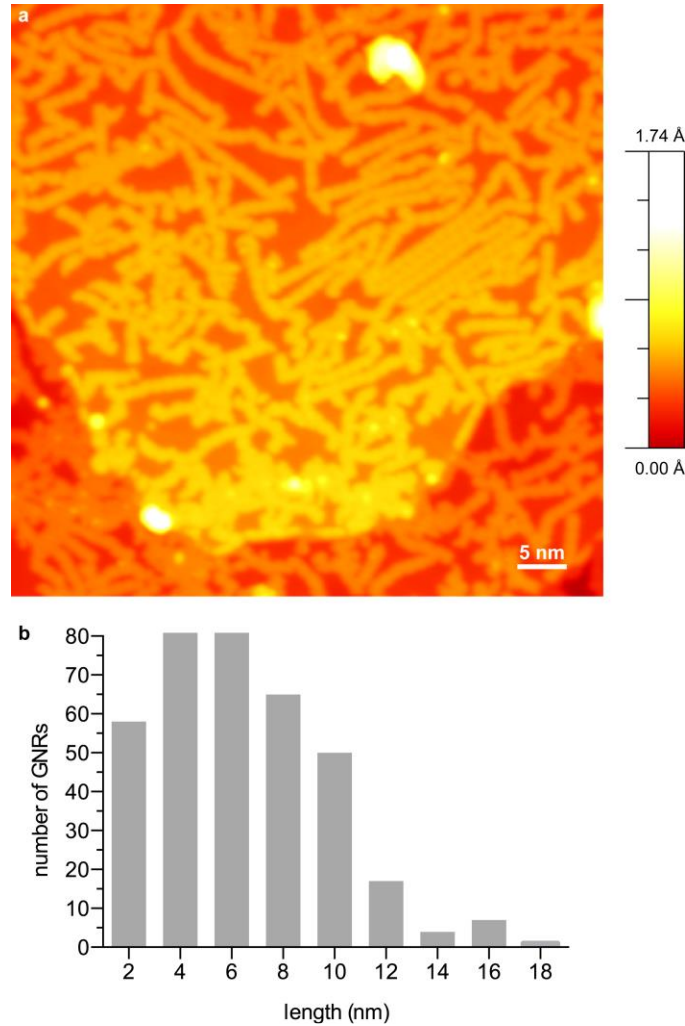


Figure 4.3 Statistical analysis of B-7AGNRs STM images (a) Large area STM of B-7AGNRs on Au(111) surface ($V_s = 1.5$ V, $I_t = 5$ pA, $T = 4.5$ K). (b) Statistical analysis of the length distribution of B-7AGNRs on Au(111).

4.1.4 DFT Calculation for B-7AGNRs

In order to better understand the electronic effects of substitutive B-doping in B-7AGNRs, we performed first principles calculations based on the GW approximation and included the screening effects from the underlying Au(111) substrate [18] (these calculations were performed by the Louie group). The total density of states (DOS) at the GW level for a B-7AGNR is depicted in Figure 4.4(a). The DOS of both the valence (VB) and the conduction (CB) bands show significant contributions ($\sim 10\%$) from B atoms. Comparing to the electronic structure of a pristine 7-AGNR (Figure 4.4(a)), substitutive B-doping along the backbone of a 7-AGNR introduces a

Chapter 4-Graphene Nanoribbons

deep acceptor band (CB) 0.8 eV above the VB maximum. The theoretically predicted quasiparticle band gap of B-7AGNRs, 0.8 eV (Figure 4.4(b)), is significantly smaller than that of the undoped 7-AGNRs (~ 2.1 eV) calculated with the same method (the undoped 7-AGNR DOS is shown in Figure 4.4(a)).

The spatial distribution of the states associated with both the conductance band (CB) and the CB+1 band was investigated by dI/dV mapping. Figure 4.4(c) shows a B-7AGNR dI/dV map at $V_g = 1.0$ V, corresponding to states in the CB. The dI/dV map shows a predominance of local density of states (LDOS) along the backbone of the ribbon. This can be compared to the CB LDOS map calculated for a given energy range at a distance of 4 Å above a B-7AGNR plane (Figure 4.4(d)). In strong contrast to undoped 7-AGNRs [98], both the experimental and theoretical LDOS maps at this energy show significant higher state density along the backbone of the B-7AGNR. Atomic scale features are not well-resolved experimentally, likely due to tip-induced broadening and substrate interactions that are not accounted for in the calculation. The dI/dV map recorded at a higher bias of $V_g = 1.6$ V (corresponding to an energy closer to CB+1) shows strong localization of the LDOS along the edges of the B-7AGNR (Figure 4.4(e)). This agrees with the calculated LDOS map of B-7AGNR CB+1 states (Figure 4.4(f)) and is reminiscent of band edge LDOS observed in undoped 7-AGNRs [98]. These spectroscopic maps provide additional evidence that the substitution of C atoms with trigonal planar B atoms in GNRs induces a change in their electronic structure.

Chapter 4-Graphene Nanoribbons

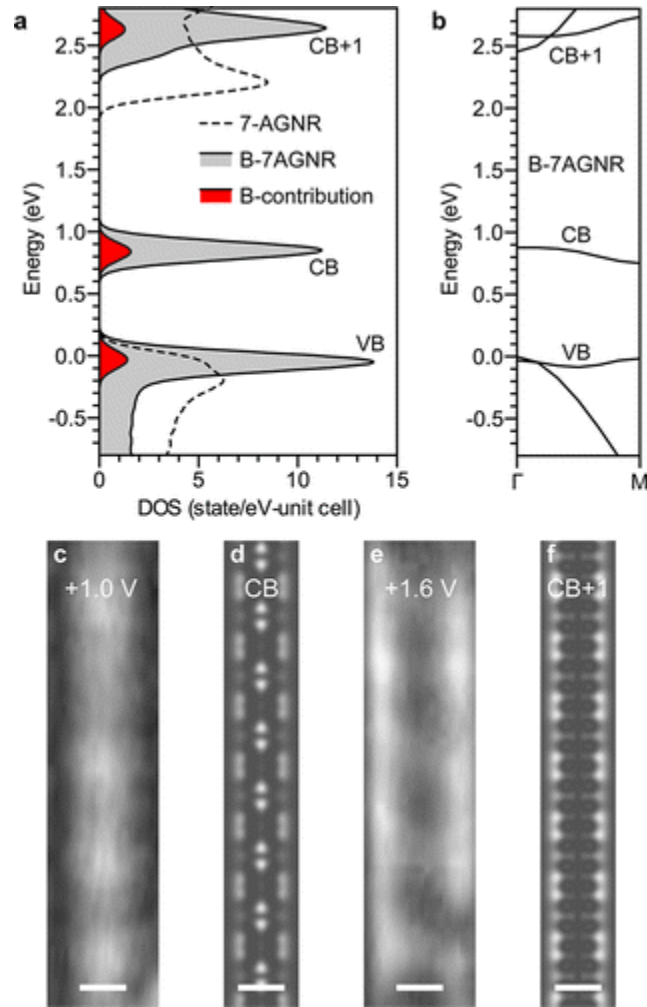


Figure 4.4. Experimental and theoretical electronic structure of B-7AGNRs (a) Calculated total DOS for B-7AGNRs (gray) and contribution from B atoms to the DOS (red) using the GW approximation and including screening effects from Au(111) substrate. The total DOS for undoped 7-AGNRs is plotted as a dotted line. A Gaussian broadening of 0.1 eV is applied. The valence band maximum is set to 0 eV. (b) Calculated quasiparticle band structure of B-7AGNRs (using GW approximation). (c) dI/dV spatial map of B-7AGNR recorded at 1.0 V ($I_t = 30$ pA, modulation voltage $V_{rms} = 15$ mV, modulation frequency 634 Hz, $T = 13$ K). (d) Calculated LDOS map of states at the conduction band edge (CB) at a height of 4 Å above a B-7AGNR plane. (e) dI/dV spatial map of same B-7AGNR as in (c) recorded at 1.6 V ($I_t = 30$ pA, modulation voltage $V_{rms} = 15$ mV, modulation frequency 634 Hz, $T = 13$ K). (f) Calculated LDOS maps of CB+1 bandedge states at a height of 4 Å above a B-7AGNR plane. Calculated images average states over an energy range of 0.1 eV, scale bar 1 nm.

Chapter 4-Graphene Nanoribbons

4.1.4 Summary

In conclusion, we have demonstrated atomically precise bottom-up synthesis of 7-AGNRs with dopant atoms inserted directly into the GNR backbone. The trigonal planar B atoms incorporated at defined positions along the GNR share an empty p-orbital with the extended π -system, potentially providing hole dopant concentrations in excess of 10^{14} cm^{-2} . The highly regular placement of p-dopants along the 7-AGNR is reflected in a characteristic modulation of the LDOS along the backbone of the ribbon visualized by STM topographic imaging.

4.2 Bottom-Up Synthesis of $N = 13$ Sulfur-Doped Graphene Nanoribbons

In this section, I will discuss our work involving the fabrication and nanoscale characterization of atomically precise $N = 13$ armchair GNRs featuring regioregular edge-doping of sulfur atoms (S-13-AGNRs) on a Au(111) surface. The work described below was originally published in ref. [28].

4.2.1 Introduction

The edge-doping in bottom-up fabricated GNRs has exclusively relied on the introduction of nitrogen heteroatoms in the form of pyridine and pyrimidine rings along the edges of chevron GNRs [91–93]. In this position, the electron lone pair on the trigonal planar nitrogen atoms is not in conjugation with the GNR aromatic π -system. Rather than significantly affecting the GNR DOS or energy gap, the electronegative N atoms only induce a rigid shift of the energies of both the valence and conduction bands [91].

In this chapter, we report the bottom-up synthesis and characterization of atomically precise $N = 13$ armchair graphene nanoribbons (S-13-AGNRs) wherein alternating $(\text{CH})_2$ groups lining the edges of the GNRs have been replaced by sulfur atoms. This alternative edge-doping pattern places one of the lone pairs (having p-character) on trigonal planar S atoms in full conjugation with the extended π -system of the 13-AGNR. Molecular precursors for S-13-AGNRs (**1** in Figure 4.5) are derived from 10,10'-dibromo-9,9'-bisanthracene and feature (2-phenyl)thiophene substituents. A sub-monolayer of **1** was deposited onto a Au(111) surface under ultrahigh vacuum (UHV). Subsequent heating of the decorated Au(111) surface to 200 °C induces a radical step growth polymerization to give poly-**1**. A second annealing step (400 °C) induces a thermal cyclodehydrogenation to yield fully conjugated S-13-AGNRs. Both scanning tunneling microscopy (STM) and scanning tunneling spectroscopy (STS) were used to investigate the structure and to probe the electronic states of the resulting S-13-AGNRs. STS measurements reveal a LUMO state (lowest unoccupied molecular orbital) for S-13-AGNRs at approximately the same energy as that previously recorded for undoped 13-AGNRs. When compared to undoped 13-

Chapter 4-Graphene Nanoribbons

AGNRs, the density of states (DOS) associated with the LUMO in S-13-AGNR spans a significantly broader energy range. These results are consistent with *ab initio* simulations of S-13-AGNRs that indicate a sulfur-induced increase in the energy separation between CB and CB+1 as well as between the VB and VB-1 13-AGNR band edges (here, CB refers to the conduction band, and VB refers to the valence band).

4.1.2 Molecular Synthesis

Synthesis of the molecular precursors (**1**) was performed by the F. Fischer group. The molecular precursor for S-13-AGNRs **1** (Figure 4.5) was synthesized through a Suzuki cross-coupling of 2,2',10,10'-tetrabromo-9,9'-bianthracene (**2**) with 2 equiv of (2-(thiophen-2-yl)phenyl)boronic acid (**3**). Oxidative addition favors the sterically less hindered 2,2'-position in the bisanthracene backbone and yields the desired regioisomer **1** as the major product in 44% yield.

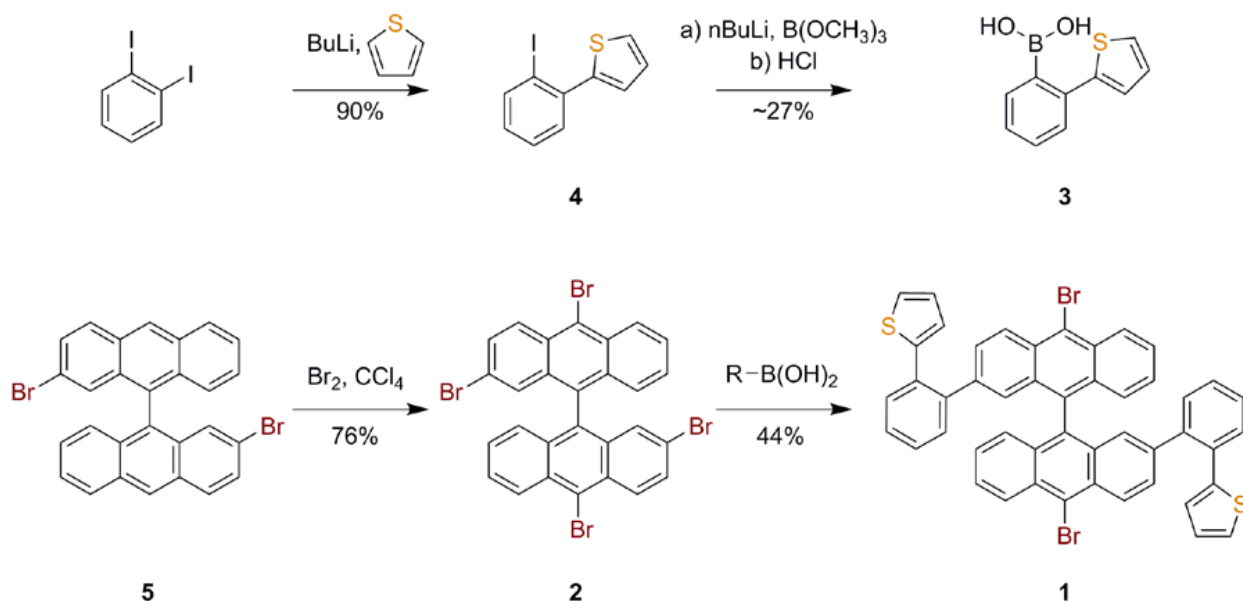


Figure 4.5 Synthesis of **1**

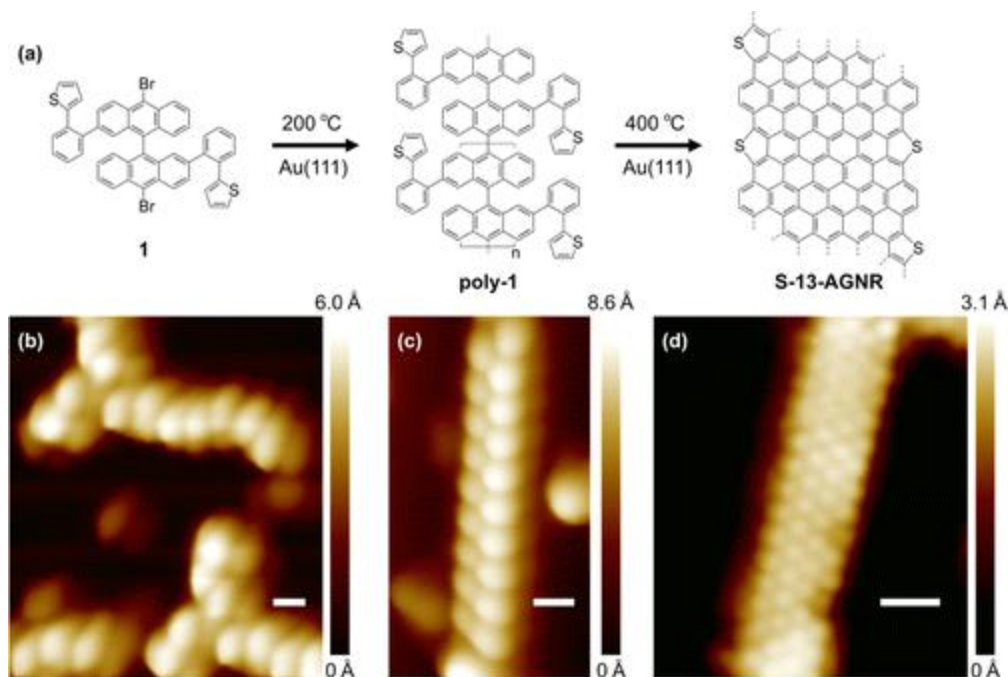
4.2.3 Bottom-up Fabrication of S-13-AGNRs on Au(111)

A polished Au(111) single crystal was used as the substrate for the STM measurements. Standard Ar⁺ sputtering/annealing cycles were applied to prepare an atomically clean Au(111) surface. The molecular building block **1** was evaporated from a home-built Knudsen cell evaporator, and the deposition rate was calibrated in a test chamber using a quartz crystal microbalance. Compound **1** was sublimed at 478 K onto a 298 K Au(111) substrate under UHV for about 2 min to obtain 30–90% coverage. STM measurements were performed on two home-

Chapter 4-Graphene Nanoribbons

built low temperature STMs operating at 13 and 7 K. Both tungsten and PtIr tips were used for STM topographic measurements in constant current mode. The dI/dV spectra were recorded using a tungsten tip and measured with a lock-in amplifier under open-feedback conditions. WSxM was used to process all STM images.

Figure 4.6(b) shows a STM image of **1** on Au(111) as deposited. The molecules tend to aggregate into irregular islands along the Au(111) herringbone reconstruction with an average height of 0.5 nm. Annealing the molecule-decorated sample at 200 °C for 20 min induces homolytic cleavage of the labile C–Br bonds in **1** followed by radical step growth polymerization of the intermediate diradical to give poly-**1** (Figure 4.6(a)). A representative STM image of a linear chain of poly-**1** on Au(111) is depicted in Figure 4.6(c). Analogous to the polymer precursor for undoped 13-AGNRs, poly-**1** exhibits a pattern of alternating protrusions associated with the preferred conformation of the (2-phenyl)thiophene substituents on the Au(111) surface (the periodicity of the protrusions is 0.83 ± 0.02 nm with an apparent height of 0.43 ± 0.02 nm) [3, 26, 27]. Further annealing of Au(111) samples at 400 °C for 20 min induces a thermal cyclodehydrogenation that converts poly-**1** into fully cyclized S-13-AGNRs (Figure 4.6(d)). The average height and width of the resulting S-13-AGNRs are 0.23 ± 0.01 and 1.9 ± 0.2 nm, respectively, and are comparable with the dimensions previously reported for undoped 13-AGNRs (0.21 ± 0.01 and 1.9 ± 0.2 nm) [18, 26].



Chapter 4-Graphene Nanoribbons

Figure 4.6 Bottom-up synthesis of S-13-AGNRs (a) Reaction scheme for bottom-up synthesis of S-13-AGNRs. Annealing at 200 °C induces radical step growth polymerization. Annealing at 400 °C induces cyclodehydrogenation to yield S-13-AGNRs. (b) STM image of precursor 1 as deposited onto a Au(111) surface ($V_s = 2.0V$, $I_t = 20$ pA, $T = 13$ K) (c) STM image of poly-1 (after the first annealing step) shows the characteristic pattern of alternating protrusions ($V_s = 2.0V$, $I_t = 20$ pA, $T = 13$ K). (d) STM image of a fully cyclized S-13-AGNR ($V_s = 0.1V$, $I_t = 15$ pA, $T = 7$ K). Scale bars are 1 nm.

Statistical analysis of STM images shows that the average length of S-13-AGNRs obtained by this growth procedure is 5 nm (Figure 4.7 (c)). We observe some irregular edge structure in our samples following the final cyclodehydrogenation step (Figure 4.7 (a), (b)). These defects might arise from the additional strain induced along the edges of GNRs by the introduction of five-membered thiophene rings or by deletion of the thiophene ring through fragmentation of the (2-phenyl)thiophene C–C bond during the thermal annealing at 400 °C.

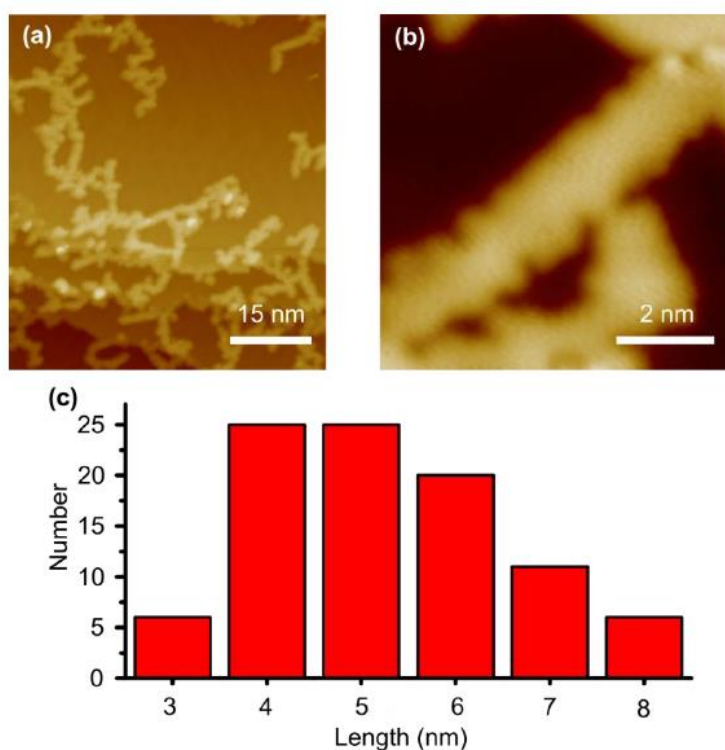
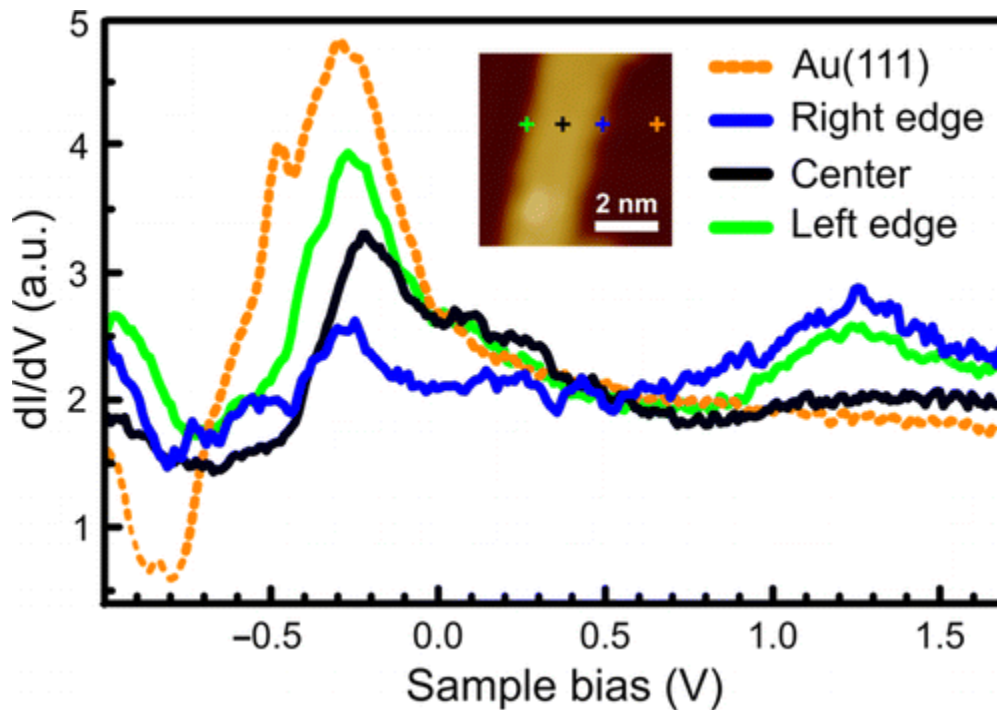


Figure 4.7 Statistical analysis of S-13-AGNRs STM images (a) Large scale STM topographic image of S-13-AGNRs ($V_s = -0.1V$, $I_t = 20$ pA, $T = 7$ K). (b) STM topographic image of a defective 13-S-AGNR ($V_s = -0.05$ V, $I_t = 35$ pA, $T = 7$ K). (c) Length distribution of S-13-AGNRs.

4.2.4 Local Electronic Structure of S-13-AGNR

The local electronic structure of S-13-AGNRs was characterized by recording dI/dV spectra at various positions above the S-13-AGNR decorated surface. Figure 4.8 shows typical dI/dV spectra measured at the center and edges of a S-13-AGNR compared to a reference spectrum measured with the STM tip placed above the bare Au(111) substrate. The Au(111) reference spectrum is dominated by a peak centered at a sample bias of $V = -0.3$ V that drops steeply for $V \leq -0.5$ V. This feature is known to originate from the Au(111) surface state [104], which has a band edge at 0.5 eV below the Fermi energy E_F (E_F corresponds to $V = 0$). All spectra recorded with the STM tip positioned above S-13-AGNRs show a peak for $V < 0$ that is similar to the peak observed when the tip is held above bare Au(111). This makes it difficult to discern whether this feature (when seen at locations above a S-13-AGNR) is due to the intrinsic S-13-AGNR electronic structure (such as the VB edge) or is due to the underlying Au(111) surface state. A more unambiguous S-13-AGNR spectral feature is observed at $V = 1.22 \pm 0.23$ V. Here, a peak can be seen in the dI/dV spectra at the S-13-AGNR edges that is not observed at either the S-13-AGNR center or in the Au(111) reference spectrum. This behavior is consistent with the spectral signature of GNR band edge states observed previously for $N = 5, 7,$ and 13 AGNRs [18, 26, 90, 98] and is assigned to the S-13-AGNR conduction band edge. This band edge feature lies at almost the same energy as the undoped 13-AGNR conduction band edge ($V = 1.21 \pm 0.06$ V) [26] but is significantly broadened with a full width at half-maximum (fwhm) of $\Delta E = 0.37 \pm 0.2$ eV compared to $\Delta E = 0.19 \pm 0.07$ eV for the undoped 13-AGNR.

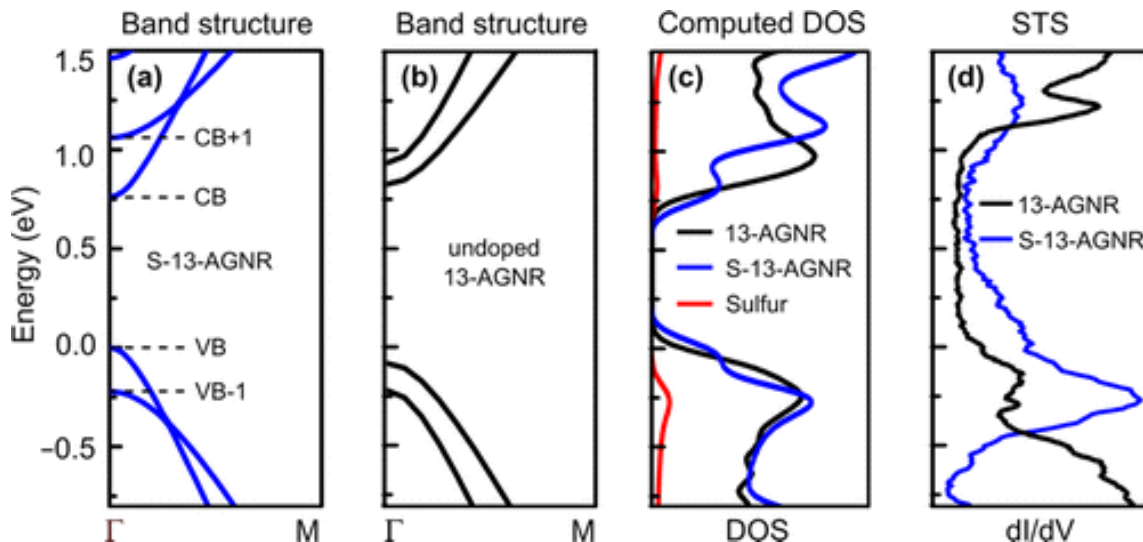


Chapter 4-Graphene Nanoribbons

Figure 4.8 STM dI/dV spectroscopy of S-13-AGNRs dI/dV spectra of S-13-AGNRs at different spatial positions compared to the reference spectrum obtained on bare Au(111). Crosses in the topographic STM image (inset) indicate the positions of recorded spectra ($T = 13$ K).

4.2.4 Theoretical Calculation and Comparison to Experimental Result

In order to better understand how the electronic properties of 13-AGNRs are affected by substitutional sulfur edge-doping, we performed density functional theory (DFT) calculations within the local density approximation (LDA) for both S-doped (Figure 4.9(a)) and undoped (Figure 4.9(b)) free-standing 13-AGNRs. Our calculations suggest that incorporation of sulfur atoms into the armchair edges only slightly reduces the band gap (at the DFT-LDA level) of a pristine 13-AGNR, from 0.90 to 0.76 eV. In addition, when referenced to the vacuum potential, the CB minimum and VB maximum of S-13-AGNRs have similar energy alignment compared to pristine 13-AGNRs. This behavior is quite different from the previously studied case of nitrogen edge-doped chevron GNRs, whose band edges undergo a nearly rigid shift of ~ -0.5 eV compared to undoped chevron GNRs [91]. This difference in behavior for N-doped and S-doped GNRs can be explained by the small difference in electronegativity between sulfur and carbon as compared to the large difference between nitrogen and carbon [105]. Furthermore, the sulfur edge-doping causes a significant increase in the energy difference between the CB and CB+1 band edges, as well as between the VB and VB-1 band edges, when compared with pristine 13-AGNRs (Figure 4.9). This modification to the electronic structure is due to the strong hybridization of S dopant orbitals with the aromatic network in S-13-AGNRs (Figure 4.9(c)) (due to conjugation of the S lone pair with the π -system).



Chapter 4-Graphene Nanoribbons

Figure 4.9 Theoretical electronic structure of S-13-AGNRs Computed band structures of (a) a S-13-AGNR and (b) a pristine 13-AGNR. (c) Calculated DOS of a S-13-AGNR (blue), the partial density of states (PDOS) of sulfur orbitals (red), and the DOS of a pristine 13-AGNR (black) (Gaussian broadened by 0.1 eV). (d) Experimental dI/dV spectrum for a S-13-AGNR (blue) compared to the dI/dV spectrum for a pristine 13-AGNR (black).

The calculated band structure of S-13-AGNRs is consistent with the experimentally observed dI/dV spectra of Figure 4.9(d). The experimental CB edge of S-13-AGNRs is very closely aligned with the CB edge observed for undoped 13-AGNRs (similar to the simulated DOS depicted in Figure 4.9(c)). The significant broadening of the experimental CB feature for S-13-AGNRs compared to that for undoped 13-AGNRs is consistent with the predicted increase in energy separation between the CB and CB+1 band edges for S-13-AGNRs as compared to that for undoped 13-AGNRs (Figure 4.9). The reason that the experimental measurement shows only a single feature instead of two peaks is likely due to broadening arising from interaction between S-13-AGNRs and the gold substrate [106].

4.2.5 Computational Methods

First-principles calculations of sulfur-doped GNRs were performed by the Louie group using DFT in the local density approximation implemented in the Quantum Espresso package [107]. A supercell arrangement was used, with the cell dimension carefully tested to avoid interactions between the nanoribbon and its periodic image. We used norm-conserving pseudopotentials [104], with a plane wave energy cutoff of 60 Ry. The structure was fully relaxed until the force on each atom was smaller than 0.02 eV \AA^{-1} . All of the σ dangling bonds of carbon atoms on the edge of the nanoribbon were capped by hydrogen atoms. The unit cell dimension along the periodic direction was fully relaxed. The cell sizes along the nanoribbon plane normal direction and edge normal direction were set to 13 and 30 \AA , respectively, in order to avoid interactions between the S-13-AGNR and its periodic images. The Gaussian broadening used in plotting the DOS was 0.1 eV.

4.2.5 Summary

Hence, we have demonstrated the successful bottom-up synthesis of substitutional sulfur edge-doped 13-AGNRs on Au(111), as well as determination of the effect of sulfur edge-doping on the electronic structure of $N = 13$ AGNRs. Both the theoretically determined and experimentally measured S-13-AGNR electronic structures are consistent with the hybridization of sulfur orbitals with the conjugated π -system of the extended carbon network. This characteristic leads to enhanced energy separation of the CB (VB) and CB+1 (VB-1) band edges, but because sulfur and carbon electronegativities are similar, the energy alignments of $N = 13$ AGNR bands remain relatively unchanged by sulfur doping.

4.3 Conclusion and Outlook

In conclusion, we were able to study how the dopant atoms tunes the electronic property of GNRs. In the case of boron doped N=7 AGNRs, the GNRs were doped with boron atoms along the backbone. And we observed the introduction of new dopant states inside the bandgap of the pristine GNR. On the other hand, for sulfur-doped N=13 GNRs, the sulfur atoms substitutionally doped the edges of the GNRs. Rather than significantly changing the band-gap, the electronegative S atoms increases the energy separation between CB and CB+1 as well as between the VB and VB-1. Such site-specific substitutional doping of GNRs with B and S heteroatoms will help pave the way toward the development of advanced functional device architectures based on GNR semiconductor technology.

Chapter 5-Two-Dimensional Covalent Organic Frameworks

This chapter discusses my work on covalent organic frameworks. Covalent organic frameworks (COFs) are crystalline organic structures made up of light elements and held together by strong covalent bonds. The researchers who contributed to these studies are Trinity Joshi, Dr. Chen Chen, Zahra Pedramrazi, Dr. Gaoqiang Wang, Dr. Huifang Li, Dr. Pei-Nian Liu, Anton D. Chavez, Dr. Christian S. Diercks, Peter J. Waller, Dr. Omar M. Yaghi, Dr. William R. Dichtel, Dr. Hong Li, Dr. Jean-Luc Bredas, and Dr. Michael F. Crommie.

The main objective of our study on single-layer 2D COFs was to understand its local electronic properties through atomically-precise spectroscopy. Two fundamental questions we addressed are how does the electronic behavior of a molecule change once it is linked up via covalent bonds and how does the chemical bonding environment within the covalent network affect the overall electronic properties of COFs? Our study answers these two important questions via the bottom-up synthesis and electronic structure characterization of two different porphyrin-based imine-coupled square lattice single-layer 2D COFs that exhibit symmetric (COF-366-OMe) and asymmetric (COF-420) bonding environments.

5.1 Symmetric imine-coupled square lattice COF (COF366-OMe)

In this section, I present a project focused on the changes in electronic behavior experienced by a molecule once it has been linked up via covalent bonds in a COF. The work described in this section was originally published in ref. [56].

5.1.1 Introduction

Since the first successful synthesis of COF-1 from boronic acid precursors [4], numerous COFs with different chemical linkages [29, 40–42, 108], geometries [37, 44, 45], and pore sizes [43] have been reported, showing properties of interest for applications such as gas storage [109, 110], catalysis [111–113], and photodetectors [114, 115]. Such ultrathin COFs have been synthesized in solution [44, 46, 47], at air/water interfaces [116, 117], and on surfaces [48–52]. Although there has been rapid progress in synthesizing many different COFs, characterization of their local electronic properties has progressed at a slower rate. A limited number of COFs displaying honeycomb symmetry have been examined using scanning tunneling spectroscopy techniques, revealing different aspects of their frontier orbital electronic structure [53, 54]. COFs

Chapter 5-Two-Dimensional Covalent Organic Frameworks

exhibiting square lattice symmetry have also been synthesized (*e.g.* porphyrin or phthalocyanine-containing COFs) [44, 118–121], but their local electronic structure has not yet been characterized.

In this section, I will present a combined STM and theoretical study of the local electronic structure of a single-layer porphyrin-containing COF at the surface of a Au(111) crystal. The Schiff-base condensation of 5,10,15,20-tetrakis (4-aminophenyl) porphyrin core molecules (TAPP) with 2,5-dimethoxybenzene-1,4-dicarboxaldehyde linker molecules (DMA) results in a 2D COF with a square lattice. The COF conduction and valence band states were measured by scanning tunneling spectroscopy (STS) and compared to the highest occupied molecular orbital (HOMO) and the lowest unoccupied molecular orbital (LUMO) of an isolated TAPP molecule. While the COF energy gap does not change significantly compared to the HOMO-LUMO gap of isolated, non-bonded TAPP molecules on Au(111), an energy downshift of 0.4 eV is observed for the COF band edges compared to isolated TAPP orbital energies. The valence band edge wavefunction of the COF exhibits reduced symmetry compared to the conduction band edge wavefunction, similar to behavior observed for isolated TAPP molecules. Density functional theory (DFT) calculations suggest that the observed energy downshift arises from the presence of electron-withdrawing imine linkages within the COF and that the reduced valence band symmetry arises from molecular buckling induced by interaction with the underlying Au(111) substrate. These results provide insight into how linkage-driven charge transfer causes the electronic structure of molecules to evolve as they covalently bond into networks.

5.1.2 Molecular Synthesis

5,10,15,20-Tetrakis(4-aminophenyl)-21H,23H-porphine (TAPP) was obtained from Combi-Blocks (QC-4722, 96% purity). 2,5-dimethoxybenzene-1,4-dicarboxaldehyde (DMA) linker molecules (DMA) was obtained from Sigma-Aldrich.

5.1.3 Electronic Structure of the Single Core Precursor TAPP molecule

As mentioned earlier, in order to have a deeper understanding of the change in behavior of the molecules once they are reticulated into these covalent networks, we first performed STM/STS electronic characterization of an isolated TAPP molecule on Au(111) (Figure 5.1, all STM data reported here were obtained at $T = 7\text{K}$ in ultra-high vacuum). The STM topographic image of Figure 5.1(a) shows that TAPP exhibits a four-lobe structure with a slight dip in the middle, corresponding to the core of the porphyrin. Energy-dependent LDOS obtained by dI/dV spectroscopy at the center of a TAPP molecule exhibits two peaks that are assigned to the TAPP HOMO ($-0.44 \pm 0.06\text{ V}$) and LUMO ($+1.42 \pm 0.05\text{ V}$), corresponding to a 1.85 eV transport gap (Figure 5.1(b)) (dI/dV traces obtained on different parts of the TAPP molecule exhibit different amplitudes for these peaks, but the peak energies do not vary). dI/dV mapping was performed at the HOMO and LUMO peak energies to examine the wavefunction spatial distribution for isolated

Chapter 5-Two-Dimensional Covalent Organic Frameworks

TAPP molecules (Figures 5.1(c), (d)). As seen in Figure 5.1(c), the HOMO state is nearly two-fold symmetric and exhibits an asymmetrical "dumbbell" structure in the interior. The LUMO state is more diffuse and has LDOS intensity in regions where the HOMO state is dark (Figure 5.1(d)). Similar frontier orbital LDOS patterns have been reported previously for related porphyrin molecule adsorbates on Au(111) [122].

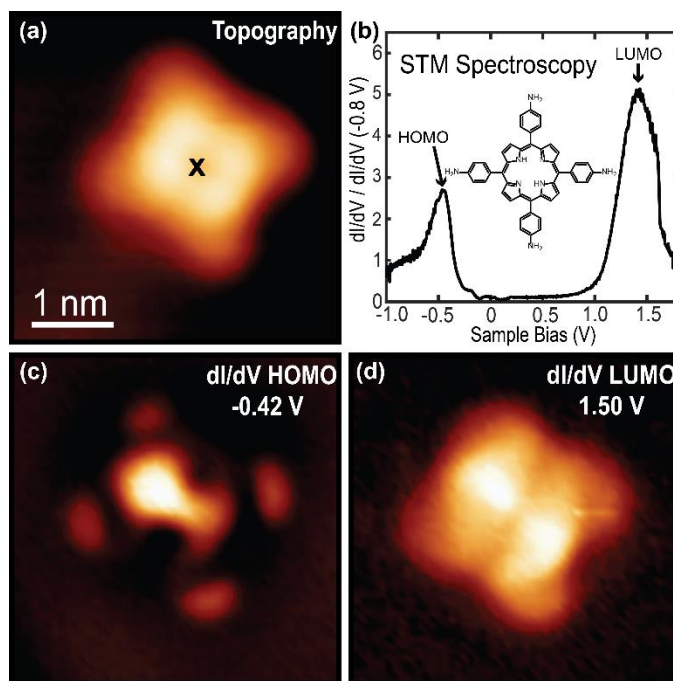


Figure 5.1 Single TAPP molecule electronic structure. (a) STM topographic image of a single TAPP molecule on a Au(111) surface (sample bias $V_s = 2.0$ V, tunneling current $I_t = 10$ pA). (The “X” represents the location where the dI/dV curve shown in (b) was obtained.) (b) dI/dV point spectra measured on top of a single TAPP molecule shows HOMO and LUMO states (open feedback parameters: $V_s = 1.0$ V, $I_t = 60$ pA; modulation voltage $V_{rms} = 10$ mV). Inset shows chemical structure of a TAPP molecule. dI/dV maps of the TAPP HOMO and LUMO states are shown for bias voltages (c) -0.42 V and (d) 1.50 V (open feedback parameters: $V_s = 1.0$ V, $I_t = 60$ pA; modulation voltage $V_{rms} = 10$ mV).

5.1.4 Synthesis of COF366-OMe on Au(111) from Precursor Molecules

This COF was synthesized by Schiff-base condensation reaction between 5,10,15,20-tetrakis(4-aminophenyl) porphyrin core molecules (TAPP) with 2,5-dimethoxybenzene-1,4-dicarboxaldehyde linker molecules (DMA). A gold crystal with a polished Au(111) surface was used as the substrate for these experiments. Standard Ar⁺ sputtering/annealing cycles were applied to obtain an atomically clean surface. Precursor molecules were thermally evaporated onto the Au(111) surface held at room temperature in an ultra-high vacuum environment (base pressure $\sim 2 \times 10^{-10}$ Torr) using a home-built Knudsen-type dual-cell evaporator. The temperature of the evaporator was ~ 110 °C for the DMA precursor and ~ 320 °C for the TAPP precursor.

As shown in Figure 5.2(a), DMA molecules were first deposited onto a Au(111) surface with a coverage of 0.9 monolayer (ML), resulting in close-packed islands with an intermolecular spacing of 0.8 nm. TAPP molecules were then deposited onto this surface, resulting in an intermixed adlayer (DMA + TAPP) as shown in Figure 5.2(b). The TAPP/DMA intermixed adlayer was then annealed at 150 °C for 1 h in UHV to induce COF formation. The sample was then cooled down and placed into a home-built cryogenic STM to perform imaging and spectroscopy at $T = 7$ K. The resultant COF covers the Au(111) surface in square-lattice patches (Figure 5.2(c)) with a unit cell size of 2.5 ± 0.1 nm, in good agreement with the expected porphyrin core-to-core distance (2.57 nm) for the COF structure shown in Figure 5.2(d). The observed structure is also in agreement with room temperature ambient STM images of this COF obtained previously from samples grown on graphite *via* solution-phase processing [123]. The zoomed-in STM image shown in Figure 5.2(a) shows additional detail that confirms the formation of the COF, which we refer to as COF366-OMe following the naming convention used in the report of its solvothermal synthesis [119]. The positions of each DMA group can be inferred from the orientation of the oval-shaped linkages positioned between porphyrin centers in the zoomed-in image of Figure 5.3(a). We named this COF as the symmetric COF due to the symmetrical configuration of the linkage (Figure 5.2(d)), each 5,10,15,20-tetraphenyl porphyrin core in COF366-OMe experiences identical chemical environment when compared with its four nearest neighbor porphyrin cores. This is because the nitrogen atom of the imine linkage is the first atom encountered as one moves outward from any porphyrin core within the COF.

Chapter 5-Two-Dimensional Covalent Organic Frameworks

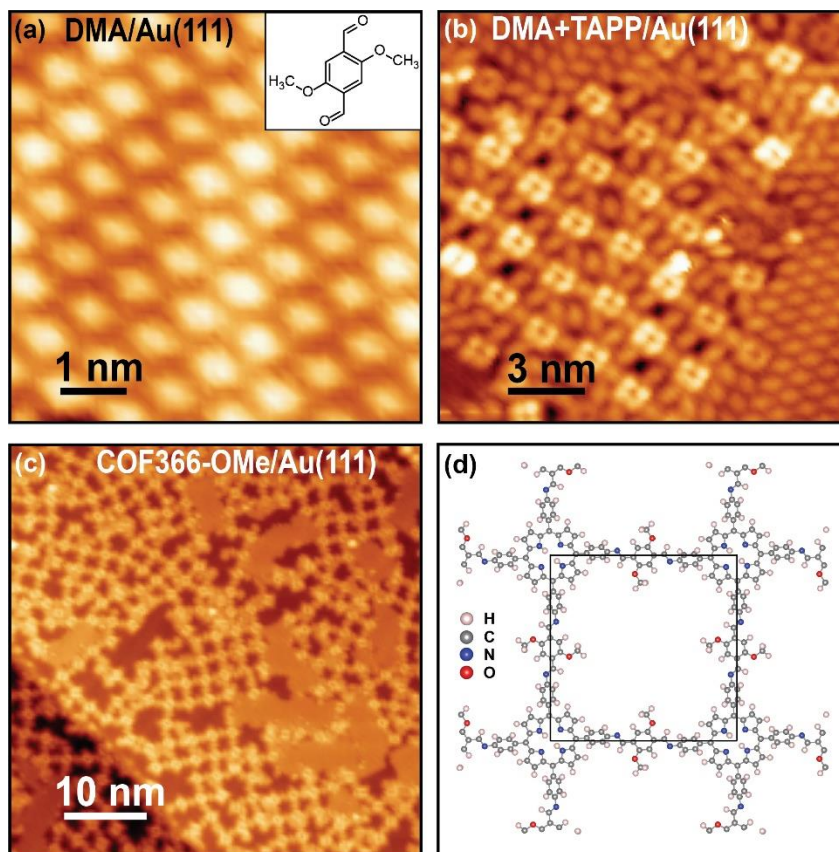


Figure 5.2 Synthesis of COF366-OMe on a Au(111) surface. (a) STM topographic image of DMA molecules deposited on Au(111) surface ($V_s = 0.8$ V, $I_t = 10$ pA). Inset shows the structure of a DMA molecule. (b) STM topographic image shows a mixture of TAPP and DMA molecules on Au(111) surface before reaction ($V_s = 1.0$ V, $I_t = 10$ pA). (c) Large-scale STM image of COF366-OMe on Au(111) after reaction of TAPP and DMA molecules ($V_s = 2.0$ V, $I_t = 10$ pA). (d) Model structure of COF366-OMe. The black square shows a unit cell.

5.1.5 Local Electronic Structure of COF366-OMe

The local electronic properties of COF366-OMe were characterized by performing STS point spectroscopy at different locations on the 2D COF (Figure 5.3(b)). The black curve shows a reference spectrum taken on a bare Au(111) region; the feature near -0.5 V corresponds to the well-known Shockley surface state of Au(111). When the TAPP core of the COF was probed (at the position of the blue X in Figure 5.3(a)), two prominent peaks are seen at -0.9 V and $+1.0$ V (blue curve). In contrast, the spectrum of the DMA linker shows only a small peak at $+1.0$ V (red

Chapter 5-Two-Dimensional Covalent Organic Frameworks

curve), suggesting that this feature arises from delocalization of the state into the linker. We assign the peak at -0.9 V as the COF366-OMe valence band maximum and the peak at $+1.0$ V as the conduction band minimum, thus leading to a band gap of 1.98 ± 0.04 eV for COF366-OMe (the uncertainty is the standard deviation of measurements obtained from 10 different cores, each connected to four nearest neighbors). Because the COF electronic structure is relatively localized, we refer to the COF valence band maximum as the highest occupied molecular orbital (HOMO) and the COF conduction band minimum as the lowest unoccupied molecular orbital (LUMO).

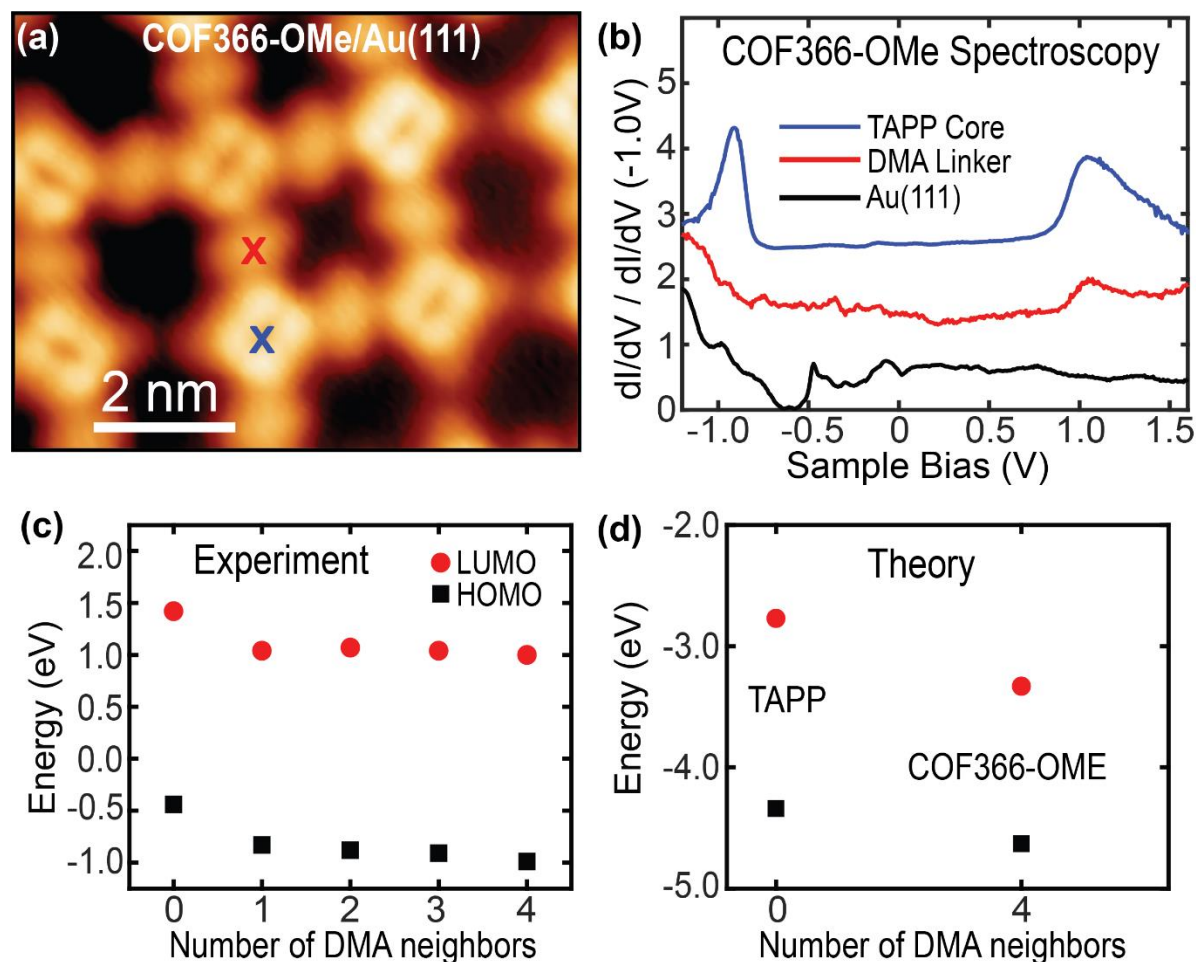


Figure 5.3 STS measurements of COF366-OMe on Au(111) surface. (a) Zoomed-in STM image of COF366-OMe ($V_s = 1.0$ V, $I_t = 10$ pA). Red and blue crosses indicate the positions at which dI/dV spectra were taken. (b) dI/dV spectra taken at location of DMA linker (red curve) and

Chapter 5-Two-Dimensional Covalent Organic Frameworks

TAPP core (blue curve) shown in (a), as well as bare Au(111) surface for reference (black curve). Each curve is normalized by the value at $V_s = -1.0$ V, and the red (blue) curve is upshifted by 1 (2.5) a.u. for clarity (open feedback parameters: $V_s = 1.0$ V, $I_t = 40$ pA, 60 pA, 80 pA for the red, black and blue curve respectively; modulation voltage $V_{rms} = 10$ mV). (c) Effect of number of DMA neighbors on the HOMO and LUMO energies of a porphyrin core (0 DMA neighbors refers to an isolated TAPP molecule). Each data point consists of at least eight different measurements, and the error bars are smaller than the size of the dots. (d) DFT calculations of the electronic structure of freestanding, isolated TAPP molecule and COF366-OMe, indicating a downshift in HOMO and LUMO energies upon COF formation (zero energy is the vacuum level).

A closer inspection of the extended structure in Figure 5.3(a) reveals that some of the linkers are missing, resulting in TAPP cores that are covalently bonded to only two or three DMA linkers instead of the four found in the ideal COF structure. To understand the effect of this type of defect, we took dI/dV point spectra on TAPP cores connected to different numbers of DMA linkers. The average HOMO and LUMO energies for TAPP cores connected to different numbers of linkers are plotted in Figure 5.3(c). The HOMO-LUMO gap measured at the site of a TAPP core does not change significantly with the number of linkers bonded to it. However, a large energy downshift in the HOMO/LUMO states (0.4 eV) is seen as soon as even a single DMA linker is bound. Subsequent bound linkers do not significantly change the energy shift, although a slight downward trend in the HOMO energies is seen. Spectroscopic surveys performed in different COF regions and on different parts of the porphyrin cores yield no significant deviations from these findings.

Chapter 5-Two-Dimensional Covalent Organic Frameworks

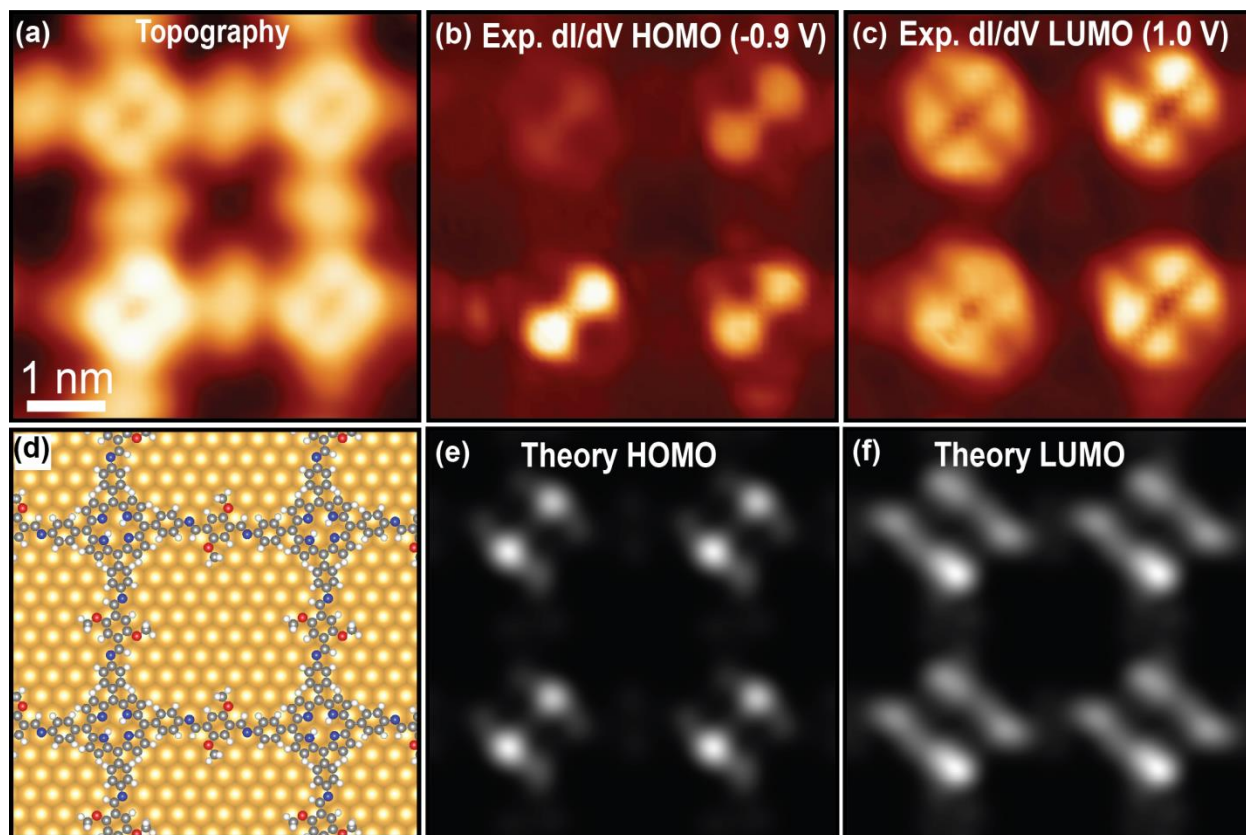


Figure 5.4 Spatial distribution of COF366-OMe electronic states. (a) STM topographic image shows zoom-in view of COF366-OMe ($V_s = 1.0$ V, $I_t = 60$ pA). Experimental dI/dV maps for (b) the COF HOMO at -0.90 V and (c) the COF LUMO at +1.00 V (open feedback parameters: $V_s = -0.90$ V for HOMO and +1.00 V for LUMO, $I_t = 60$ pA; modulation voltage $V_{rms} = 10$ mV). (d) DFT-optimized adsorption geometry of COF366-OMe on Au(111) surface. Simulated LDOS maps of COF366-OMe on Au(111) for (e) HOMO state and (f) LUMO state.

The spatial wavefunction distribution of the COF366-OMe HOMO and LUMO states was measured by dI/dV mapping conducted at their corresponding peak energies. Figure 5.4(a) shows an STM topographic image of the COF segment on which dI/dV mapping was performed. As shown in Figures 5.4(b) and 5.4(c), experimental HOMO and LUMO dI/dV maps both have significantly higher intensity on the TAPP cores than on the DMA linkers. The COF LUMO state exhibits a four-lobe structure with two nodal lines while the HOMO state exhibits a smaller “dumbbell” shape with bright intensity near the LUMO nodal region. There is some resemblance between the COF HOMO/LUMO states and the isolated TAPP precursor molecule HOMO/LUMO states (Figure 5.1), but the COF states are more symmetric. We note that the “dumbbells” of the COF HOMO can be misaligned between adjacent porphyrin cores.

Chapter 5-Two-Dimensional Covalent Organic Frameworks

5.1.6 DFT Calculations and Comparison to Experimental Results

We first performed a series of DFT-PBE calculations aimed at understanding the origin of the electronic structure observed in our experiments (theory performed by the J. -L. Bredas group). The initial calculations focused on isolated TAPP molecules (*i.e.*, core molecules with zero DMA linkers) as well as the full, periodic COF366-OMe network (*i.e.*, core molecules with four DMA linkers) in the absence of substrate effects (*i.e.*, the “freestanding” limit). After optimization both systems contained a planar central porphine macrocycle with the four phenyl rings twisted with dihedral angles ranging from 60° to 67° with respect to the central plane. The energies of the HOMO and LUMO states for the isolated TAPP molecule and the COF366-OMe network are plotted in Figure 5.3(d) where zero energy represents the vacuum level. The formation of COF366-OMe results in a LUMO downshift of 0.57 eV and a HOMO downshift of 0.29 eV compared to the isolated TAPP molecule. Formation of the COF thus leads to an energy downshift similar to what is seen experimentally, but the calculation also shows an energy gap reduction. This reduction is not observed in the experiment owing to the interactions of the TAPP and COF monolayers with the Au(111) surface (*vide infra*).

Although these calculations were performed at the standard DFT-PBE level, which tends to underestimate absolute HOMO-LUMO gaps, the observed relative energy level shifts due to covalent bonding to the DMA linkers are consistent with our STS measurements. This energy-level downshift is explained by the fact that the amine ($-\text{NH}_2$) group of the isolated TAPP molecule is relatively electron-rich (*i.e.*, electron-donating) whereas the imine ($-\text{C}=\text{N}-$) group of the COF is more electron-poor (*i.e.*, electron-withdrawing). As a result, the transition from amine to imine due to the condensation reaction decreases electron density within the porphyrin core, thereby electrostatically shifting the frontier orbital energies downwards. This was further confirmed by the results of calculations on the electronic structure of a TAPP molecule bonded to a single DMA linker using a localized (atomic) basis set (with the Gaussian 09 package). Once again a clear downshift is observed in the frontier orbitals of the combined TAPP+DMA system compared to isolated TAPP molecules.

To better understand the spatial wavefunction properties of these molecular systems, we extended the DFT calculations for both individual TAPP molecules and COF366-OMe networks to include contact with a Au(111) substrate. These calculations show that the interaction between an isolated TAPP molecule and the underlying Au(111) substrate leads to a “saddle-like” structure, where the four pyrrole rings in the porphine macrocycle tilt alternately up and down so as to maximize the nitrogen-gold interactions (the equilibrium geometry has all four porphine nitrogens nearly on top of four Au atoms in the top layer of the Au(111) surface). This is in agreement with earlier results on other porphyrin derivatives [124–126]. After COF formation on the Au(111) surface, the porphine macrocycles are observed to retain the saddle structure. This distortion of the porphyrin core leads to a much stronger charge localization on the β - β C-C bond of the two up-tilted pyrrole rings compared to the β - β C-C bond of the two down-tilted pyrroles, resulting in the

Chapter 5-*Two-Dimensional Covalent Organic Frameworks*

dumbbell shape of the COF HOMO state (Figure 5.4(e)). In contrast, the calculated LDOS of the LUMO state (Figure 5.4(f)) displays a nearly four-fold symmetric distribution on the TAPP core, in reasonable agreement with the four-lobe structure observed in the COF dI/dV map (Figure 5.4(c)) (some discrepancy does exist between theoretical and experimental maps, likely due to differences in tip trajectory since the experimental dI/dV maps were taken along a surface of constant-current feedback while the theoretical simulation shows LDOS intensity taken along a plane at fixed distance above the COF). Inclusion of the substrate in our calculations also results in the HOMO-LUMO gap remaining constant for isolated TAPP molecules compared to a fully formed COF, thus explaining why we do not experimentally observe the gap reduction predicted by the “freestanding” calculations.

We note that although the core dominates both the experimental and theoretical LUMO LDOS images shown in Figure 5.4, some LUMO state density does still extend across the DMA linker. The reason the core dominates the LUMO maps of Figure 5.4 is because the STM tip is relatively far from the surface ($\sim 4 \text{ \AA}$) and the core LDOS is much greater than the linker LDOS at this distance. This is partly due to the fact that the phenyl rings of the core twist away from the Au surface by 35° (leading to the four brightest spots in the simulated LUMO dI/dV map) whereas the DMA linkers lie flat.

5.1.7 Summary

In conclusion, we have characterized the local electronic structure of a single-layer porphyrin-containing square-lattice COF on Au(111). Energy shifts of the frontier orbitals of the porphyrin core are observed upon COF formation due to the electron withdrawing nature of the imine linkages. The experimentally measured HOMO and LUMO wavefunctions of the COF have highest intensity on the porphyrin cores and exhibit an energy gap of $1.98 \pm 0.04 \text{ eV}$. DFT-based electronic local density of states simulations are consistent with our experimental data and confirm that substrate-induced buckling observed for isolated porphyrins persists in COF networks. This provides insight into how the electronic structure of molecular nanostructures is affected by forming covalent bonds between monomer components.

5.2 Asymmetric imine-coupled square lattice COF (COF-420)

In this section, I present a project focused on the effect of chemical bonding environment on the electronic behavior of a COF. The work described in this section was originally published in ref. [57].

Chapter 5-Two-Dimensional Covalent Organic Frameworks

5.2.1 Introduction

Different electronic and chemical properties can be engineered into COF networks by modifying the molecular properties of the building-blocks [114, 127–129]. Two-component COFs provide a high degree of electronic tunability since one molecular element can act as a ‘core’ while the second acts as a ‘linker’ between cores, and both can be precisely modified [130, 131]. This approach, for example, has been used to create donor-acceptor COFs that are made by fusing donor/acceptor molecules into core/linker arrangements that yield ordered arrays of molecular charge-transfer pairs, with potential applications in optoelectronics and catalysis [132–134]. Such electrically modulated COFs, however, have up to now been fabricated using techniques that do not allow synthesis of a single-layer structure, and no local probe measurements have been performed to verify the effects of local charge-transfer.

In this section, I will present our study demonstrating new technique for fabricating COFs that exhibit internal electronic heterojunctions with staggered potential offsets. The core of the COF is tuned independently from charge-transfer elements that reside within the linker. This is accomplished through directed Schiff-base condensation reactions that allow oriented dipoles to be placed between core elements in an alternating arrangement, thus causing adjacent cores to experience a relative potential offset. The surface compatibility of this chemistry allows bottom-up fabrication of single-layer COF-420 whose local electronic structure we have characterized at the atomic scale using scanned probe microscopy.

The new COF was fabricated by first synthesizing two square planar tetrapodal building blocks (5,10,15,20-tetrakis(4-aminophenyl)porphyrin (TAPP) and 5,10,15,20-tetrakis(4-formylphenyl)porphyrin (TFPP)) as shown in Figure 5.6 (synthesis performed by the O. M. Yaghi group). Upon reticulation at a surface these precursors yield cores that have identical chemical composition but are rendered electrically asymmetric by the relative orientation of the imine linkages connecting them. Charge-transfer functionality thus resides in the linker and is separated from the core electronic properties. This unique asymmetric COF is termed COF-420 ((TAPP)(TFPP)imine) and exhibits a square lattice (**sql**) topology. Due to the asymmetrical configuration of the linkage (Figure 5.6(a)), each 5,10,15,20-tetraphenyl porphyrin core in COF-420 experiences a different chemical environment than its four nearest neighbor porphyrin cores. For example, if we denote cores arising from TAPP as ‘core A’ and cores arising from TFPP as ‘core B’, then the nitrogen atom of the imine linkage is the first atom encountered as one moves outward from core A, whereas for core B the first atom encountered is carbon. Scanning tunneling microscopy (STM) was used to experimentally verify that this asymmetrical bonding scheme results in the spatial separation of the conduction band (CB) and the valence band (VB) onto different porphyrin cores (i.e., different sublattices), thus forming a grid of molecular type II heterojunctions within COF-420. Hirshfeld charge analysis performed using density functional theory (DFT) suggests that these molecular heterojunctions arise from dipole fields generated within the imine linkages of the COF.

5.2.2 Molecular Synthesis

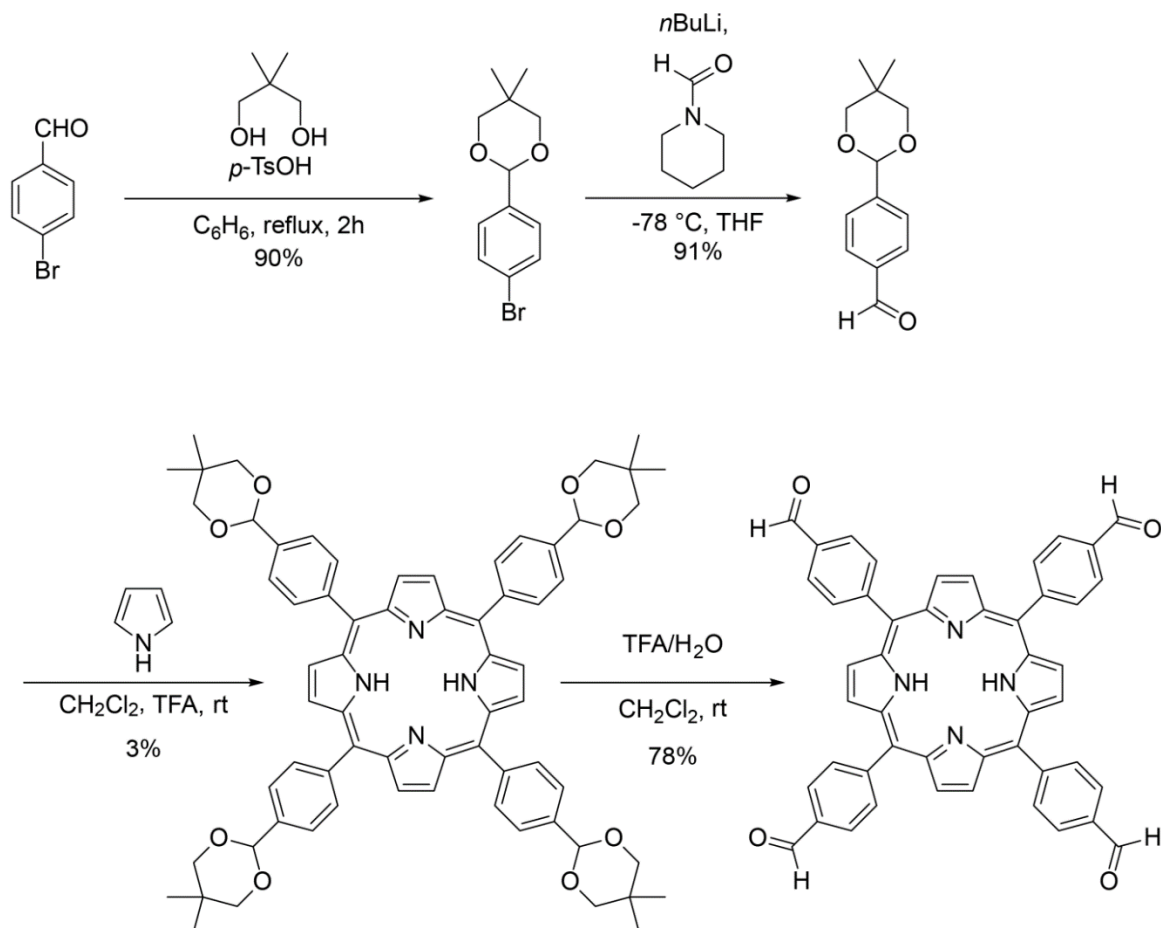


Figure 5.5 Synthesis of meso-tetra(*p*-formylphenyl)porphyrin.

The synthesis of TFPP was carried out according to a literature protocol [135]. In a first step 4-bromobenzaldehyde was protected using neopentyl glycol to yield 2-(4-bromophenyl)-5,5-dimethyl-1,3-dioxane (90%). In a second step, lithiation at $-78\text{ }^\circ\text{C}$ followed by formylation with 1-formyl piperidine yielded 4-(5,5-dimethyl-1,3-dioxan-2-yl)benzaldehyde (91%). In a third step

Chapter 5-Two-Dimensional Covalent Organic Frameworks

reaction with pyrrole catalyzed by trifluoroacetic acid yielded tetrakis[4-(1,3-dioxo-5,5-dimethylcyclohex-2-yl)phenyl]porphyrin (3%). Finally, deprotection of the 5,5-dimethyl-1,3-dioxane protecting groups yielded meso-Tetra(*p*-formylphenyl)porphyrin which was purified by column chromatography (dichloromethane) and isolated as a dark violet solid (78%) (Figure 5.5).

5,10,15,20-Tetrakis(4-aminophenyl)-21H,23H-porphine was obtained from Combi-Blocks (QC-4722, 96% purity).

5.2.3 Synthesis of COF-420 on Au(111) from Precursor Molecules

The synthesis of single-layer COF-420 was carried out on a Au(111) surface in ultrahigh vacuum (UHV). Standard Ar⁺ sputtering/annealing cycles were applied to a polished Au(111) crystal to yield an atomically clean surface. Molecular precursors for COF-420 were deposited onto the clean Au(111) surface held at room temperature in an ultrahigh vacuum environment (base pressure $\sim 2 \times 10^{-10}$ Torr) using a home-built Knudsen-type dual-cell evaporator. The temperature of evaporator for TAPP and TFPP precursors were 330°C and 340°C respectively. TFPP molecules were first deposited onto the surface via thermal evaporation, followed by deposition of TAPP molecules. The adsorbed precursors were then gradually annealed to 180 °C and held at that temperature for 45 minutes to induce the condensation reaction that results in imine bond formation (Figure 5.6(a)).

The sample was then cooled down and placed into a home-built cryogenic STM to perform imaging and spectroscopy at $T = 7\text{K}$. Figure 5.6(b) shows an STM topographic image of the resulting single-layer COF-420. Square lattice patches are observed that exhibit a ‘checker board’ pattern, indicating an alternating array of two electrically distinct porphyrin cores (a small fraction of cores near the edge of the COF do not exhibit the checkerboard pattern, possibly due to metalation of core B) [6]. The unit cell determined via STM imaging has equal sides of length $a = b = 27 \pm 1.6 \text{ \AA}$. Figure 5.6(c) shows a zoomed-in image of COF-420, with a superimposed line drawing of the chemical structure in the top right corner.

Chapter 5-Two-Dimensional Covalent Organic Frameworks

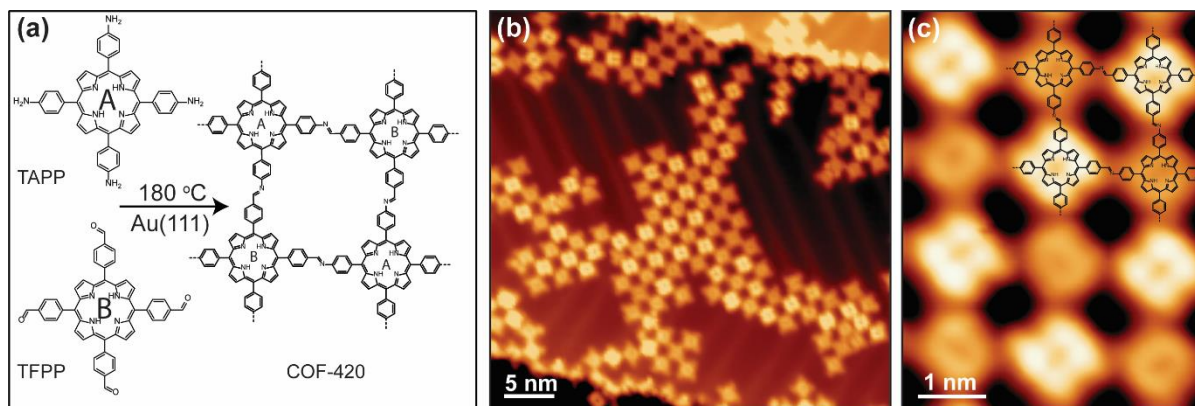


Figure 5.6 Bottom-up fabrication of COF-420. (a) Schematic representation of the synthesis of COF-420 from molecular precursors TAPP and TFPP. (b) Representative large-scale STM topographic image of COF-420 on Au(111) (sample bias $V_s = 0.8$ V, tunnel current $I_t = 10$ pA). (c) Close-up STM image of COF-420 with the chemical structure overlaid in top-right corner ($V_s = 0.8$ V, $I_t = 10$ pA).

Core A (originating from TAPP) and core B (originating from TFPP) are structurally identical upon reticulation and differ only in their local chemical environment due to the imine linkage. Although we saw a checkerboard pattern for COF-420 in STM topographic scans, careful consideration was made in order to assign darker (brighter) cores to core A (core B). We chose to structurally identify these cores by co-depositing a small amount of 2,5-dimethoxybenzene-1,4-dicarboxaldehyde linker molecules (DMA) onto the same surface (Figure 5.7(a)). After annealing we expect only core A (from TAPP) to undergo a Schiff-base condensation reaction with the DMA, thus forming a covalent bond with it (Figure 5.7(a)) [56]. To accomplish this, TAPP, TFPP and DMA were co-deposited onto a Au(111) surface and the sample was annealed to $\sim 150^\circ\text{C}$ to induce the Schiff-base condensation reaction. Figure 5.7(b) shows an STM topographic image of a sample prepared in this way. As shown in the blue box in the figure, the porphyrin cores with lower intensity were the ones that covalently bonded with DMA linkers. We thus assign the porphyrin core with the lower intensity as core A (originating from TAPP) and the porphyrin core with the higher intensity as core B (originating from TFPP).

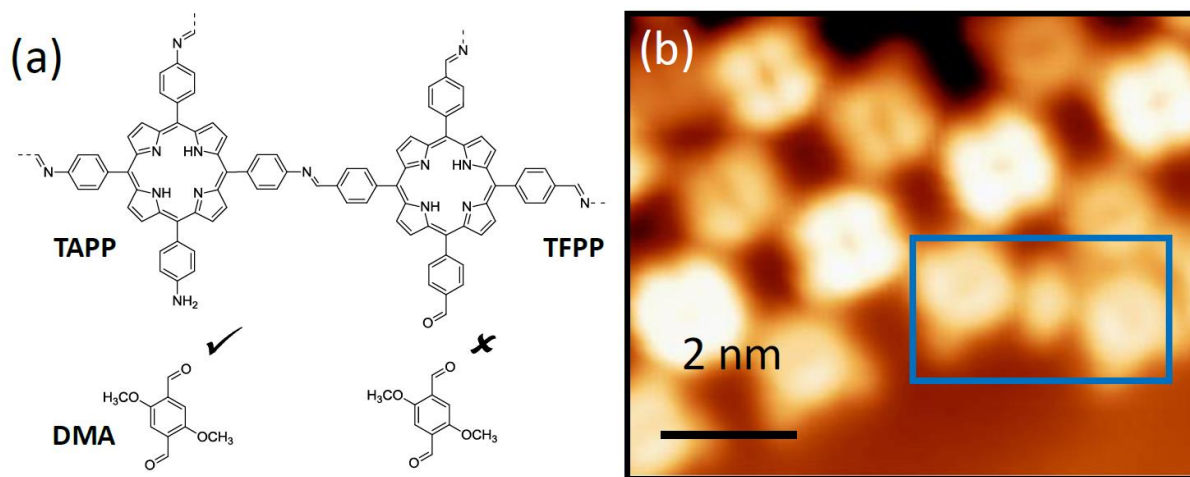


Figure 5.7 Justification of the assignment of the core A (from TAPP) and core B (from TFPP). (a) Sketch of COF-420 in the presence of DMA linker. DMA can undergo a condensation reaction only with core A. (b) STM topograph of a Au(111) surface obtained by annealing adsorbed TAPP, TFPP and DMA molecules (sample bias $V_s = 0.8$ V, tunneling current $I_t = 10$ pA). The blue box shows that only porphyrin cores with lower intensity form covalent bonds with the DMA linker, thus justifying the identification of these porphyrin cores as core A (originating from TAPP).

5.2.4 Local Electronic Structure of COF-420

The local electronic structure of COF-420 was characterized by STM dI/dV point spectroscopy performed at different positions on the single-layer COF as shown in Figure 5.8 (point spectroscopy positions are shown in Figure 5.8(a)). The black curve in Figure 5.8(b) shows a reference spectrum taken at a nearby bare Au(111) region (the sharp drop at -0.5 V corresponds to a Shockley surface state band edge [104]). The blue curve shows a typical dI/dV point spectrum recorded on core A within the COF, whereas the red curve shows a typical dI/dV point spectrum recorded on the neighboring core B. Both cores exhibit two well-defined resonances that arise from bands composed of porphyrin molecular orbitals. The bands localized on core A, however, are shifted up in energy by ~ 0.25 eV relative to the bands whose weight lies on core B (i.e., the bands are localized on different sublattices). This causes the valence band (VB) to lie on core A while the conduction band (CB) lies on core B. Similarly, the outlying VB-1 and CB+1 bands are located on core B and core A respectively. The resulting experimental bandgap for COF-420 is 1.92 ± 0.06 eV (i.e., the difference in energy between the CB and VB peaks).

Chapter 5-Two-Dimensional Covalent Organic Frameworks

The spatial localization of the COF-420 bands onto different sublattices is better seen in the dI/dV maps of Figure 5.8(c)-(f), obtained at the different peak energies in the same COF region as imaged in Figure 5.8(a). Figure 5.8(c) shows the dI/dV map obtained at the CB energy, where the local density of states (LDOS) lights up (i.e., has highest intensity) on core B sites. The CB LDOS pattern at each core exhibits a nearly 4-fold symmetric structure with two orthogonal nodal lines crossing through the center of the porphyrin core. The LDOS intensity at the VB energy is shown in Figure 5.8(d), and is found to be shifted from core B sites to core A sites. The VB LDOS symmetry is also quite different than the CB LDOS in that it is ‘dumbbell’ shaped and 2-fold symmetric rather than 4-fold symmetric. The difference between the VB and CB LDOS shapes reflects the difference in symmetry between the highest occupied molecular orbital (HOMO) and the lowest unoccupied molecular orbital (LUMO) for isolated porphyrin molecules and their derivatives [56, 124–126]. Unlike the CB states seen on the core B sublattice, some of the core A sites do not show LDOS intensity at the VB energy. This is caused by small, spatially inhomogeneous shifts in the energy of the VB peak, likely due to surface defects and conformational changes within the COF (including the number of complete nearest neighbor bonds). The VB peak has the narrowest width and so slight shifts in energy for molecules on the core A sublattice causes dramatic reductions in VB intensity in constant bias dI/dV maps. Figure 5.8(e)-(f) show that the CB+1 and VB-1 LDOS also reside separately at core A and core B sites, respectively, thus separating onto different sublattices just as seen for the VB and CB states. The COF-420 spectroscopy shows all of the hallmarks of type II heterojunctions, including a staggered band structure and spatial localization of VB and CB states at different physical locations. Unlike a conventional type II heterojunction which has only a single interface, COF-420 exhibits a periodic array of heterojunctions that exist between each adjacent molecular core.

Chapter 5-Two-Dimensional Covalent Organic Frameworks

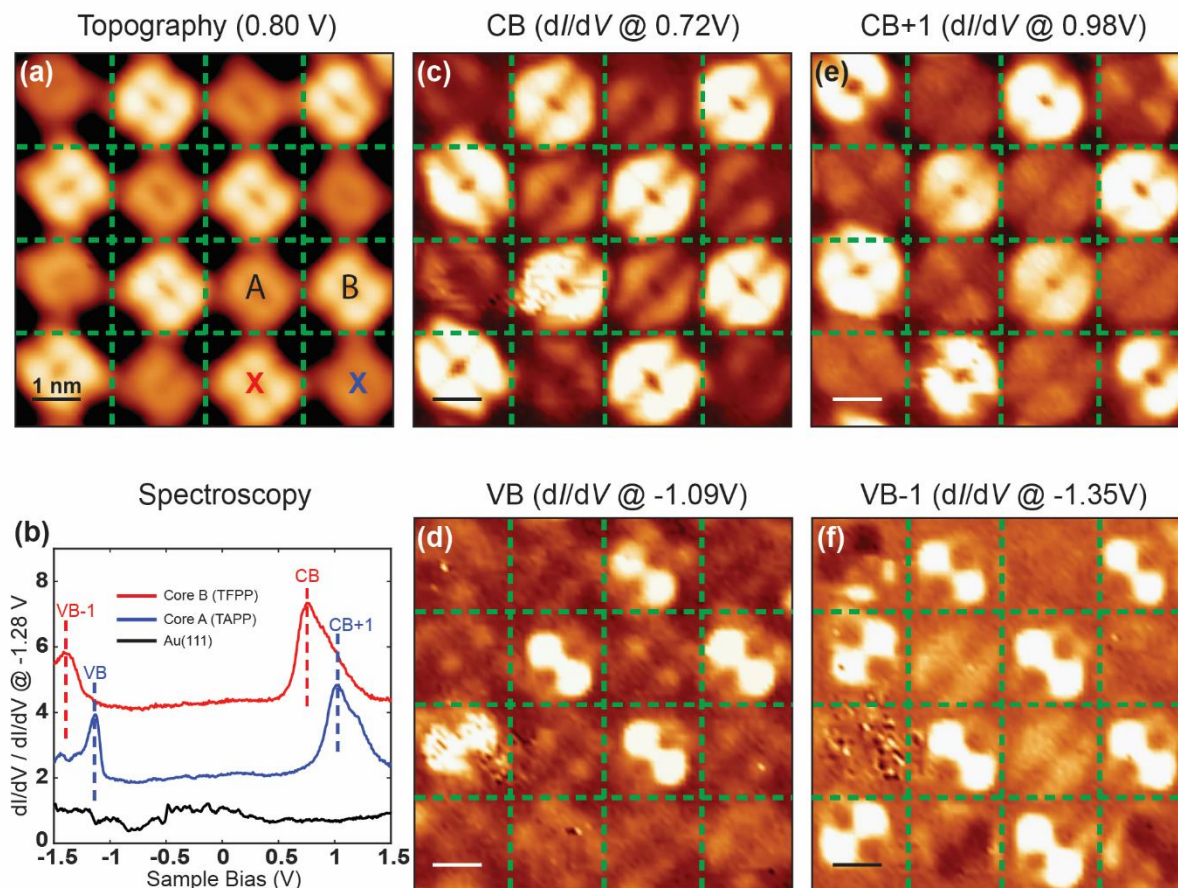


Figure 5.8 Electronic structure of COF-420. (a) Close-up STM image of COF-420 ($V_s = 0.8$ V, $I_t = 10$ pA). Red and blue x's indicate the positions where dI/dV spectra were recorded. (b) dI/dV spectra taken at location of core B (red curve) and core A (blue curve) shown in panel (a), as well as spectrum from bare Au(111) surface for reference (black curve). Each curve is normalized by the value at $V_s = -1.28$ V and the red (blue) curve is upshifted by 4 (1.75) for clarity (open feedback set point parameters: $V_s = 0.8$ V, $I_t = 20$ pA for all the curves; modulation voltage $V_{rms} = 51$ mV). Experimental dI/dV maps for (c) the COF CB at 0.72V, (d) the COF VB at -1.09V, (e) the COF CB+1 at 0.98V and (f) the COF VB-1 at -1.35V (dI/dV map parameters: $I_t = 20$ pA; modulation voltage $V_{rms} = 51$ mV).

5.2.5 DFT Calculations and Comparison to Experimental Results

In order to identify the underlying cause of the staggered band structure and wavefunction localization observed in our experiments, we performed first-principles calculations of COF-420 using density functional theory (DFT) at the generalized gradient approximation (GGA) level

Chapter 5-Two-Dimensional Covalent Organic Frameworks

(theory performed by the J. -L. Bredas group). These efforts were aimed at answering three fundamental questions. The first question is simply whether DFT-based simulations are able to reproduce the experimental phenomena observed in order to confirm that it is consistent with the physical system we believe to be measuring. The second is whether this behavior is intrinsic to the COF, or rather a byproduct of the interaction between the COF and the Au(111) substrate. The third question is what microscopic mechanism causes type II heterojunction behavior to arise between the sublattices of COF-420.

We addressed the first question by modeling the behavior of COF-420 on Au(111) using the unit cell sketched in Figure 5.9(a). The STM dI/dV spectra were simulated by separately calculating the projected density of states of this system onto core A and core B, as shown in Figure 5.9(b). The core A sublattice (blue curve) shows two prominent peaks corresponding to the VB and CB+1 bands whereas core B (red curve) shows two peaks shifted down in energy with respect to core A (corresponding to the VB-1 and CB bands). The resulting bandgap is 1.10 eV, approximately 0.82 eV smaller than the experimental value, which is due to the known behavior of GGA-DFT calculations to underestimate quasiparticle bandgaps [17, 136]. Other than the gap, however, the calculation reproduces the experimental results closely. For example, the VB and CB are seen to localize on different sublattice cores, precisely as seen in the experiment. Also, the energy differences between VB and VB-1 as well as between CB and CB+1 have an average magnitude of 0.31 eV, very close to the average experimental value of 0.25 eV (these differences do not suffer the known GGA-DFT tendency to underestimate bandgaps). The simulated electronic structure thus yields a robust network of molecular type II heterojunctions in agreement with the experiment.

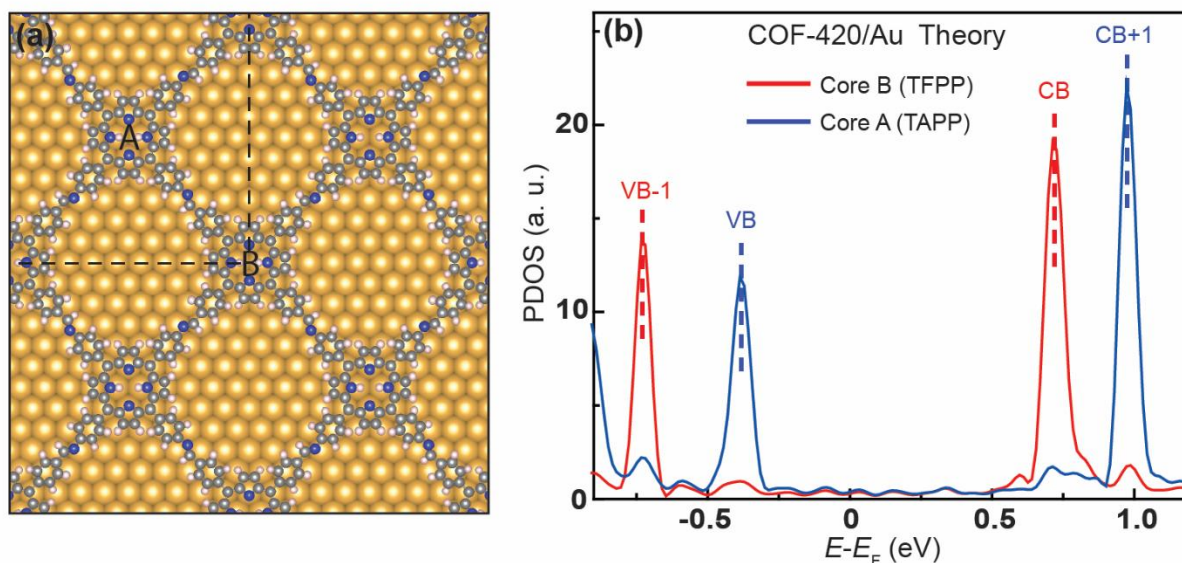


Figure 5.9 Theoretical electronic structure of COF-420 on Au(111). (a) Optimized geometry

Chapter 5-Two-Dimensional Covalent Organic Frameworks

of COF-420 on a Au(111) surface resulting from density functional theory (DFT) calculation (unit cell marked by dashed lines). (b) Theoretical projected density of states (PDOS) calculated for COF-420 on Au(111) (i.e., DOS projected separately onto the two cores). The red curve represents the PDOS of core B whereas the blue curve represents the PDOS of core A.

The behavior of freestanding COF-420 layers was also calculated in order to check that the staggered electronic structure of COF-420 is an intrinsic property and not the result of substrate interactions. The optimized structure of a free-standing COF-420 monolayer (lattice constant = 27.1 Å) calculated at the PBE-TS level under periodic boundary conditions is shown in Figure 5.10(a). The projected densities of states (PDOS) for core A (originating from TAPP) and core B (originating from TFPP) are shown in Figure 5.10(b). The behavior of freestanding COF-420 was found to be nearly identical to COF-420 on Au(111). The bandgap calculated for freestanding COF-420 is 1.38 eV (Figure 5.10(b)), slightly larger than the energy gap calculated for COF-420 on Au(111) (1.10 eV). This difference is expected to be due to the enhanced screening experienced by COF-420 when it is in contact with Au. The band offset obtained from the average energy difference of the VB and VB-1 bands as well as the CB and CB+1 bands for freestanding COF-420 is 0.31 eV, almost identical to the average band offset calculated for COF-420 on Au(111) (0.31 eV), as well as the average experimental offset (0.25 eV).

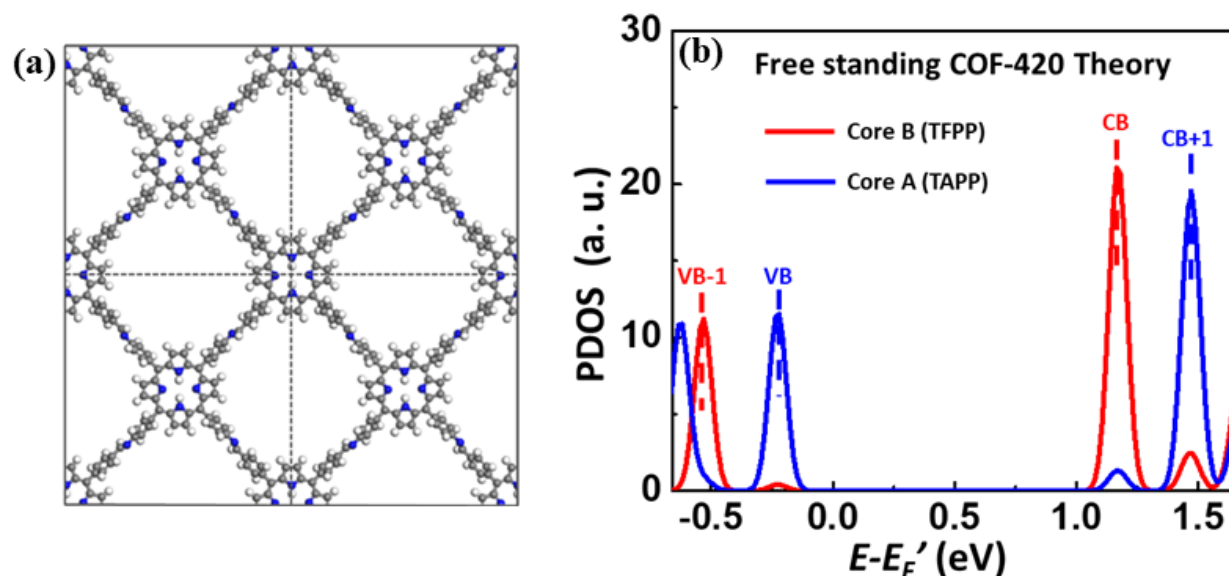


Figure 5.10 Theoretical electronic structure of free-standing COF-420 monolayer. (a) Optimized structure of free-standing COF-420 monolayer resulting from density functional theory (DFT) calculation (unit cell marked by dashed lines). (b) Theoretical projected density of states (PDOS) of a free-standing COF-420 monolayer. The red curve represents the PDOS of core B whereas the blue curve represents the PDOS of core A. Here, E_F' is $1/2(E_v + E_c)$.

Chapter 5-Two-Dimensional Covalent Organic Frameworks

Figure 5.11(a) and 5.11(b) shows the partial charge density plot for the free-standing COF-420 monolayer. It can be seen clearly that VB and CB wavefunctions of freestanding COF-420 are separately localized on core A and core B, just as observed experimentally and in the COF-420/Au(111) simulation.

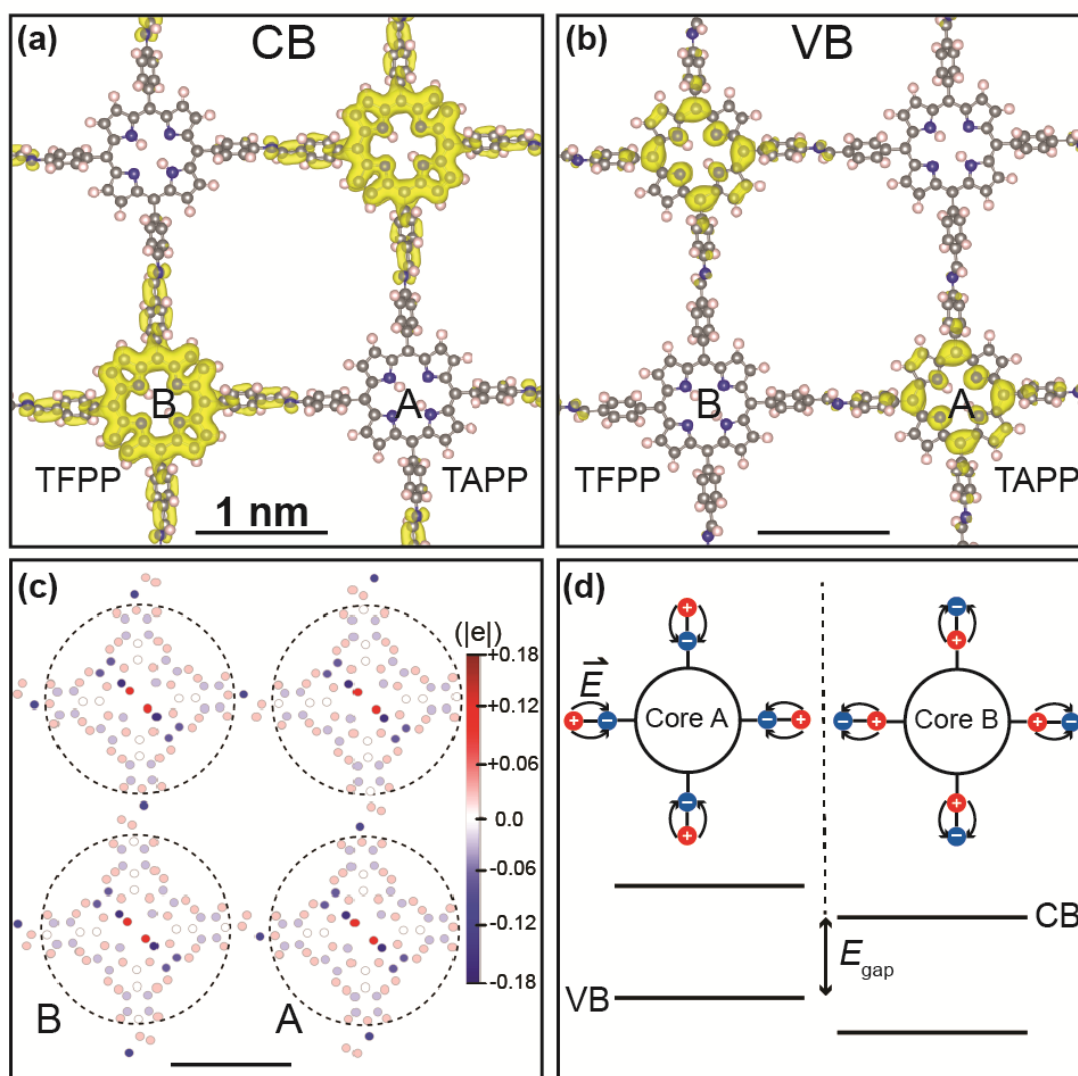


Figure 5.11 Local charge transfer leads to spatial separation of CB and VB. (a) Charge density distribution for free-standing COF-420 state at the conduction band minimum and; (b) charge density distribution at the valence band maximum. (partial charge density isosurface plotted for $8 \times 10^{-4} |e|$ (bohr) $^{-3}$). (c) Hirshfeld population plot of free-standing COF-420 showing the formation

Chapter 5-Two-Dimensional Covalent Organic Frameworks

of local dipoles generated by the net charges accumulating on nitrogen atoms (blue, $q_N = -0.128$ |e|) as well as carbon and hydrogen atoms (red, $q_{CH} = 0.075$ |e|) of the imine bonds between porphyrin macrocycles. (d) Sketch of a simple electrostatic model showing how the dipole field arising from the oriented imine bonds leads to an energy offset between core A and core B.

5.2.6 Hirshfeld Charge Transfer Analysis

To understand the microscopic mechanism driving the formation of a periodic array of type II heterojunctions in COF-420, we took a closer look at the simulated charge distribution within the COF network. This suggests that the staggered band structure originates from the dipole field generated by the oriented imine bonds linking the porphyrin cores. The charge distribution was calculated for a freestanding COF-420 single-layer using the Hirshfeld charge analysis as implemented by the Tkatchenko-Scheffler method in VASP. This technique allows evaluation of the difference in charge density that arises in the vicinity of each atom due to the formation of surrounding chemical bonds [137] and has been used to analyze other extended molecular systems [135]. A Hirshfeld population plot of the freestanding COF-420 is shown in Figure 5.11(c). While significant charge redistribution can be seen throughout the COF, the distributed net charge on core A is very similar to the distributed charge on core B (the dashed circles enclose the identical porphyrin macrocycles of core A and core B). The formation of dipoles can be seen between the porphyrin macrocycles that are generated by charge accumulation on the nitrogen atom (blue, $q_N = -0.128$ |e|) as well as the carbon and hydrogen atoms (red, $q_{CH} = 0.075$ |e|) within the imine bonds. The lower energy of core B relative to core A arises because the positive end of the imine dipole *always* points toward core B, whereas the negative end *always* points toward core A.

5.2.7 Estimation of the Dipole-Induced Inter-sublattice Electrostatic Energy Offset

To further test this idea we can perform a rough estimate of the inter-sublattice electrostatic energy offset arising from the dipole field of the oriented imine bonds using the simplified geometry of Figure 5.11(d). For an electron placed at the center of core A, the energy increase arising from the four nearest imine dipoles is

$$\Delta E_A = \frac{1}{4\pi\epsilon_0} \times \frac{4|e|p}{r^2 - d^2/4} \quad (5.1)$$

Here p is the strength of the imine dipole, d is the length of the dipole, and r is the distance from the dipole center to the core center. The strength of the imine dipole is $p = \frac{q_{CH} - q_N}{2} d$ where q_N is the charge on the nitrogen atom and q_{CH} is the charge on the CH group. From symmetry we see

Chapter 5-Two-Dimensional Covalent Organic Frameworks

that $\Delta E_B = -\Delta E_A$, and so the energy difference arising from the dipole field for an electron on core A compared to an electron on core B is $\Delta E_T = 2\Delta E_A$. If we use the values $q_N = -0.128 |e|$ and $q_{CH} = 0.075 |e|$ from the Hirshfeld analysis, $r = 9.53 \text{ \AA}$ from the molecular geometry, and $d = 1.29 \text{ \AA}$ (the length of a double bond) then we see that $\Delta E_T = 0.16 \text{ eV}$, in reasonable agreement (given the degree of approximation) with the observed experimental band offset of 0.25 eV .

5.2.8 Summary

In conclusion, we have synthesized a porphyrin-based imine-linked square-lattice single-layer COF with atomically-precise type II heterojunctions distributed throughout the entire lattice. Characterization of the COF by STM/STS measurements and *ab initio* simulations reveals that an asymmetrical chemical environment of the adjacent porphyrin cores causes localization of the CB and VB onto distinct COF sublattices. Hirshfeld charge analysis implies that the origin of the heterojunction behavior is the asymmetrical dipole field that arises from oriented imine linkages within the COF. We expect this COF to exhibit novel optoelectronic properties since exciton formation should lead to the generation of electron and hole quasiparticles localized on different COF sublattices.

5.3 Conclusion and Outlook

Thus, through the study of the COF366-OMe and the COF-420 we explored the significant role of the covalent bonds in engineering the electronic structure of the COF. In the case of COF366-OMe, we observed an energy downshift for the COF band edges compared to isolated TAPP orbital energies due to the presence of the electron-withdrawing imine linkages within the COF. On the other hand, COF-420 exhibited internal electronic heterojunctions with staggered potential offsets, due to the directionality of the imine bonds that lead to an asymmetrical bonding environment between the two adjacent neighboring porphyrin cores.

Hence, by manipulating the covalent bonds within the COF network we are able to create 2D materials whose electronic and chemical properties can be controlled with high degree of precision. This will be useful for creating future 2D materials with exotic properties such as tunable bandgaps, catalytic response, optical absorption and photovoltaic behavior.

Chapter 6-Coupled Plasmon and Phonon Polaritons in a Hybrid Structure

This chapter describes the study of novel coupling behavior arising from interaction between two distinctive polaritons in different dimensionality. More specifically, we observe the coupling between 1D plasmon polaritons in silver nanowires with 2D phonon polaritons of the silicon carbide (SiC) substrate supporting them. The researchers who contributed to these studies are Trinity Joshi, Dr. Ji-Hun Kang, Dr. Lili Jiang, Sheng Wang, Theron Tarigo, Tairu Lyu, Salman Kahn, Dr. Zhiwen Shi, Dr. Yuen-Ron Shen, Dr. Michael F. Crommie, and Dr. Feng Wang. The work described below was originally published in ref. [58].

6.1 Introduction

Recently there has been increasing interest in plasmon excitations in lower dimensional materials such as silver nanowires [138, 139], graphene [140–142], and carbon nanotubes [143], and such plasmon polaritons are often strongest in the infrared spectral range. At the same time, phonon polaritons are also present at infrared frequencies in polar crystals [144–146], and they exhibit lower intrinsic loss compared to the metal-based plasmonics. Simultaneous excitation of both infrared plasmon polaritons and phonon polaritons in low-dimensional hybrid structures offers exciting opportunities to further control infrared light-matter interactions at the nanoscale.

Recently there have been a few studies on the coupling between 2D graphene plasmons with different optical phonon modes. For example, the coupling between 2D graphene plasmons and substrate optical phonons of the SiO₂ and SiC substrates can lead to strong modifications of the graphene dispersion relation [147–150]; the 2D plasmon-phonon coupling can also enhance the phonon absorption of thin PMMA layers due to the graphene plasmons [151] and the interaction between 2D plasmon in graphene and 2D phonon polariton in monolayer hexagonal boron nitride (h-BN) lead to hybrid polariton modes [152]. In this chapter, we investigate for the first time the coupling between 1D plasmon polariton in silver nanowires with 2D phonon polariton of the SiC substrate. Due to the different dimensionality of the subsystem, the plasmon-phonon coupling exhibit unusual behavior that is distinctly different from couplings between 2D plasmon and 2D phonon polaritons. We use the scattering type near-field infrared nanoscopy with tunable laser excitation to directly map out the polariton excitation in the hybrid system in the spectral range from 9.8 to 10.6 μm . We show that the plasmon wavelength of the silver nanowire changes drastically when the photon energy approaches the SiC phonon polariton energies. In particular, we observe well-defined 1D plasmon polariton excitation with the plasmon wavelength exceeding the free-space photon wavelengths in a finite spectral range. This behavior is in striking contrast of conventional surface plasmons, where the plasmon wavelengths are always shorter than the free space photon wavelength [143, 147, 153, 154]. In addition, we carry out numerical

Chapter 6-Coupled Plasmon and Phonon Polaritons in a Hybrid Structure

simulation of the polaritons in such hybrid 1D-2D system using the finite-difference time-domain (FDTD) method, which shows good agreement with our experimental observations.

6.2 Experimental set-up

Silver nanowires with diameters around 80 nm and lengths up to 50 μm dissolved in ethanol solutions were obtained from Blue Nano Inc. The diluted solution of silver nanowires was spin-coated onto the SiC substrate to form isolated individual silver nanowires on SiC. Infrared near-field nanoscopy [59–61, 155] was used to image the polariton excitations in the hybrid silver nanowires/SiC system. We employ a continuously tunable quantum cascade laser [daylight solutions MIRcat 1200 system] to provide excitation photons ranging from 9.8 μm to 10.57 μm . The infrared radiation was focused onto the apex of a gold-coated atomic force microscope (AFM) tip that provides strong momentum-kick and consequently enables excitation of SPs on the silver nanowire or PhPs on the SiC substrate. Figure 6.1(a) shows the schematic of the set-up for launching of the plasmon waves in the silver nanowire. When the infrared light of wavelength 9.8 μm to 10.57 μm is focused onto the apex of the metallic AFM tip in steps plasmons are optically excited in the nanowire. These excited plasmon wave travel along the length of the wire and are reflected back from the nanowire end. The back reflected plasmon wave interfered with the plasmon wave launched under the tip. Thus, we obtain a standing wave pattern. This standing wave pattern revealed itself as the peaks of varying intensity upon measuring the scattered infrared radiation by HgCdTe detector in the far field with the constructive interference appearing as high intensity peaks [138, 140–143, 145]. Figure 6.1(b) represents a three-dimensional infrared near-field nanoscopy image of an Ag nanowire on SiC at 10.2 μm excitation. We can confidently assign the prominent periodic oscillations observed in the near-field image to plasmon oscillations as such oscillation is absent in the corresponding topographical image shown in the inset. Here, we are measuring the standing wave pattern between the surface plasmons being launched under the tip and the plasmons being reflected from the end of the silver nanowire.

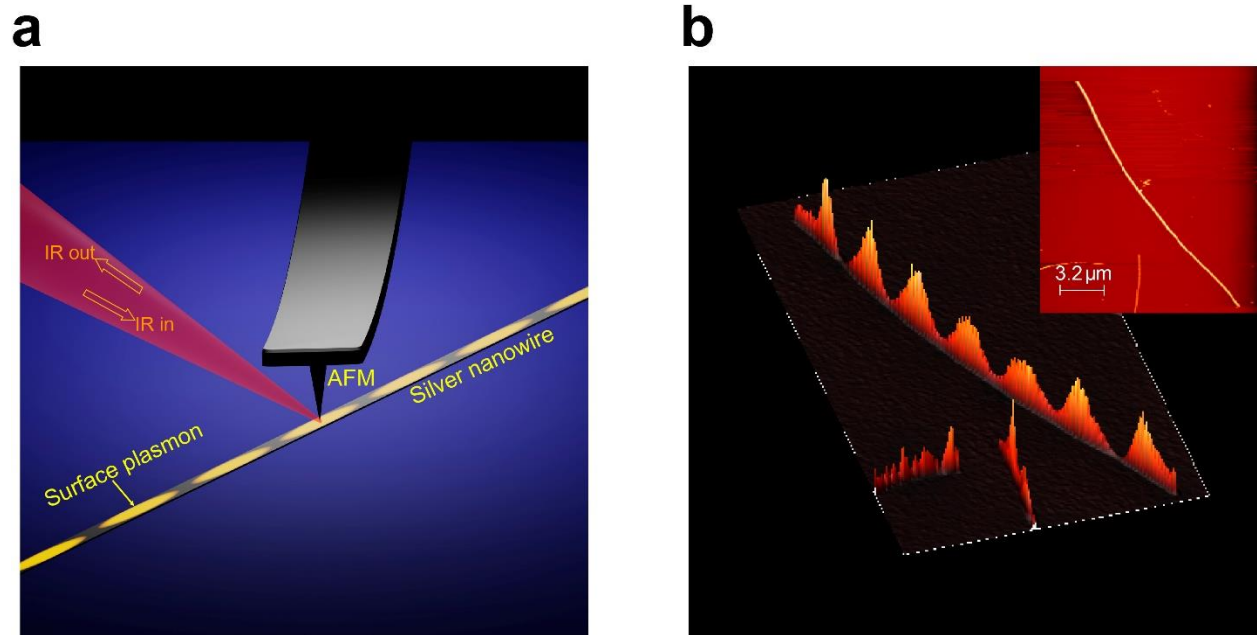


Figure 6.1 Experimental set-up (a) Schematic of the s-SNOM set-up. Infrared light ranging from 9.8 μm to 10.6 μm were focused onto the apex of a gold-coated atomic force microscope (AFM) tip in steps thus optically exciting the plasmons in the nanowire. These excited plasmon wave travel along the length of the wire and are reflected back at the nanowire end. The back reflected plasmon wave interfered with the plasmon wave launched under the tip giving a standing wave pattern. (b) 3D image of plasmons in Ag nanowire on SiC at 10.2 μm excitation. Each peak represents the antinode of the standing wave. Inset represents the corresponding topographical image of the Ag nanowire.

6.3 Experimental Observation

We systematically investigated plasmons in an Ag nanowire at increasing excitation wavelength closer to the phonon resonance of our substrate. Figure 6.2 (a)-(h) presents the near-field infrared nanoscopy images of one-dimensional SPs in a silver nanowire with 9.8 μm to 10.57 μm photon excitation. The inset text on the upper right corner represents the excitation wavelength. Periodic oscillation of the tip-induced infrared scattering from the one-dimensional plasmon is evident in the nanowires at 9.8 μm to 10.57 μm photon excitation. As it is apparent from these images the oscillation period becomes longer with increasing excitation wavelength. However, the excitation wavelength and the oscillation period do not have the same ratio and are inconsistent with a linear scaling. The oscillation period tends to increase more rapidly upon approaching the phonon resonance of the SiC substrate, as can be seen clearly in Figure 6.2 (a)-(f). Figure 6.2(h) displays the near-field infrared scattering image of the same nanowire at 10.6 μm excitation. At

Chapter 6-Coupled Plasmon and Phonon Polaritons in a Hybrid Structure

10.6 μm , the SPs in the nanowire becomes very weak instead the PhPs in the SiC is launched and are reflected from the silver nanowire [145].

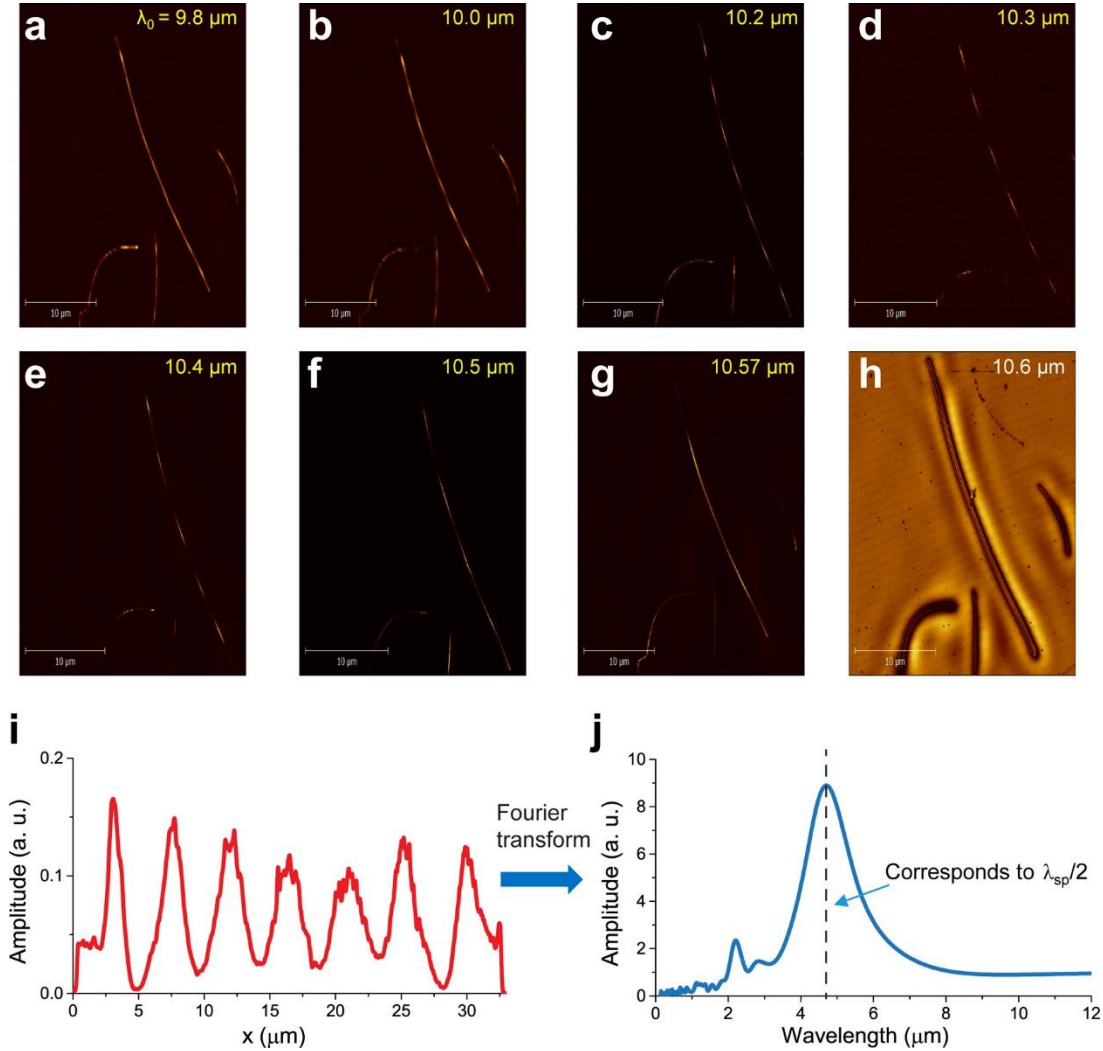


Figure 6.2 Experimental observation (a-h) Near-field infrared nanoscopy images of Ag nanowire/SiC at excitation wavelength from 9.8 μm to 10.6 μm . The number of oscillations along the length of the wire decreases thus increasing the SP wavelength as we approach to excitation wavelengths closer to the phonon resonance of the SiC. At 10.57 μm we only observe two oscillations or half wavelength. Furthermore, at 10.6 μm the plasmon in the nanowire becomes very weak. Also, the phonon polariton in the SiC is launched and is reflected from the silver nanowire. Therefore, we can observe a standing wave pattern of the phonon polariton next to the

Chapter 6-Coupled Plasmon and Phonon Polaritons in a Hybrid Structure

length of the wire. (i) Oscillation of near-field infrared scattering intensity from one-dimensional plasmons in the silver nanowire at 10.2 μm excitation wavelength. Shown in (i) and (j) is the method of experimental determination of plasmon wavelength. (i) A line-cut profile of plasmon at 10.2 μm excitation. (j) Fourier-transformed result of (i)

Figure 6.2(i) shows the oscillation of near-field infrared scattering intensity from one-dimensional plasmons in a silver nanowire at exemplary 10.2 μm excitation. Owing to strong reflections of SP at two ends of nanowires, well-defined cavity resonance of SP can be supported in nanowires. The scattering peaks (dips) in the near-field infrared nanoscopy images arises due to the constructive (destructive) interference between the surface plasmons launched under the tip and one that has been reflected from the nanowire end. Considering a phase change φ acquired upon reflection, the cavity resonance can be simply written as $Lq_{\text{sp}} + \varphi = m\pi$, where L is the length of the cavity, $q_{\text{p}} \equiv 2\pi/\lambda_{\text{sp}}$ and λ_{sp} respectively are the momentum and wavelength of SP, and m is a positive integer. Hence, the plasmon wavelength is given by twice the oscillation period observed in the near-field infrared nanoscopy images. In order to accurately determine the SP wavelength at each excitation wavelength, we performed Fourier-transform on the spatial plasmon profile presented in Figure 6.2(i) of the silver nanowire, yielding spectral plasmon profile as shown in Figure 6.2(j).

6.4 Theoretical Calculations and Comparison to Experimental Results

Figure 6.3 (a) and (b) illustrate the theoretically and experimentally obtained dependence of SP wavelength on the excitation wavelength. In both theoretical (blue solid lines) and experimental (red squares) results, the SP wavelength in SP-PhP coupled system, $\lambda_{\text{sp,c}}$, increases as the excitation wavelength λ_0 gets longer. There might be a discrepancy between the experimental and theoretical values of permittivities of SiC. Hence, a shift of 0.1 μm was introduced in the theoretical results (blue dotted-line) to compensate for the inconsistency between FDTD and experimental results. We can clearly see that, as λ_0 gets closer to the phonon resonance wavelength shown in Figure 6.3(c), $\lambda_{\text{sp,c}}$ rapidly increases compared to SP wavelength in an uncoupled (free-standing) case, $\lambda_{\text{sp,u}}$ (black solid line), which increases very slightly. Particularly, in both experimental and theoretical results, the increasing behavior of $\lambda_{\text{sp,c}}$ even gets faster when λ_0 is about 10.3-10.4 μm where the real-part of the dielectric function $\text{Re}(\epsilon)$ is very close to 0 as shown in Figure 6.3(d), and then, $\lambda_{\text{sp,c}}$ exceeds λ_0 . We note that this observation of the SP wavelength longer than free-space photon wavelength is very unique. In two-dimensional SP, supported by thin metal film on a substrate, one can easily find from the explicit dispersion relation [156] that the wavelength of SP is always smaller than free-space photon wavelength, regardless of dielectric function of the substrate. On the contrary, from our measurement and FDTD calculations, the 1D plasmon exceeds the free-space photon wavelength upon approaching the phonon resonance of the substrate. This surprising result is a unique property of 1D plasmon

Chapter 6-Coupled Plasmon and Phonon Polaritons in a Hybrid Structure

coupled to phonon polariton of SiC, and presumably enabled by an inefficient coupling between the 1D plasmon mode and the free space radiation mode. We also note that, based on the trends of SP wavelength increase, we can divide the spectral range into three sub-ranges specified by vertical dashed lines in Figure 6.3(b): ranges in which $\lambda_{sp,c} < \lambda_{sp,u}$, $\lambda_{sp,u} < \lambda_{sp,c} < \lambda_0$, and $\lambda_0 < \lambda_{sp,c}$ respectively. On comparing with the spectral behavior of dielectric function of SiC as shown in Figure 6.3(b), the excitation wavelength at which $\lambda_{sp,c} = \lambda_{sp,u}$ is shown to be close to $\text{Re}(\epsilon) = 1$, and that in the range $\text{Re}(\epsilon) < 0$, $\lambda_{sp,c}$ completely exceeds λ_0 and increases more rapidly with increase of λ_0 . We also can see that the excitation wavelength at which $\lambda_{sp,c} = \lambda_0$ is located in between $0 < \text{Re}(\epsilon) < 1$. Therefore, we can attribute the origin of the unique behavior of 1D plasmon exhibiting wavelength longer than the excitation photon wavelength to the coupling of the SPs and the PhPs.

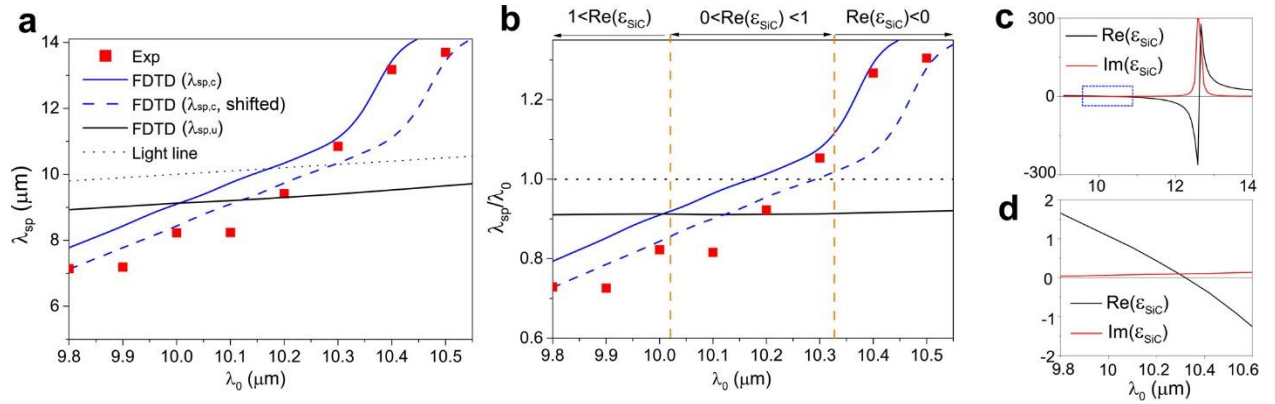


Figure 6.3 Experimentally measured and numerically calculated λ_{sp} . (a) λ_0 -dependent plasmon wavelengths on silver nanowire with and without SiC substrate. (b) Ratio of plasmon and photon wavelengths. Two vertical dotted lines denote the photon wavelengths where the real parts of dielectric constant of SiC are 1 and 0. In (a) and (b), dotted blue curves are 0.1 μm-shifted plots of FDTD results drawn in blue solid lines. (c) Dielectric constant of SiC [157]. (d) Zoom in of the blue rectangle on Figure 6.3(c).

Usually the SP momentum (wavelength) larger (shorter) than that of the photon is a necessary condition for SP to be bounded to the boundary of two media of opposite permittivities. Violating this condition indicates that the SP mode can be coupled out to the free-space plane-waves, i.e. it corresponds to a leaky mode. In the coupled 1D-2D polaritons of silver nanowire and SiC, such a leaky mode with SP wavelength longer than the free space photon wavelength exhibit well defined oscillations. This arises from the fact that unlike 2D SP, there is a large mismatch between the field distributions of 1D SP relative to the free space propagating mode. The strongly confined 1D SP field distribution calculated by FDTD simulation is shown in Figure 6.4.

Chapter 6-Coupled Plasmon and Phonon Polaritons in a Hybrid Structure

A qualitative understanding of our observed phenomena can be captured by the effective medium approximation. For the lowest order SP mode supported by nanowire surrounded by homogeneous medium, including for a free-standing one, the electric field component normal to the surface of nanowire can be written as [158]

$$E_r(r, z) = AK_1\left(\sqrt{q_{sp}^2 - \varepsilon_s k_0^2} r\right) e^{iq_{sp}z},$$

where r is the direction normal to the surface of the wire, A is a constant, K is the modified Bessel function of the second kind, ε_s is the relative permittivity of surrounding medium, and z is the SP propagation direction. Note that the normal component of electric field, directly related to the surface charge distribution, has no azimuthal dependence. Now, let us consider the substrate. Because the field distribution shown in Figure 6.4(b-d) indicates that the surface charge distribution is not strongly disturbed by the substrate, we approximate the SiC substrate and free-space as an effective homogeneous surrounding with the averaged relative permittivity $\varepsilon_{avg} \equiv (\varepsilon_{SiC} + \varepsilon_{air})/2$ for the surrounding. Then we obtain the dispersion relation of SP in silver nanowire as [158]

$$\frac{\varepsilon_m}{\sqrt{q_{sp}^2 - \varepsilon_m k_0^2}} \frac{I_1\left(\sqrt{q_{sp}^2 - \varepsilon_m k_0^2} a\right)}{I_0\left(\sqrt{q_{sp}^2 - \varepsilon_m k_0^2} a\right)} + \frac{\varepsilon_{avg}}{\sqrt{q_{sp}^2 - \varepsilon_{avg} k_0^2}} \frac{K_1\left(\sqrt{q_{sp}^2 - \varepsilon_{avg} k_0^2} a\right)}{K_0\left(\sqrt{q_{sp}^2 - \varepsilon_{avg} k_0^2} a\right)} = 0, \quad (6.1)$$

where ε_m and a respectively are the relative permittivity and radius of nanowire, and I is the modified Bessel function of the first kind. Note that the averaging of two permittivities, ε_{SiC} and ε_{air} , is effectively related to the averaging of the polarization density in the proximity of the nanowire. As shown in Figure 6.4(a), λ_0 -dependent SP wavelength in averaged system, analytically calculated from Eq. (6.1), can describe the qualitative dispersion feature observed in our experimental. We note, however, the effective media approximation becomes less accurate at wavelengths longer than 10.1 μm , where the dielectric constant of SiC becomes strongly negative. We also note that a strong lossy behavior of SP at 10.4 μm , shown in Figure 6.4(d) and (e), is mainly due to the material loss of the SiC. Specifically, the complex refractive index n of SiC at 10.4 μm is about $0.087 + 0.63i$, whereas that at 10.1 μm is about $0.88 + 0.045i$. The figure-of-merit of the refractive index, $\text{Re}(n)/\text{Im}(n)$, is therefore quite low at 10.4 μm , indicating that the intrinsic material loss of SiC at 10.4 μm is significant.

Chapter 6-Coupled Plasmon and Phonon Polaritons in a Hybrid Structure

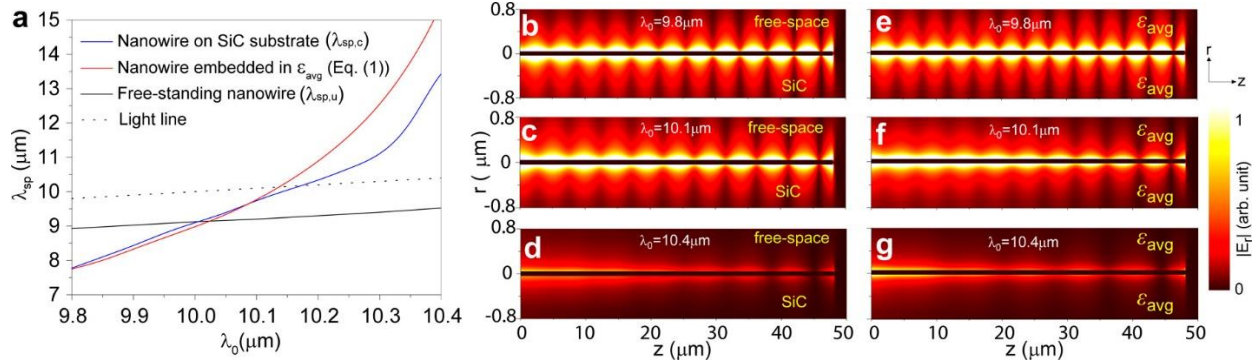


Figure 6.4 Theoretical calculations (a) SP wavelength comparison between nanowire/SiC coupled system and nanowire embedded in a homogeneous medium possessing averaged permittivity $\epsilon_{avg} \equiv (\epsilon_{SiC} + \epsilon_{air})/2$. For the embedded system, Eq. (1) is used to obtain SP wavelength. (b-g) FDTD-calculated z - r field-maps of r -component of electric field for (b-d) nanowire/SiC coupled system and (e-g) embedded system. Three exemplary photon wavelengths, 9.8, 10.1, and 10.4 microns, are selected. The z - r plane crosses the central axis of the silver nanowire and orthogonal to the SiC surface.

6.5 Materials and Methods. FDTD Numerical Calculations.

We used a homemade FDTD program for the numerical simulations. To implement deep subwavelength diameter of the silver nanowires, a nonuniform grid technique with a minimum grid size of 2 nm was adapted. The dispersive lossy natures of the silver nanowire and the SiC substrate were implemented by using an auxiliary differential equation method.

6.6 Conclusion and Outlook

In summary, we have experimentally and theoretically studied the localization behavior of SPs in SP-PhP coupled system. Our infrared scattering-type scanning near-field optical microscopy revealed that the localization of SPs in silver nanowire on the SiC substrate can be strongly modified by PhPs in the substrate, allowing SPs to possess unusual wavelength greater than the excitation photon wavelength in the proximity of phonon resonance wavelength. Also, our study on the coupling between SPs and PhPs in the 1D-2D heterostructures is specifically focused on the frequency regime where the dielectric constant of the SiC substrate is in the proximity of zero. Therefore, one possible implication of our study is related to so-called “epsilon-near-zero” (ENZ) polaritonics. In particular, our work demonstrates how strong changes in 1D SP characteristic can emerge from an ENZ material, especially how 1D SP behaves in the proximity of the interface of an ENZ material and the free-space. Since 1D-2D heterostructures that support

Chapter 6-Coupled Plasmon and Phonon Polaritons in a Hybrid Structure

two distinctive polaritons allow further control over the optical responses, our work is important for both understanding of physics of SP–PhP coupling and development of relevant applications.

Bibliography

Bibliography

- [1] Novak S, Parker C, Becher D, et al. Transistor aging and reliability in 14nm tri-gate technology. In: *2015 IEEE International Reliability Physics Symposium*. 2015, pp. 2F.2.1-2F.2.5.
- [2] Jan CH, Al-Amoody F, Chang HY, et al. A 14 nm SoC platform technology featuring 2nd generation Tri-Gate transistors, 70 nm gate pitch, 52 nm metal pitch, and 0.0499 μm^2 SRAM cells, optimized for low power, high performance and high density SoC products. In: *IEEE Symposium on VLSI Circuits, Digest of Technical Papers*. 2015. Epub ahead of print 2015. DOI: 10.1109/VLSIC.2015.7231380.
- [3] Cai J, Jaafar PRR, Bieri M, et al. Atomically precise bottom-up fabrication of graphene nanoribbons. *Nature*. Epub ahead of print 2010. DOI: 10.1038/nature09211.
- [4] Côté AP, Benin AI, Ockwig NW, et al. Porous, Crystalline, Covalent Organic Frameworks. *Science* (80-) 2005; 310: 1166 LP – 1170.
- [5] Ho K-I, Boutchich M, Su C-Y, et al. A Self-Aligned High-Mobility Graphene Transistor: Decoupling the Channel with Fluorographene to Reduce Scattering. *Adv Mater* 2015; 27: 6519–6525.
- [6] Lee C, Wei X, Kysar JW, et al. Measurement of the elastic properties and intrinsic strength of monolayer graphene. *Science* (80-). Epub ahead of print 2008. DOI: 10.1126/science.1157996.
- [7] Balandin AA, Ghosh S, Bao W, et al. Superior thermal conductivity of single-layer graphene. *Nano Lett*. Epub ahead of print 2008. DOI: 10.1021/nl0731872.
- [8] Morozov S V., Novoselov KS, Katsnelson MI, et al. Giant intrinsic carrier mobilities in graphene and its bilayer. *Phys Rev Lett*. Epub ahead of print 2008. DOI: 10.1103/PhysRevLett.100.016602.
- [9] Kim KS, Zhao Y, Jang H, et al. Large-scale pattern growth of graphene films for stretchable transparent electrodes. *Nature*. Epub ahead of print 2009. DOI: 10.1038/nature07719.
- [10] Schwierz F. Graphene transistors. *Nat Nanotechnol* 2010; 5: 487.
- [11] Yang L, Park C-H, Son Y-W, et al. Quasiparticle Energies and Band Gaps in Graphene Nanoribbons. *Phys Rev Lett* 2007; 99: 186801.

Bibliography

- [12] Son Y-W, Cohen ML, Louie SG. Energy Gaps in Graphene Nanoribbons. *Phys Rev Lett* 2006; 97: 216803.
- [13] Nakada K, Fujita M, Dresselhaus G, et al. Edge state in graphene ribbons: Nanometer size effect and edge shape dependence. *Phys Rev B* 1996; 54: 17954–17961.
- [14] Fujita M, Wakabayashi K, Nakada K, et al. Peculiar Localized State at Zigzag Graphite Edge. *J Phys Soc Japan* 1996; 65: 1920–1923.
- [15] Chen C. *On-Surface Synthesis and Local Electronic Structure Characterization of Low-Dimensional Nano-Materials*. University of California, Berkeley, 2018.
- [16] Chen Y-C. *Exploring Graphene Nanoribbons Using Scanning Probe Microscopy and Spectroscopy*. University of California, Berkeley, 2014.
- [17] Hybertsen MS, Louie SG. Electron correlation in semiconductors and insulators: Band gaps and quasiparticle energies. *Phys Rev B* 1986; 34: 5390–5413.
- [18] Chen Y-C, Cao T, Chen C, et al. Molecular bandgap engineering of bottom-up synthesized graphene nanoribbon heterojunctions. *Nat Nanotechnol* 2015; 10: 156.
- [19] Tao C, Jiao L, Yazyev O V, et al. Spatially resolving edge states of chiral graphene nanoribbons. *Nat Phys* 2011; 7: 616.
- [20] Li YY, Chen MX, Weinert M, et al. Direct experimental determination of onset of electron–electron interactions in gap opening of zigzag graphene nanoribbons. *Nat Commun* 2014; 5: 4311.
- [21] Xi M, Bent BE. Mechanisms of the Ullmann coupling reaction in adsorbed monolayers. *J Am Chem Soc* 1993; 115: 7426–7433.
- [22] Xi M, Bent BE. Iodobenzene on Cu(111): formation and coupling of adsorbed phenyl groups. *Surf Sci* 1992; 278: 19–32.
- [23] Sambigioglio C, Marsden SP, Blacker AJ, et al. Copper catalysed Ullmann type chemistry: from mechanistic aspects to modern development. *Chem Soc Rev* 2014; 43: 3525–3550.
- [24] Dong L, Liu PN, Lin N. Surface-Activated Coupling Reactions Confined on a Surface. *Acc Chem Res* 2015; 48: 2765–2774.
- [25] Ruffieux P, Wang S, Yang B, et al. On-surface synthesis of graphene nanoribbons with zigzag edge topology. *Nature* 2016; 531: 489.

Bibliography

- [26] Chen Y-C, de Oteyza DG, Pedramrazi Z, et al. Tuning the Band Gap of Graphene Nanoribbons Synthesized from Molecular Precursors. *ACS Nano* 2013; 7: 6123–6128.
- [27] Cloke RR, Marangoni T, Nguyen GD, et al. Site-Specific Substitutional Boron Doping of Semiconducting Armchair Graphene Nanoribbons. *J Am Chem Soc*. Epub ahead of print 2015. DOI: 10.1021/jacs.5b02523.
- [28] Nguyen GD, Toma FM, Cao T, et al. Bottom-Up Synthesis of $N = 13$ Sulfur-Doped Graphene Nanoribbons. *J Phys Chem C* 2016; 120: 2684–2687.
- [29] Hunt JR, Doonan CJ, LeVangie JD, et al. Reticular Synthesis of Covalent Organic Borosilicate Frameworks. *J Am Chem Soc* 2008; 130: 11872–11873.
- [30] El-Kaderi HM, Hunt JR, Mendoza-Cortés JL, et al. Designed Synthesis of 3D Covalent Organic Frameworks. *Science (80-)* 2007; 316: 268 LP – 272.
- [31] Castro Neto AH, Guinea F, Peres NMR, et al. The electronic properties of graphene. *Rev Mod Phys*. Epub ahead of print 2009. DOI: 10.1103/RevModPhys.81.109.
- [32] Geim AK. Graphene: Status and Prospects. *Science (80-)* 2009; 324: 1530 LP – 1534.
- [33] Xu X, Yao W, Xiao D, et al. Spin and pseudospins in layered transition metal dichalcogenides. *Nat Phys* 2014; 10: 343.
- [34] Wang QH, Kalantar-Zadeh K, Kis A, et al. Electronics and optoelectronics of two-dimensional transition metal dichalcogenides. *Nature Nanotechnology*. Epub ahead of print 2012. DOI: 10.1038/nnano.2012.193.
- [35] Mak KF, Shan J. Photonics and optoelectronics of 2D semiconductor transition metal dichalcogenides. *Nature Photonics*. Epub ahead of print 2016. DOI: 10.1038/nphoton.2015.282.
- [36] Manzeli S, Ovchinnikov D, Pasquier D, et al. 2D transition metal dichalcogenides. *Nature Reviews Materials*. Epub ahead of print 2017. DOI: 10.1038/natrevmats.2017.33.
- [37] Diercks CS, Yaghi OM. The atom, the molecule, and the covalent organic framework. *Science*. Epub ahead of print 2017. DOI: 10.1126/science.aal1585.
- [38] Liu Z, Liu F, Wu YS. Exotic electronic states in the world of flat bands: From theory to material. *Chinese Physics B*. Epub ahead of print 2014. DOI: 10.1088/1674-1056/23/7/077308.
- [39] Slot MR, Gardenier TS, Jacobse PH, et al. Experimental realization and characterization

Bibliography

- of an electronic Lieb lattice. *Nat Phys*. Epub ahead of print 2017. DOI: 10.1038/nphys4105.
- [40] Uribe-Romo FJ, Doonan CJ, Furukawa H, et al. Crystalline covalent organic frameworks with hydrazone linkages. *J Am Chem Soc*. Epub ahead of print 2011. DOI: 10.1021/ja204728y.
- [41] Uribe-Romo FJ, Hunt JR, Furukawa H, et al. A crystalline imine-linked 3-D porous covalent organic framework. *J Am Chem Soc*. Epub ahead of print 2009. DOI: 10.1021/ja8096256.
- [42] Dalapati S, Jin S, Gao J, et al. An azine-linked covalent organic framework. *J Am Chem Soc*. Epub ahead of print 2013. DOI: 10.1021/ja4103293.
- [43] Nagai A, Guo Z, Feng X, et al. Pore surface engineering in covalent organic frameworks. *Nat Commun*. Epub ahead of print 2011. DOI: 10.1038/ncomms1542.
- [44] Spitler EL, Dichtel WR. Lewis acid-catalysed formation of two-dimensional phthalocyanine covalent organic frameworks. *Nat Chem*. Epub ahead of print 2010. DOI: 10.1038/nchem.695.
- [45] Bisbey RP, Dichtel WR. Covalent Organic Frameworks as a Platform for Multidimensional Polymerization. *ACS Cent Sci*. Epub ahead of print 2017. DOI: 10.1021/acscentsci.7b00127.
- [46] Colson JW, Woll AR, Mukherjee A, et al. Oriented 2D covalent organic framework thin films on single-layer graphene. *Science (80-)*. Epub ahead of print 2011. DOI: 10.1126/science.1202747.
- [47] Tanoue R, Higuchi R, Enoki N, et al. Thermodynamically controlled self-assembly of covalent nanoarchitectures in aqueous solution. *ACS Nano*. Epub ahead of print 2011. DOI: 10.1021/nn200393q.
- [48] Zwaneveld NAA, Pawlak R, Abel M, et al. Organized formation of 2D extended covalent organic frameworks at surfaces. *J Am Chem Soc*. Epub ahead of print 2008. DOI: 10.1021/ja800906f.
- [49] Gutzler R, Walch H, Eder G, et al. Surface mediated synthesis of 2D covalent organic frameworks: 1,3,5-tris(4-bromophenyl)benzene on graphite(001), Cu(111), and Ag(110). *Chem Commun*. Epub ahead of print 2009. DOI: 10.1039/b906836h.
- [50] Sánchez-Sánchez C, Brüller S, Sachdev H, et al. On-Surface Synthesis of BN-Substituted Heteroaromatic Networks. *ACS Nano*. Epub ahead of print 2015. DOI:

Bibliography

- 10.1021/acsnano.5b03895.
- [51] Bieri M, Nguyen MT, Gröning O, et al. Two-dimensional polymer formation on surfaces: Insight into the roles of precursor mobility and reactivity. *J Am Chem Soc.* Epub ahead of print 2010. DOI: 10.1021/ja107947z.
- [52] Liu XH, Guan CZ, Ding SY, et al. On-surface synthesis of single-layered two-dimensional covalent organic frameworks via solid-vapor interface reactions. *J Am Chem Soc.* Epub ahead of print 2013. DOI: 10.1021/ja403464h.
- [53] Morchutt C, Björk J, Straßer C, et al. Interplay of Chemical and Electronic Structure on the Single-Molecule Level in 2D Polymerization. *ACS Nano* 2016; 10: 11511–11518.
- [54] Steiner C, Gebhardt J, Ammon M, et al. Hierarchical on-surface synthesis and electronic structure of carbonyl-functionalized one- and two-dimensional covalent nanoarchitectures. *Nat Commun* 2017; 8: 14765.
- [55] Schiff H. Mittheilungen aus dem Universitätslaboratorium in Pisa: Eine neue Reihe organischer Basen. *Justus Liebigs Ann Chem.* Epub ahead of print 1864. DOI: 10.1002/jlac.18641310113.
- [56] Chen C, Joshi T, Li H, et al. Local Electronic Structure of a Single-Layer Porphyrin-Containing Covalent Organic Framework. *ACS Nano* 2018; 12: 385–391.
- [57] Joshi T, Chen C, Li H, et al. Local Electronic Structure of Molecular Heterojunctions in a Single-Layer 2D Covalent Organic Framework. *Adv Mater* 2019; 31: 1805941.
- [58] Joshi T, Kang J-H, Jiang L, et al. Coupled One-Dimensional Plasmons and Two-Dimensional Phonon Polaritons in Hybrid Silver Nanowire/Silicon Carbide Structures. *Nano Lett* 2017; 17: 3662–3667.
- [59] Keilmann F, Hillenbrand R. Near-field microscopy by elastic light scattering from a tip. *Phil Trans R Soc Lond A* 2004; 362: 787–805.
- [60] Novotny L, Hecht B. *Principles of Nano-Optics*. Cambridge Univ. Press, 2006.
- [61] Gerber JA, Berweger S, O’Callahan BT, et al. Phase-resolved surface plasmon interferometry of graphene. *Phys Rev Lett* 2014; 113: 055502.
- [62] Chen CJ. *Introduction to Scanning Tunneling Microscopy: Second Edition*. Oxford: Oxford University Press. Epub ahead of print 2007. DOI: 10.1093/acprof:oso/9780199211500.001.0001.

Bibliography

- [63] Bardeen J. Tunnelling from a Many-Particle Point of View. *Phys Rev Lett* 1961; 6: 57–59.
- [64] Bardeen J, Cooper LN, Schrieffer JR. Theory of Superconductivity. *Phys Rev* 1957; 108: 1175–1204.
- [65] Giaever I. Energy Gap in Superconductors Measured by Electron Tunneling. *Phys Rev Lett* 1960; 5: 147–148.
- [66] Giaever I, Megerle K. Study of Superconductors by Electron Tunneling. *Phys Rev* 1961; 122: 1101–1111.
- [67] Giaever I. Electron Tunneling Between Two Superconductors. *Phys Rev Lett* 1960; 5: 464–466.
- [68] Ashcroft NW, Mermin ND. *Solid state physics*. Philadelphia, Pa.: Saunders college, 1976.
- [69] Tersoff J, Hamann DR. Theory of the scanning tunneling microscope. *Phys Rev B* 1985; 31: 805–813.
- [70] Tersoff J, Hamann DR. Theory and Application for the Scanning Tunneling Microscope. *Phys Rev Lett* 1983; 50: 1998–2001.
- [71] Yamachika R. *Probing atomic-scale properties of organic and organometallic molecules by scanning tunneling spectroscopy*. University of California, Berkeley, 2009.
- [72] Comstock MJ. *Photomechanical Switching of Individual Molecules on a Surface*. University of California, Berkeley, 2008.
- [73] Niv B, Levy. *Investigations into nanometer scale surface opto-electro-mechanical coupling*. University of California, Berkeley, 2010.
- [74] Cho J. *No Title*. University of California, Berkeley, 2010.
- [75] I. V. Pechenezhskiy. *Photomechanical Response of Molecular Nanostructures*. University of California, Berkeley, 2013. Epub ahead of print 2013. DOI: 10.1017/CBO9781107415324.004.
- [76] Nguyen GD. *Engineering the electronic structure of atomically-precise graphene nanoribbonso Title*. University of California, Berkeley, 2016.
- [77] Binnig G, Quate CF, Gerber C. Atomic Force Microscope. *Phys Rev Lett* 1986; 56: 930–933.

Bibliography

- [78] Binnig G, Gerber C, Stoll E, et al. Atomic resolution with atomic force microscope. *Surf Sci* 1987; 189–190: 1–6.
- [79] Gerber J. Real-Time Detection for Scattering Scanning Near-Field Optical Microscopy. *Undergrad Honor Theses*, https://scholar.colorado.edu/honr_theses/357 (2013, accessed 13 March 2019).
- [80] Synge EH. XXXVIII. A suggested method for extending microscopic resolution into the ultra-microscopic region. *London, Edinburgh, Dublin Philos Mag J Sci* 1928; 6: 356–362.
- [81] Keilmann F, Hillenbrand R. *Near-field microscopy by elastic light scattering from a tip: One contribution of 13 to a Theme 'Nano-optics and near-field microscopy'*. 2004. Epub ahead of print 1 May 2004. DOI: 10.1098/rsta.2003.1347.
- [82] Inouye Y, Kawata S. Near-field scanning optical microscope with a metallic probe tip. *Opt Lett* 1994; 19: 159–161.
- [83] L. Olmon R. *Optical Vector Near-Field Imaging for the Design of Impedance Matched Optical Antennas and Devices*. 2012.
- [84] Calander N, Willander M. Theory of surface-plasmon resonance optical-field enhancement at prolate spheroids. *J Appl Phys* 2002; 92: 4878–4884.
- [85] Atkin JM, Berweger S, Jones AC, et al. Nano-optical imaging and spectroscopy of order, phases, and domains in complex solids. *Adv Phys* 2012; 61: 745–842.
- [86] Kim WY, Kim KS. Prediction of very large values of magnetoresistance in a graphene nanoribbon device. *Nat Nanotechnol* 2008; 3: 408.
- [87] Son Y-W, Cohen ML, Louie SG. Half-metallic graphene nanoribbons. *Nature* 2006; 444: 347.
- [88] Barone V, Hod O, Scuseria GE. Electronic Structure and Stability of Semiconducting Graphene Nanoribbons. *Nano Lett* 2006; 6: 2748–2754.
- [89] Zhang X, Yazyev O V, Feng J, et al. Experimentally Engineering the Edge Termination of Graphene Nanoribbons. *ACS Nano* 2013; 7: 198–202.
- [90] Zhang H, Lin H, Sun K, et al. On-surface synthesis of rylene-type graphene nanoribbons. *J Am Chem Soc*. Epub ahead of print 2015. DOI: 10.1021/ja511995r.
- [91] Cai J, Pignedoli CA, Talirz L, et al. Graphene nanoribbon heterojunctions. *Nat Nanotechnol* 2014; 9: 896.

Bibliography

- [92] Bronner C, Stremlau S, Gille M, et al. Aligning the band gap of graphene nanoribbons by monomer doping. *Angew Chemie - Int Ed*. Epub ahead of print 2013. DOI: 10.1002/anie.201209735.
- [93] Zhang Y, Zhang Y, Li G, et al. Direct visualization of atomically precise nitrogen-doped graphene nanoribbons. *Appl Phys Lett*. Epub ahead of print 2014. DOI: 10.1063/1.4884359.
- [94] Bieller S, Zhang F, Bolte M, et al. Bitopic Bis- and Tris(1-pyrazolyl)borate Ligands: Syntheses and Structural Characterization. *Organometallics* 2004; 23: 2107–2113.
- [95] Hoffend C, Schödel F, Bolte M, et al. Boron-Doped Tri(9,10-anthrylene)s: Synthesis, Structural Characterization, and Optoelectronic Properties. *Chem – A Eur J* 2012; 18: 15394–15405.
- [96] Dou C, Saito S, Matsuo K, et al. A Boron-Containing PAH as a Substructure of Boron-Doped Graphene. *Angew Chemie Int Ed* 2012; 51: 12206–12210.
- [97] Blankenburg S, Cai J, Ruffieux P, et al. Intraribbon Heterojunction Formation in Ultranarrow Graphene Nanoribbons. *ACS Nano* 2012; 6: 2020–2025.
- [98] Ruffieux P, Cai J, Plumb NC, et al. Electronic Structure of Atomically Precise Graphene Nanoribbons. *ACS Nano* 2012; 6: 6930–6935.
- [99] Batra A, Cvetko D, Kladnik G, et al. Probing the mechanism for graphene nanoribbon formation on gold surfaces through X-ray spectroscopy. *Chem Sci* 2014; 5: 4419–4423.
- [100] Bronner C, Björk J, Tegeder P. Tracking and Removing Br during the On-Surface Synthesis of a Graphene Nanoribbon. *J Phys Chem C* 2015; 119: 486–493.
- [101] Basagni A, Sedona F, Pignedoli CA, et al. Molecules–Oligomers–Nanowires–Graphene Nanoribbons: A Bottom-Up Stepwise On-Surface Covalent Synthesis Preserving Long-Range Order. *J Am Chem Soc* 2015; 137: 1802–1808.
- [102] Narita A, Verzhbitskiy IA, Frederickx W, et al. Bottom-Up Synthesis of Liquid-Phase-Processable Graphene Nanoribbons with Near-Infrared Absorption. *ACS Nano* 2014; 8: 11622–11630.
- [103] Talirz L, Söde H, Cai J, et al. Termini of Bottom-Up Fabricated Graphene Nanoribbons. *J Am Chem Soc* 2013; 135: 2060–2063.
- [104] Chen W, Madhavan V, Jamneala T, et al. Scanning Tunneling Microscopy Observation of an Electronic Superlattice at the Surface of Clean Gold. *Phys Rev Lett* 1998; 80: 1469–

Bibliography

- 1472.
- [105] Yang Z, Yao Z, Li G, et al. Sulfur-doped graphene as an efficient metal-free cathode catalyst for oxygen reduction. *ACS Nano*. Epub ahead of print 2012. DOI: 10.1021/nm203393d.
- [106] Madhavan V, Chen W, Jamneala T, et al. Local spectroscopy of a Kondo impurity: Co on Au(111). *Phys Rev B - Condens Matter Mater Phys*. Epub ahead of print 2001. DOI: 10.1103/PhysRevB.64.165412.
- [107] Giannozzi P, Baroni S, Bonini N, et al. QUANTUM ESPRESSO: a modular and open-source software project for quantum simulations of materials. *J Phys Condens Matter* 2009; 21: 395502.
- [108] Kuhn P, Antonietti M, Thomas A. Porous, covalent triazine-based frameworks prepared by ionothermal synthesis. *Angew Chemie - Int Ed*. Epub ahead of print 2008. DOI: 10.1002/anie.200705710.
- [109] Furukawa H, Yaghi OM. Storage of Hydrogen, Methane, and Carbon Dioxide in Highly Porous Covalent Organic Frameworks for Clean Energy Applications. *J Am Chem Soc* 2009; 131: 8875–8883.
- [110] Doonan CJ, Tranchemontagne DJ, Glover TG, et al. Exceptional ammonia uptake by a covalent organic framework. *Nat Chem*. Epub ahead of print 2010. DOI: 10.1038/nchem.548.
- [111] Ding S-Y, Gao J, Wang Q, et al. Construction of Covalent Organic Framework for Catalysis: Pd/COF-LZU1 in Suzuki–Miyaura Coupling Reaction. *J Am Chem Soc* 2011; 133: 19816–19822.
- [112] Lin S, Diercks CS, Zhang Y-B, et al. Covalent organic frameworks comprising cobalt porphyrins for catalytic CO₂ reduction in water. *Science (80-)* 2015; 349: 1208 LP – 1213.
- [113] Qianrong F, Shuang G, Jie Z, et al. 3D Microporous Base-Functionalized Covalent Organic Frameworks for Size-Selective Catalysis. *Angew Chemie Int Ed* 2014; 53: 2878–2882.
- [114] Shun W, Jia G, Jangbae K, et al. A Photoconductive Covalent Organic Framework: Self-Condensed Arene Cubes Composed of Eclipsed 2D Polypyrene Sheets for Photocurrent Generation. *Angew Chemie Int Ed* 2009; 48: 5439–5442.
- [115] Mirjam D, Matthias H, Florian A, et al. A Photoconductive Thienothiophene-Based

Bibliography

- Covalent Organic Framework Showing Charge Transfer Towards Included Fullerene. *Angew Chemie Int Ed* 2013; 52: 2920–2924.
- [116] Dai W, Shao F, Szczerbiński J, et al. Synthesis of a Two-Dimensional Covalent Organic Monolayer through Dynamic Imine Chemistry at the Air/Water Interface. *Angew Chemie Int Ed* 2016; 55: 213–217.
- [117] Sahabudeen H, Qi H, Glatz BA, et al. Wafer-sized multifunctional polyimine-based two-dimensional conjugated polymers with high mechanical stiffness. *Nat Commun*. Epub ahead of print 2016. DOI: 10.1038/ncomms13461.
- [118] Grill L, Dyer M, Lafferentz L, et al. Nano-architectures by covalent assembly of molecular building blocks. *Nat Nanotechnol*. Epub ahead of print 2007. DOI: 10.1038/nnano.2007.346.
- [119] Wan S, Gándara F, Asano A, et al. Covalent Organic Frameworks with High Charge Carrier Mobility. *Chem Mater* 2011; 23: 4094–4097.
- [120] Sun X, Fan L, Zhou X, et al. Surface confined synthesis of porphyrin containing two-dimensional polymers: The effect of rigidity and preferential adsorption of building blocks. *Chem Commun*. Epub ahead of print 2015. DOI: 10.1039/c5cc00659g.
- [121] Spitler EL, Colson JW, Uribe-Romo FJ, et al. Lattice expansion of highly oriented 2D phthalocyanine covalent organic framework films. *Angew Chemie - Int Ed*. Epub ahead of print 2012. DOI: 10.1002/anie.201107070.
- [122] Müllegger S, Schöffberger W, Rashidi M, et al. Spectroscopic STM studies of single gold(III) porphyrin molecules. *J Am Chem Soc*. Epub ahead of print 2009. DOI: 10.1021/ja908157j.
- [123] Liu X-H, Yue J-Y, Mo Y-P, et al. Surface Host–Guest Supramolecular Assemblies on Porphyrin-Based Covalent Organic Grids. *J Phys Chem C* 2016; 120: 15753–15757.
- [124] Yokoyama T, Yokoyama S, Kamikado T, et al. Nonplanar adsorption and orientational ordering of porphyrin molecules on Au(111). *J Chem Phys* 2001; 115: 3814–3818.
- [125] Zhang Q, Zheng X, Kuang G, et al. Single-Molecule Investigations of Conformation Adaptation of Porphyrins on Surfaces. *J Phys Chem Lett* 2017; 8: 1241–1247.
- [126] Auwärter W, Seufert K, Klappenberger F, et al. *Site-specific electronic and geometric interface structure of Co-tetraphenyl-porphyrin layers on Ag(111)*. 2010. Epub ahead of print 1 June 2010. DOI: 10.1103/PhysRevB.81.245403.

Bibliography

- [127] Diercks CS, Lin S, Kornienko N, et al. Reticular Electronic Tuning of Porphyrin Active Sites in Covalent Organic Frameworks for Electrocatalytic Carbon Dioxide Reduction. *J Am Chem Soc* 2018; 140: 1116–1122.
- [128] DeBlase CR, Hernández-Burgos K, Silberstein KE, et al. Rapid and Efficient Redox Processes within 2D Covalent Organic Framework Thin Films. *ACS Nano* 2015; 9: 3178–3183.
- [129] Wan S, Guo J, Kim J, et al. A Belt-Shaped, Blue Luminescent, and Semiconducting Covalent Organic Framework. *Angew Chemie Int Ed* 2008; 47: 8826–8830.
- [130] Lohse MS, Bein T. Covalent Organic Frameworks: Structures, Synthesis, and Applications. *Adv Funct Mater* 2018; 0: 1705553.
- [131] Ding S-Y, Wang W. Covalent organic frameworks (COFs): from design to applications. *Chem Soc Rev* 2013; 42: 548–568.
- [132] Xiao F, Long C, Yoshihito H, et al. An Ambipolar Conducting Covalent Organic Framework with Self-Sorted and Periodic Electron Donor-Acceptor Ordering. *Adv Mater* 2012; 24: 3026–3031.
- [133] Shangbin J, Xuesong D, Xiao F, et al. Charge Dynamics in A Donor–Acceptor Covalent Organic Framework with Periodically Ordered Bicontinuous Heterojunctions. *Angew Chemie Int Ed* 2013; 52: 2017–2021.
- [134] Jin S, Furukawa K, Addicoat M, et al. Large pore donor-acceptor covalent organic frameworks. *Chem Sci* 2013; 4: 4505–4511.
- [135] Hong S, Rohman MR, Jia J, et al. Porphyrin Boxes: Rationally Designed Porous Organic Cages. *Angew Chemie Int Ed* 2015; 54: 13241–13244.
- [136] Neaton JB, Hybertsen MS, Louie SG. Renormalization of Molecular Electronic Levels at Metal-Molecule Interfaces. *Phys Rev Lett* 2006; 97: 216405.
- [137] Hirshfeld FL. Bonded-atom fragments for describing molecular charge densities. *Theor Chim Acta* 1977; 44: 129–138.
- [138] Jones AC, Olmon RL, Skrabalak SE, et al. Mid-IR polasmonics: Near-field imaging of coherent plasmon modes of silver nanowires. *Nano Lett* 2009; 9: 2553–2558.
- [139] Novotny L. Effective wavelength scaling for optical antennas. *Phys Rev Lett* 2007; 98: 266802.

Bibliography

- [140] Chen J, Badioli M, Alonso-González P, et al. Optical nano-imaging of gate-tunable graphene plasmons. *Nature* 2012; 487: 77–81.
- [141] Fei Z, Rodin a. S, Andreev GO, et al. Gate-tuning of graphene plasmons revealed by infrared nano-imaging. *Nature* 2012; 487: 82–85.
- [142] Jiang L, Shi Z, Zeng B, et al. Soliton-dependent plasmon reflection at bilayer graphene domain walls. *Nat Mater* 2016; 15: 840–844.
- [143] Shi Z, Hong X, Bechtel HA, et al. Observation of a Luttinger-liquid plasmon in metallic single-walled carbon nanotubes. *Nat Photonics* 2015; 9: 515–519.
- [144] Shi Z, Bechtel HA, Berweger S, et al. Amplitude- and Phase-Resolved Nanospectral Imaging of Phonon Polaritons in Hexagonal Boron Nitride. *ACS Photonics* 2015; 2: 790–796.
- [145] Dai S, Fei Z, Ma Q, et al. Tunable Phonon Polaritons in Atomically Thin van der Waals Crystals of Boron Nitride. *Science (80-)* 2014; 343: 1125–1130.
- [146] Hillenbrand R. Towards phonon photonics: Scattering-type near-field optical microscopy reveals phonon-enhanced near-field interaction. *Ultramicroscopy* 2004; 100: 421–427.
- [147] Brar VW, Jang MS, Sherrott M, et al. Highly Confined Tunable Mid-Infrared Plasmonics in Graphene Nanoresonators. *Nano Lett* 2013; 13: 2541–2547.
- [148] Yan H, Low T, Zhu W, et al. Damping pathways of mid-infrared plasmons in graphene nanostructures. *Nat Photonics* 2013; 7: 394–399.
- [149] Liu Y, Willis RF. Plasmon-phonon strongly coupled mode in epitaxial graphene. *Phys Rev B* 2010; 81: 081406(R).
- [150] Koch RJ, Seyller T, Schaefer JA. Strong phonon-plasmon coupled modes in the graphene/silicon carbide heterosystem. *Phys Rev B* 2010; 82: 201413(R).
- [151] Li Y, Yan H, Farmer DB, et al. Graphene plasmon enhanced vibrational sensing of surface-adsorbed layers. *Nano Lett* 2014; 14: 1573–1577.
- [152] Brar VW, Jang MS, Sherrott M, et al. Hybrid surface-phonon-plasmon polariton modes in graphene/monolayer h-BN heterostructures. *Nano Lett* 2014; 14: 3876–3880.
- [153] Jablan M, Buljan H, Soljačić M. Plasmonics in graphene at infrared frequencies. *Phys Rev B* 2009; 80: 245435.

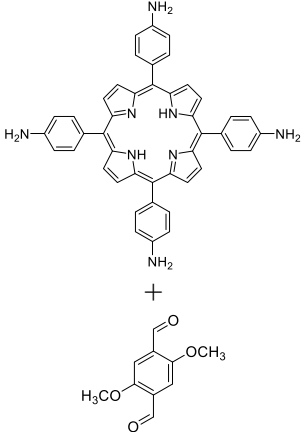
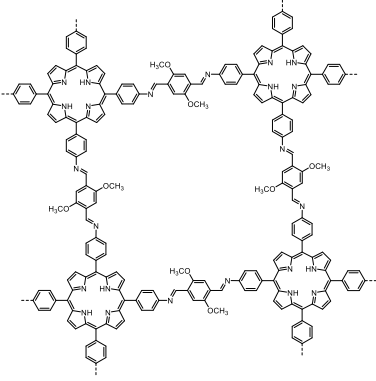
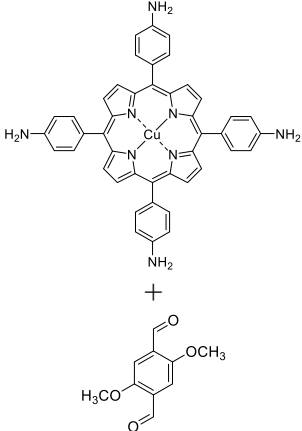
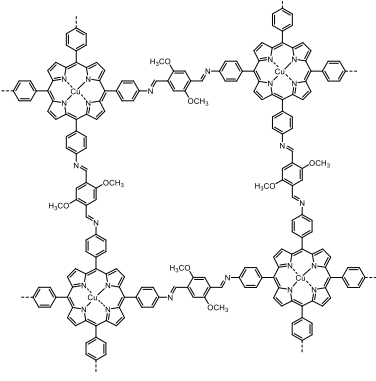
Bibliography

- [154] Maier SA. *Plasmonics: Fundamentals and Applications*. Boston, MA: Springer US, 2007. Epub ahead of print 2007. DOI: 10.1007/0-387-37825-1.
- [155] Bechtel HA, Muller EA, Olmon RL, et al. Ultrabroadband infrared nanospectroscopic imaging. *Proc Natl Acad Sci U S A* 2014; 111: 7191–7196.
- [156] Alù, Andrea, Engheta N. Optical Nanotransmission Lines : Synthesis of Planar Left-Handed Metamaterials in the Infrared and Visible Regimes. *J Opt Soc Am B* 2006; 23: 571–583.
- [157] Palik ED. *Handbook of Optical Constants of Solids*. New York: Academic Press, 1985. Epub ahead of print 1985. DOI: 10.1016/B978-0-08-054721-3.50036-8.
- [158] Pfeiffer CA, Economou EN, Ngai KL. Surface polaritons in a circularly cylindrical interface: Surface plasmons. *Phys Rev B* 1974; 10: 3038–3051.

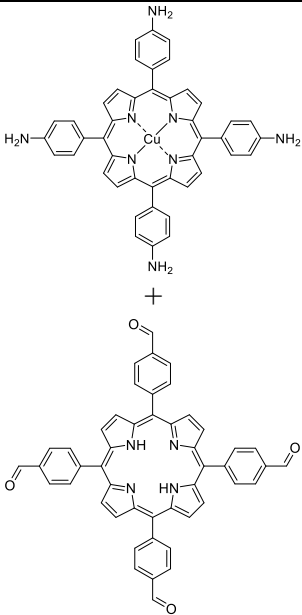
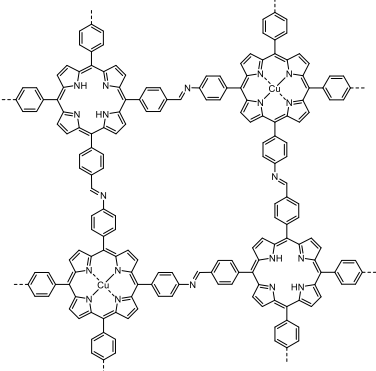
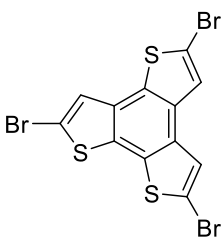
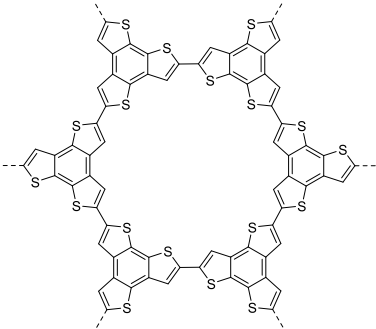
Appendix: List of All COFs studied

Appendix: List of All COFs studied

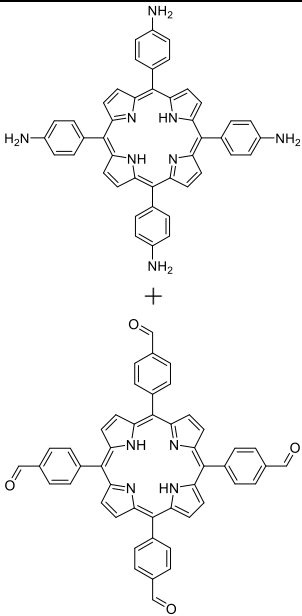
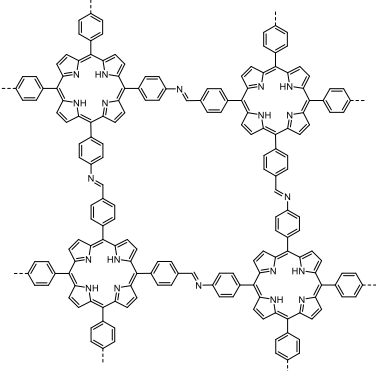
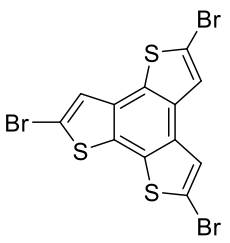
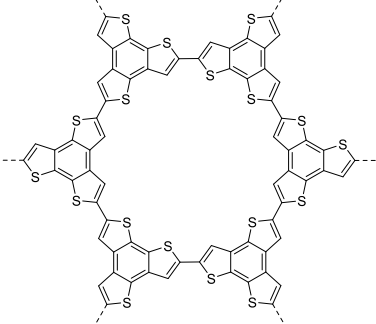
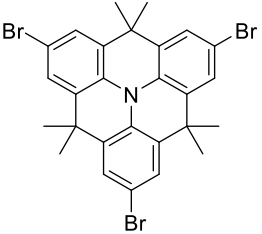
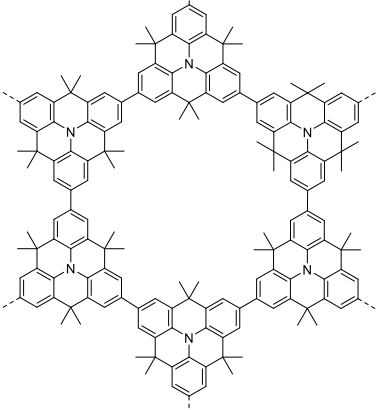
List of all the COF structures studied.

Molecule	Expected Product	Result Summary
		<p>On Au(111): square lattice COF with core-linker geometry.</p>
		<p>On Au(111): square lattice COF with core-linker geometry. Low coverage with small domain size.</p>

Appendix: List of All COFs studied

		<p>On Au(111): square lattice COF with checker board pattern.</p>
		<p>On Au(111): imperfect hexagonal lattice. On Cu(111): worm-like structure instead of ordered hexagons. On Ag(111): imperfect hexagonal lattice; also saw organometallic intermediate.</p>

Appendix: List of All COFs studied

		<p>On Au(111): square lattice COF with checker board pattern.</p>
		<p>On Au(111): got the hexagonal lattice with high coverage. On Ag(111): also saw hexagonal lattice, which might be MOF or COF.</p>
		<p>On Au(111): hexagonal COF with high coverage</p>

[15].